This is a postprint version of the following published document:

J. Muñoz-García, L. Vázquez, R. Gago, M. Castro, A. Redondo-Cubero, A. Moreno-Barrado, and R. Cuerno, "Self-organized nanopatterning of silicon surfaces by ion beam sputtering". In *Materials Science and Engineering: R: Reports* 86 (2014) pp.1-44.
Available in http://dx.doi.org/10.1016/j.mser.2014.09.001

© 2014 Elsevier

This work is licensed under a Creative Commons Attribution-NonCommercial-NoDerivatives 4.0 International License.

Self-organized nanopatterning of silicon surfaces by ion beam sputtering

Javier Muñoz-García[a,*], Luis Vázquez[b], Mario Castro[c], Raúl Gago[b], Andrés Redondo-Cubero[d], Ana Moreno-Barrado[c], Rodolfo Cuerno[a]

[a] Departamento de Matemáticas and GISC, Universidad Carlos III de Madrid, E-28911 Leganés, Spain
[b] Instituto de Ciencia de Materiales de Madrid (CSIC), Cantoblanco, E-28049 Madrid, Spain
[c] Grupo de Dinámica No-Lineal and Grupo Interdisciplinar de Sistemas Complejos (GISC), Escuela Técnica Superior de Ingeniería (ICAI), Universidad Pontificia Comillas, E-28015 Madrid, Spain
[d] Departamento de Física Aplicada, Universidad Autónoma de Madrid, Cantoblanco, E-28049 Madrid, Spain

Abstract: In recent years Ion Beam Sputtering (IBS) has revealed itself as a powerful technique to induce surface nanopatterns with a large number of potential applications. These structures are produced in rather short processing times and over relatively large areas, for a wide range of materials, such as metals, insulators, and semiconductors. In particular, silicon has become a paradigmatic system due to its technological relevance, as well as to its mono-elemental nature, wide availability, and production with extreme flatness. Thus, this review focuses on the IBS nanopatterning of silicon surfaces from the experimental and the theoretical points of view. First, the main experimental results and applications are described under the light of the recently established evidence on the key role played by simultaneous impurity incorporation during irradiation, which has opened a new scenario for an improved understanding of the phenomenon. Second, the progress and state-of-art of the theoretical descriptions of the IBS nanopatterning process for this type of targets are discussed. We summarize the historical approach to IBS through simulation techniques, with an emphasis on recent information from Molecular Dynamics methods, and provide a brief overview of the earlier and most recent continuum models for pure and compound systems.

Keywords: Ion beam technology, Nanopatterning, Silicon, Co-deposition.

Contents

1. Introduction 2
2. Historical overview 3
3. Experimental results 5
   3.1. Impurity-free patterning 5
      3.1.1. Low-energy (<10 keV) 5
      3.1.2. Medium-energy (10–200 keV) 10
   3.2. Patterning with simultaneous impurity incorporation 12
      3.2.1. Isotropic patterns: nanodot/nanohole patterns 12
      3.2.2. Anisotropic patterns: nanoripples 18
      3.2.3. Mechanisms for IBS patterning with metal co-deposition: systematic studies 23
4. Atomistic simulations 25
   4.1. Physical mechanisms involved in IBS 25

* Corresponding author.
E-mail address: javiermunozgarcia@gmail.com (J. Muñoz-García).

4.1.1. Mechanisms related to ion damage . . . 25
4.1.2. Mechanisms related to material relaxation . . . 26
4.2. Overview of numerical simulation methods for IBS . . . 27
4.3. Historical account of simulation results . . . 27
4.3.1. Early works: comparison between methods . . . 27
4.3.2. Amorphization and annealing after irradiation . . . 27
4.3.3. Atomistic simulations in the context of surface nanopatterning theories . . . 28
4.3.4. From MD to continuum models (crater function approach) . . . 29
5. Continuum models . . . 30
5.1. Early theories of IBS surface nanopatterning . . . 30
5.1.1. Geometric methods based on the sputtering yield . . . 30
5.1.2. The Bradley–Harper theory . . . 31
5.1.3. Refinements of Bradley-Harper theory . . . 32
5.2. Two-field models of IBS nanopatterning . . . 33
5.2.1. Two-field models for single-component systems . . . 33
5.2.2. Two-field composition models . . . 35
5.3. Stress-driven hydrodynamics of irradiated silicon targets . . . 37
6. Applications . . . 39
7. Concluding remarks . . . 41
Acknowledgements . . . 41
References . . . 41

1. Introduction

Already back in 1974, erosion of solid targets through ion-beam sputtering (IBS) was put forward by Taniguchi as the most promising technique at the time to nanostructure the surface of a wide range of materials [1]. Ironically, in spite of the visions contained in this seminal work that have been fulfilled, including the coinage of the word "Nanotechnology" itself, and in spite of the degree of empirical control reached in this technique—part of which will be reviewed in what follows—a fundamental understanding of the phenomenon has not been reached yet. Indeed, the morphologies produced form and self-organize spontaneously in response of the solid target to the energetic irradiation. As a result, ordered arrangements of nanoscale features emerge [2–4], like ripples and dots. Due to their characteristic length-scales in the range of a few, and up to hundreds of nanometers, they have a potential interest for technological applications due to e.g. their electronic, magnetic, and optical properties. Actually, the procedure can be conducted on different materials, amorphous or crystalline, in just a few minutes and over areas of several square centimeters. The diversity of materials processed and the similarities in the morphologies obtained indicate some kind of universality. Moreover, the technique can allow for a variation in the induced nanostructures by changing the sputtering parameters, such as ion energy, dose, substrate temperature, and ion incidence geometry. In this way, it can yield functional surfaces and confined structures.

Thus, in principle IBS does constitute a versatile, fast, and low-cost *bottom-up* technique for surface nanopatterning. In particular, it presents a number of advantages over e.g. *top-down* approaches like lithographic techniques or techniques based on scanning probe microscopy (SPM), such as a higher resolution and the capability to address large processed areas. With respect to other *bottom-up* procedures for nanostructuring like, e.g. semiconductor heterostructure growth, IBS does not require the use of ultra-high vacuum conditions. However, in order for it to finally become a nanopatterning technique which is up to the seminal expectations [1], precise control over the size, shape, crystallinity, and composition of the produced nanostructures is additionally required. This has however proved much more elusive, since it demands a thorough knowledge of the main physical mechanisms driving a phenomenon which, albeit seemingly simple, arises as the interplay of a number of multi-scale processes.

Silicon is a material which has played a particularly prominent role in the development of our understanding of IBS nanostructuring. This is naturally due to its well-known advantages with respect to integration [5] in microelectronic, electro-optical, electrochemical, electromechanical, sensing, and laser devices [6–8], and to the interesting properties of nanostructured silicon [9]. For instance, low-dimensional Si structures like nanowires are recently displaying a number of promising, novel structural, electronic, and transport properties [10]. Thus, silicon promises to be an excellent host for a new generation of devices, based on the quantum properties of charges and spins [11]. From a practical point of view, silicon is a mono-elemental material, which is widely available and can be manufactured with extreme flatness. This makes silicon a simpler system in principle, in which a clear assessment can be made of the relevant physical processes which are taking place during IBS in general. Furthermore, for the type of irradiation that we will be considering here, involving singly-charged ions with kinetic energies in the 0.5–100 keV range, silicon is a good representative of the class of materials that are amorphous or, like semiconductors, become so under treatment [12]. From the point of view of continuum modeling, this fact can also constitute a simplification, while a great deal of information exists that also aids more atomistic descriptions. For all these reasons, the history of IBS silicon nanopatterning reproduces to a large extent the development of our understanding of the technique from a general point of view, motivating our choice for the focus of the present review.

In this article, we thus consider the current status of our understanding of IBS nanostructuring of silicon targets. The work is divided into three main parts that correspond to experimental results, and then to the microscopic and the continuum modeling of the process. This is required, as a proper understanding does not seem possible without addressing the multiscale nature of the phenomenon, in which microscopic processes lead to an evolution of the surface topography that occurs in macroscopic time scales. The article starts with a historical perspective over the field, as substantial changes have occurred in our understanding of the phenomenon in relatively recent times. As a vivid example, after the initial observation of Si dot production by IBS in 2001 [13], the relatively established paradigm for describing their production and related phenomena was described in reviews such as [2,3], and even in an special issue that was devoted to IBS surface nanostructuring as recently as in 2009, see [14] and references

in the same issue. However, such a paradigm has been significantly modified by more recent developments, the most salient of which will be considered in what follows. The review finishes with a discussion of some recent applications of the technique, and with an outlook on future avenues for research in a topic that still remains open and thriving.

2. Historical overview

The capacity to produce submicron and nanometric structures on the surface of different materials by IBS is well known since the pioneering works by Cunningham et al. [15] and Navez et al. [16], published half a century ago. For example, Navez et al. observed the formation of periodic arrays (i.e. a pattern) of ripples, with a typical wavelength smaller than 100 nm, after air bombardment of glass. The ripple orientation was defined by the ion incidence angle with respect to the surface normal, θ, turning from a parallel to a perpendicular mode (i.e. wavevector parallel or perpendicular to the ion beam projection on the surface, respectively) for $\theta \lessapprox 90^\circ$. In those early years, IBS-induced patterns were considered rather as a problem in the field of depth profiling analysis, due to the change of the sputtering yield with the local incidence angle [17,18]. Nevertheless, as mentioned above, their characteristics and potentialities still led Taniguchi in 1974 to propose erosion of solid targets through IBS as a promising nanostructuring technique [1].

After the work by Navez et al., different reports were published describing ripple formation by IBS. However, the next milestone in this field was reached only in 1988 with the seminal theoretical work by Bradley and Harper (BH) [19]. There, the authors explained IBS pattern formation as the interplay between relaxation by surface diffusion and a morphological instability, which, as noted by Sigmund [20], is associated with the dependence of the sputtering yield on surface curvature. This model accounted for the ripple wavelength and orientation observed in the experiments by Navez et al. [16] and has provided an important framework for most experimental and theoretical studies since its publication to this day. Still, the advance that really boosted the field was the report by Facsko et al. [21] on the production by IBS of a highly ordered nanodot pattern on GaSb(1 0 0) surfaces under normal incidence geometry. The relevance of this finding was the promise of an efficient approach for the fabrication of quantum dots arrays [21]. The work by Facsko et al. triggered the experimental pursuit of nanodot production by IBS on other materials and with different equipments and ion energy ranges [3]. An important step forward from the experimental and applied points of view was the nanodot patterning of silicon surfaces, first reported in 2001 by Gago et al. [13]. Thus, the advent of high resolution tools for surface and interface characterization helped to recognize IBS as a method for efficient production of well ordered surface patterns at nano and submicron scales, for a wide range of ion/target combinations.

One of the goals of studies on IBS surface patterning was to assess the universality of the process. As mentioned, this was somehow hinted at by experimental evidences, and was also expected on the basis of the generality of the theoretical BH description. However, a large disparity of experimental behaviors, some of them conflicting, eventually emerged. Thus, for example, already in 1994 Carter et al. [22] pointed out "*the wide range of observations, some conflicting, on repetitive feature development on semiconductors. It is therefore not surprising that there is little understanding of the basic mechanisms which lead to their initiation and evolution*". Such a disparity prevented the supply of reliable data to theoretical models, hampering their consistent development. The interested reader can find an overview of such experimental and theoretical works in Ref. [3].

In spite of this confusing experimental situation, clear progress has been achieved in different areas of the field [2]. First, the understanding of IBS nanopatterning of metallic surfaces has developed substantially (see the excellent review [23], as well as the papers by the group of Valbusa and collaborators). This is a special case, as the surface layers do not become amorphized by the impinging ions, in contrast with the frequent cases of crystalline insulators or semiconductors [12]. On the theoretical side, the linear and anisotropic BH theory has been further extended through incorporation of nonlinearities, in order to account for the full dynamics of the pattern and its stabilization at long times [24–26], and to explain nanodot formation under isotropic conditions [27]. Moreover, an enlarged modeling perspective has been taken with respect to the previous approach in BH's model and its generalizations. While in the latter the time evolution is made explicit for the surface height of the target exclusively, the more recent perspective considers an additional field which accounts for the density of surface species that are not sputtered away, but rather remain mobile along the target surface [28]. The dynamics of this field is coupled to that of the height, allowing for a natural interplay between erosion and surface relaxation. Actually, in a similar spirit more recent models that address IBS of binary materials, or else IBS with concurrent co-deposition of impurities, also couple the dynamics of the height to that of appropriate concentration fields. A detailed survey of the different models developed in this context and their current status is presented in Section 5.

In the last years, and following the works by Ludwig's [29], and Teichert's [30] groups, progress has been also achieved in the experimental elucidation of the reasons for the huge disparity of observations, particularly on silicon surfaces. Specifically, ground-breaking results on the influence of metallic contaminants were reported by Ozaydin et al. [29]. They are shown in Fig. 1, which displays AFM top views of Si(1 0 0) surfaces irradiated under normal incidence by 1 keV Ar^+ ions without (a) and with (b) the simultaneous incorporation of Mo atoms coming from the target-fixing clamps [29]. Clearly, only smooth surfaces were obtained in the absence of metals, whereas the surface was nanopatterned when Mo was present. Moreover, this Mo-assisted nanodot pattern formation was followed in real time by X-ray analysis [29,31]. These studies demonstrated an increase of the average inter-dot distance with irradiation time (coarsening). In these influential works, the authors employed techniques such as Auger electron spectroscopy (AES) and X-ray photoelectron spectroscopy (XPS) to assess the presence of Mo atoms. Although the Mo chemical environment was not explicitly addressed, the authors moreover suggested, for the first time, that the formation of molybdenum silicides could take place, inducing the creation of protected zones with a reduced sputtering yield as compared with their surroundings. Finally, the authors suggested that this preferential sputtering could actually trigger formation of the dots. Since this seminal work, different groups [32–35] have contributed to demonstrate the relevance and potential of metal co-deposition to tune the pattern characteristics. In later studies like these, AES, Rutherford backscattering spectrometry (RBS), and energy dispersive X-ray spectroscopy (EDX) have been used to quantify the surface content of impurities, whereas XPS, electron energy loss spectroscopy (EELS), and X-ray absorption near edge spectroscopy (XANES) have been employed to characterize the chemical state of the impurities themselves.

It should be noted that, during IBS, metal atoms from the ion source itself and/or from the sample surroundings are very likely to unintentionally incorporate to the target surface. Ions can impinge on the vacuum chamber walls or on parts of the sample-holders, causing the simultaneous co-sputtering of metal atoms, that can finally land on the target surface. The systematic design of

experimental setups that explicitly avoids contamination has been done only very recently. The same applies to the characterization of the composition of the irradiated surfaces by techniques which allow to assess or discard the presence of contaminants. This still remains far from being a routine procedure in IBS nanopatterning experiments. Notwithstanding, at present it seems that there is a metal content threshold, roughly around 10^{15} atoms/cm^2 [32,36], to effectively trigger pattern formation. This fact is important as in many systems—for instance, in those where the ion gun operates with a tungsten filament and carbon or molybdenum grids—some contamination from the source is unavoidable. However, in most cases it is smaller than the threshold value that is required for impurities to control the evolution. Moreover, the pattern evolves only if metals are continuously supplied during the irradiation since, as soon as their incorporation is suppressed, the pattern will gradually vanish until a flat surface morphology is obtained [36].

The turning point on the assessment of the key role played by the metal incorporation occurred in 2008, when Madi et al. [37–39] reported a rather systematic and controlled study of Ar^+ IBS nanopatterning of Si surfaces under extremely clean conditions, in which the incorporation of metal atoms was explicitly avoided. This work reported the absence of any surface nanopattern for incidence angles $\theta < 48^\circ$, the formation of parallel mode nanoripples (i.e. with wavevector parallel to the projection of the ion beam) for $48^\circ < \theta < 80^\circ$ and, finally, the formation of perpendicular mode nanoripples for $\theta = 85^\circ$. These findings implied a deep revision of the previous results, in particular those reported on mono-elemental surfaces, and of the previous theoretical understanding of IBS. Note that the BH approach predicted pattern formation for all incidence angles, in particular at normal incidence. Thus, it became evident that pattern formation in silicon surfaces below the critical angle (around 48° for low-energy Ar^+ bombardment [37,38]) was in fact triggered by the incorporation of impurities during the process. One example that clearly shows the change of mind caused on the researchers by this new scenario is the statement by Macko et al. in 2011 [33] concerning pattern observation for $\theta < 45^\circ$: "*All patterns observed in this angular range – in the past, often erroneously interpreted in terms of pure ion beam erosion mechanisms – are just a consequence of unintentional co-deposition of a non-volatile species during erosion, resulting in a two-component surface system*". Hereafter, most recent experiments employ more careful designs and controlled conditions than in earlier times, which is enabling systematic improvements in the modeling of the process. It should be noted that, when the irradiated surfaces are not mono-elemental (such as alloys or multi-elemental materials), effects associated with the different sputtering rates of their components can also be important to the IBS nanopatterning process [40].

As exemplified above, research in this topic has generated a huge amount of studies and reports dealing with different fundamental or applied aspects. Moreover, the focus and aim of these studies have evolved along the last decades as the research advanced and a deeper and fuller insight on the involved mechanisms developed. The present work, which is obviously inscribed within the most recent scenario, intends to provide a meaningful account of the present status of the experimental and theoretical research in the field. However, we will concentrate only on the case of silicon targets. We have made this choice because of the technological relevance of this material and also because it is generally being considered as a sort of model. In addition, it is also paradigmatic system for semiconductor materials. In this regard, we should point out that, as Macko et al. [33] hinted at, multi-component surface systems present peculiarities for IBS processes, mainly related to local changes in the sputtering rates, that could distort the observed behaviors and hamper their proper understanding in some way. Moreover, we will only consider cases in which noble gas ions were employed, since the use of other ions, such as N_2^+ or O_2^+, can lead to local changes in the surface composition and, therefore, result into "abnormal" behaviors. Furthermore, in contrast with a previous account [3], in this paper we do not intend to give a comprehensive overview of all available studies on surface nanopatterning by IBS. Rather, we will mainly focus on the two main experimental aspects (Section 3) that summarize the present capabilities of the technique and, hence, provide the base-ground for the theoretical understanding of the process (Sections 4 and 5):

(i) Recent and past IBS nanostructuring experiments in which impurities do not play a dominant role, with a special focus on the dependence of the pattern formation process on the ion incidence angle, ion energy, and ion fluence (Section 3.1). To address this study we have to assume a criterion for the consideration of works performed in the past, before the community had become aware of the key role of metal impurities. This task is difficult because, as mentioned, many reports lack a compositional characterization of the nanostructured surfaces. Thus, we have to use an *a posteriori* criterion to consider that a given study corresponds to an impurity-free case. In the light of the experiments in [37–39], we will take this to be the existence of a non-zero critical angle

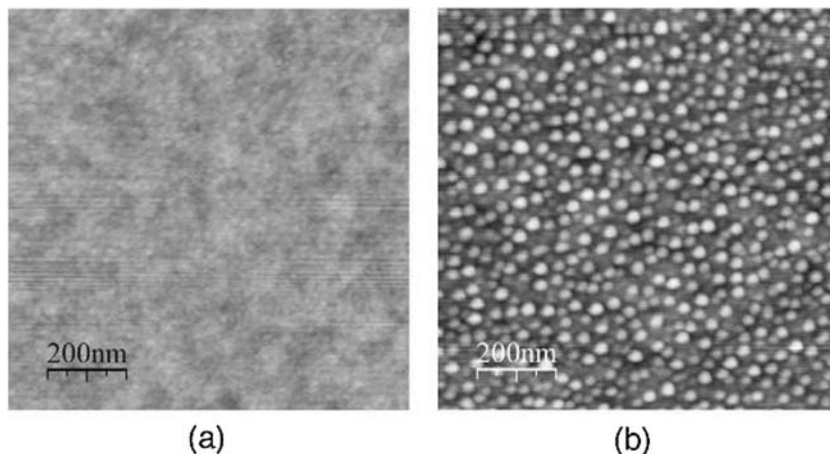

Fig. 1. Top view AFM images of Si(1 0 0) surfaces after irradiation under normal incidence by 1 keV Ar^+ without (a) and with (b) Mo seeding. Clearly, the surface remains smooth unless Mo impurities are added during the irradiation, producing in this case a nanodot pattern. Reprinted with permission from [29]. Copyright 2005, AIP Publishing LLC.

for surface nanopatterning. We do believe that in this way the resulting scenario becomes more consistent, regretfully at the price of leaving out studies that could have been included if a different criterion had been assumed.

(ii) Experiments done during the last few years that have allowed to assess the key role of impurities for IBS nanopatterning of silicon, mainly through metal co-deposition (Section 3.2). A particular emphasis will be made on the description of very recent systematic experiments that try to elucidate the physical mechanisms operating under these conditions. It should be noted that, while the presence of metals during IBS was initially considered as a nuisance, now it is attracting many researchers as a new tool to tune pattern properties and to develop new structures [33].

Finally, although some important issues have already been advanced in this chronological overview, they will be described in more detail in the following sections, due to their important role in the field.

3. Experimental results

3.1. Impurity-free patterning

As described in Section 2, the inadvertent presence of impurities is a relevant issue in IBS nanopatterning of silicon surfaces that has been considered only recently. This fact has motivated studies under negligible or low contamination environments in order to develop further insight and control of the nanostructuring process. For such a purpose, experiments have been carried out with extreme care, even covering the sample surroundings with silicon pieces in order to avoid the incorporation of any foreign element during the irradiation. Even so, special attention should be paid to disregard the influence of secondary beams, such as silicon atoms which are sputtered from these covering parts [41]. The pioneering works by Madi et al. [37–39,41] under this impurity-free configuration have shown that, for Ar^+ bombardment of silicon in the 200–1000 eV range, patterns only emerge on the surface above a critical angle of ion incidence, $\theta_c \simeq 48^\circ$. Moreover, only ripple patterns are produced under impurity-free conditions. In agreement with Navez et al. [16], the ripple patterns have a wavevector parallel to the ion beam projection in the 48–75° range [Fig. 2(a)] whereas, for more glancing incidence angles, small perpendicular-mode ripples were produced [Fig. 2(b)]. This fact is summarized in the phase diagram of Fig. 2(c) where, in addition, we can see that θ_c seems to be energy-independent within the sampled parameter range.

Based on the results of Fig. 2 and as discussed in Section 2, among the extensive literature on Si we have considered experimental works as having been carried out under low or no impurity contamination based on two premises: first, there should be a non-zero critical angle for pattern formation and, second, only ripple patterns should be observed. In fact, *in-situ* studies have demonstrated that the silicon surface is smoothened by irradiation with 100–500 eV Ar^+ ions under normal incidence and controlled conditions [42,43]. The lack of pattern formation below a threshold angle was also hinted at in earlier works on ripple formation in silicon [44,45,22,46,47]. In 2001 Carter also noted in [48] that "*in the case of Si particularly, there seems to be a low-energy cut-off, in the region of 10 keV, below which inert gas ion irradiation does not produce ripples*", which has been contradicted by the experimental evidences gathered in more recent years. At the same time, Carter proposed [48] that there should not be ripple formation for $\theta < 45^\circ$. Even as recently as in 2013 [49], it has been reported than no patterning is produced on silicon surfaces under 8 keV Ar^+ irradiation at $\theta = 60^\circ$, well above the expected (or typical) critical angle (~45°). The authors of this work also claim that impurity-induced chemical effects are crucial for ripple formation.

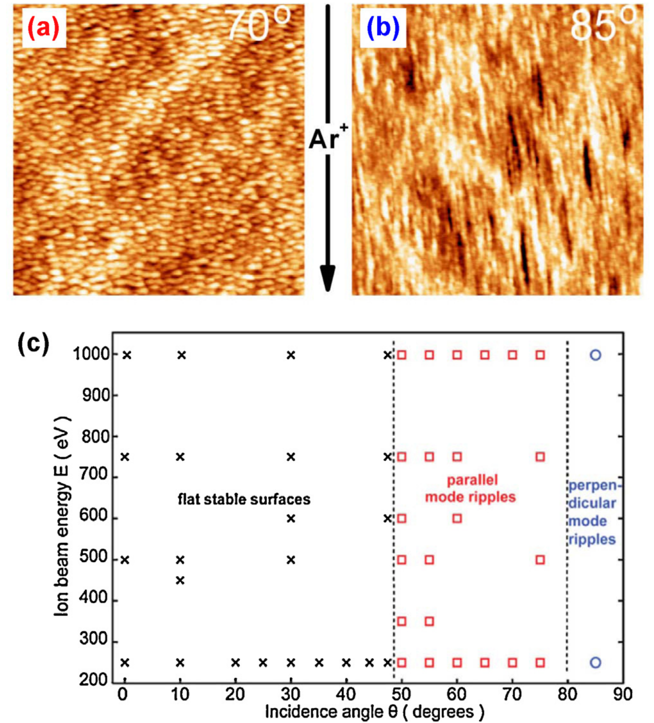

Fig. 2. AFM 2 μm × 2 μm images showing the morphology of silicon surfaces after 250 eV Ar^+ irradiation at room temperature for (a) $\theta = 70^\circ$ and (b) $\theta = 80^\circ$. The projection of the ion beam on the surface is indicated by the arrow, revealing the formation of parallel (a) and perpendicular (b) mode ripples. Adapted with permission from [39]. Copyright 2009, IOP Publishing. (c) Phase diagram for pattern formation on Si(1 0 0) by Ar^+ IBS in the absence of impurities and secondary scattering effects. The different signs refer to the observed morphologies: flat (×), parallel mode ripples (□), and perpendicular mode ripples (∘). Reprinted with permission from [41]. Copyright 2012, Elsevier.

As noted above, nowadays the relation among different experimental results in IBS pattern formation seems more clear. In this section we aim to show the most recent or systematic studies done on Si. We will distinguish between studies performed with low- (< 10 keV) and medium-energy (10–200 keV) ions. The reason for this is that different ion-induced effects may appear in each energy range, which are governed by the ion–solid interaction [50], and may influence the pattern formation and mechanisms. Particularly, medium-energy ions lead to larger penetration depths (ion range), induced-damage (amorphization), or sputtering yields. In each case, we will give details on the most systematic studies addressing issues such as pattern dynamics and the dependence of the pattern properties on variables like temperature, ion beam incidence angle, and ion energy.

3.1.1. Low-energy (< 10 keV)

In the last decades, many studies on Si have been performed in the low energy range. Such an extensive literature is mainly due to the relative ease in the access to low-energy ion sources and their implementation in many vacuum systems for surface analysis and thin film growth. On the contrary, studies with medium-energy ions are scarcer since they require costly medium-scale facilities that are not so readily accessible. For a detailed survey of the literature see [2,3]. Here, we focus on works performed under oblique ion incidence, since the surface remains flat for $\theta < \theta_c$. Hence, all the patterns described in this section will be rippled structures. There are, however, some especial cases in which ordered Si nanodots can be obtained for very low levels of impurities [51–53] or on clean targets [54]. These examples are

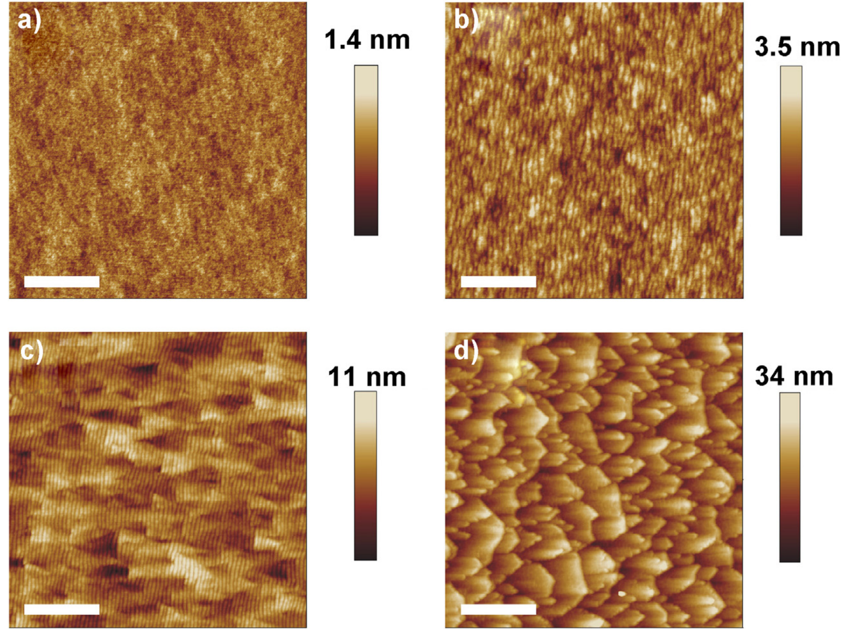

Fig. 3. Experimental AFM morphologies after Ar^+ irradiation of Si(1 0 0). All the images are obtained for a constant fluence of 5×10^{17} ions/cm^2, ion flux of 0.3 mA/cm^2, ion energy E = 700 eV, and at angles of incidence (a) $\theta = 45°$, (b) $\theta = 55°$, (c) $\theta = 65°$, and (d) $\theta = 75°$. Note the absence of pattern formation at $\theta = 45°$ in (a). Lateral size is 2 μm for all the panels, with ions arriving from right to left in all cases; white bars represent 400 nm.

interesting for device applications in which nanostructured impurity-free silicon surfaces are required. In the works by El-Atwani et al. [51–53], nanodots are obtained at normal incidence by employing several thin metal-coated Si substrates. Even after removing all the metallic impurities, the nanostructures persist for some time before the pattern begins to smooth out. In the work by Chowdhury et al. [54], pure Si nanodots are obtained using a different approach. Specifically, the sample is bombarded at a grazing angle (75°) and simultaneously rotated to induce a hexagonal array of nanodots.

The remainder of this section focuses on rippled structures whose features depend on a number of experimental parameters.

Dependence on the ion beam incidence angle. In this paragraph we consider works that have tried to reproduce and extend the results by Madi et al. [37,38], and works previous to the latter that fulfill our "impurity-free" criterion. In particular, the existence of a non-zero critical angle, as depicted in Fig. 2, has been also confirmed by other groups working in the low energy range [55–58]. In general, as shown in the AFM images of Fig. 3, clear ripple patterns are mostly observed for $\theta > 50°$ for Ar^+ bombarded surfaces. However, as discussed in the next point, the patterning dynamics is faster for higher values of θ. Therefore, the observation of clear patterns closer to the threshold angle may require longer irradiation times than those normally considered.

These results have been also assessed by means of *in-situ* grazing incidence X-ray scattering (GISAXS) studies [59–61]. Previously, this synchrotron technique had been successfully applied to study both *in-situ* and *ex-situ* nanopattern formation during IBS (see a review in e.g. [62]) where, under the experimental conditions that we are considering, the scattering pattern is proportional to the height structure factor. Remarkably, in [59–61] GISAXS analysis has been shown to provide even more detailed information. Beyond characterizing the onset of pattern formation, such detailed properties can be directly compared with continuum models in order to validate/disregard proposals on the main physical mechanisms acting in the system.

Under pattern-forming conditions and starting out from a flat target, at early irradiation times each Fourier component of the surface height field $h(x, y, t)$ grows exponentially in time as $h_{\mathbf{q}}(t) \propto \exp(\omega_{\mathbf{q}} t)$, where $\mathbf{q}$ is wave-vector [63]. In general, the growth rate $\omega_{\mathbf{q}}$, usually called *linear dispersion relation*, is a function of $\mathbf{q}$. Note, any value of $\mathbf{q}$ that makes $\omega_{\mathbf{q}}$ positive leads to amplification of the corresponding Fourier mode, which is termed *unstable*. For small values of the fluence (known as the linear regime, for reasons to be discussed in Section 5), the typical wavelength of the pattern ℓ becomes inversely proportional to the magnitude of that wave-vector $\mathbf{q}_*$ for which $\omega_{\mathbf{q}}$ takes its maximum positive value. As will be discussed later in Section 5, the functional dependence of the linear dispersion relation with $\mathbf{q}$ is an important property of continuum models of the process. Thus, the direct measurement of $\omega_{\mathbf{q}}$ in [59–61] is a very important result, as it provides in particular a strict constraint on the types of models which can be relevant to the experimental system.

Specifically, in [59], *in-situ* GISAXS was employed to analyze the surface morphology of Ar^+ IBS of Si targets, along the direction of the wave-vector $\mathbf{q}$ which is parallel to the ion beam projection on the surface, q_x. As already mentioned, see Fig. 3, this study revealed that the surface was unstable (i.e. it was prone to the formation of "parallel" ripples) above a certain critical angle of incidence, $\theta_c \simeq 48°$ to the target normal. Fig. 4 (top panel) shows the linear dispersion relations measured for parallel modes at different values of θ. The surface is (un)stable when the growth rate, $R = \omega_{\mathbf{q}}$, is (positive) negative, patterns forming in the unstable case only. Note how the linear dispersion takes on positive values indeed only for $\theta > 48°$. Later, this study was completed by addressing the surface evolution in two dimensions and finding that, below 80°, the surface was always stable for wave-vectors perpendicular to the ion beam projection (wave-vector component q_y) [60], see Fig. 4 (bottom panel). Finally, the same approach has been also used to extract similar information for other ion-target combinations, as done for Kr^+ irradiation of germanium (Ge) [61]. The particular forms of the dispersion relations obtained will be discussed later in the context of continuum models, see Section 5.

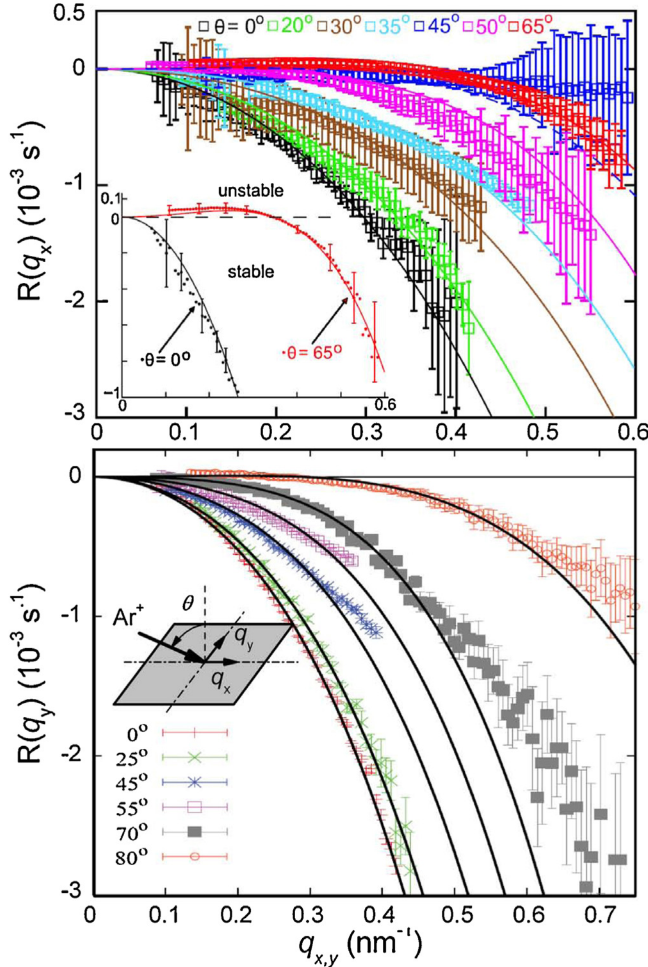

Fig. 4. Experimental dispersion relation for wave-vectors parallel (top) and perpendicular (bottom) to the ion beam projection on the target surface (see bottom inset). The surface is (un)stable when the growth rate, $R = \omega_{\mathbf{q}}$, is (positive) negative. Pattern formation (instability) only occurs for $\theta > 48^\circ$ (see top inset). Adapted with permission from [59,60]. Copyright 2011, American Physical Society.

An interesting and novel aspect regarding the dependence of the pattern on θ is the ambiguity on the threshold value, θ_c. For example, the $\theta_c = 48^\circ$ value reported by Madi et al. for the case of Ar^+ irradiation could be slightly closer to 45°, based on experimental and theoretical considerations [58], see below. Further complexity has been recently added since IBS with other inert ions indicates that θ_c may not be universal. For example, larger θ_c values have been found for low-energy Xe^+ irradiation on silicon [64]. Also, the value of θ_c may differ if other monoelemental targets are considered, such as Ge [61,65]. Therefore, establishing the value of the critical angle for different ions/target combinations remains to be systematically explored, and would provide relevant information about the mechanisms for nanopatterning.

Patterning dynamics (fluence dependence). Typically, three patterning regimes can be distinguished during ripple formation by IBS [37,38,56,58]. As an example, the evolution of a Si(1 0 0) surface under 700 eV Ar^+ irradiation at $\theta = 55^\circ$ is shown in Fig. 5. First, there is an initial stage where the surface rms roughness, W, increases exponentially and the ripple wavelength, ℓ, stays constant. This is followed by a second stage where the increase in W is slower, and is accompanied by a clear increase (coarsening) of ℓ. This stage ends in the final asymptotic stabilization of both W and ℓ. The first region is known as the *linear regime*, whereas *coarsening* and pattern stabilization features are the result of the

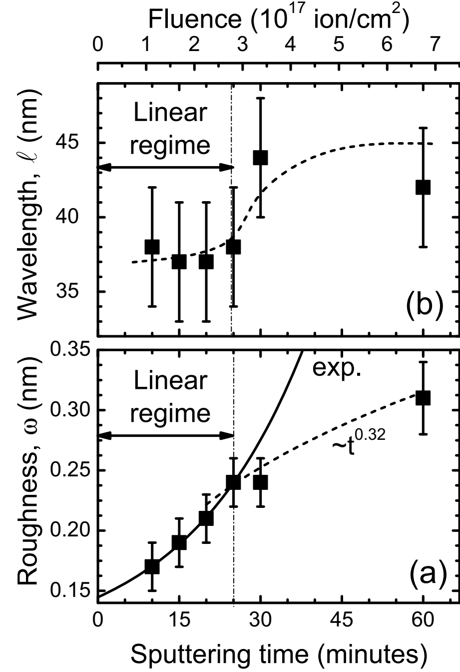

Fig. 5. Time evolution (fluence) of the surface roughness (a) and ripple wavelength (b) for Si(1 0 0) surfaces irradiated with $E = 700$ eV Ar^+ flux of 0.03 mA/cm^2 and $\theta = 55^\circ$. The extent of the linear regime is indicated by the dot-dashed vertical line. Adapted with permission from [58]. Copyright 2012, American Physical Society.

contribution from non-linear effects that control the pattern dynamics at longer times, see Section 5. As a *rule-of-thumb*, the pattern is within the linear regime when the profile along the ripple wavevector presents a sinusoidal and symmetric shape. A typical example of such a ripple morphology is shown in Fig. 3(b). On the contrary, the morphologies shown in Fig. 3(c) and (d) are clear indications of non-linear dynamics. While in (c) long-range morphological features perpendicular to the ripple morphology overlay it, in (d) the ripple line-shape becomes asymmetric and faceted.

In order to properly compare the different morphologies, it is important to assess the extent of the linear regime for each experimental condition. This is because the behaviors of W and ℓ with θ change, depending on the time regime in which the experiment is considered [58]. This issue will be discussed with more detail in Section 5.3. In general terms, the dynamics proceeds at a slower pace for θ values closer to θ_c; hence, the linear regime should last longer. This is the reason why in Fig. 5 we show the dynamics for a relatively low angle $\theta = 55^\circ$, so that the linear regime can be readily appreciated. Very recent experiments from Basu et al., carried out with 500 eV Ar^+ ions for different incident angles from 51° to 72.5°, have also concluded that there is an intrinsic timescale for the linear regime [66]. Moreover, this timescale was found to increase for angles close to θ_c, in agreement with recent results from continuum models, see a discussion in Section 5.

In general, different results will be obtained for morphologies which are obtained under a given fluence condition but for different angles: a fluence value that corresponds to the linear regime for $\theta \gtrsim \theta_c$ can correspond to the nonlinear regime for a more glancing incidence angle. Such a difference in behaviors is illustrated in Fig. 6, where W is very small and almost constant in the linear regime for θ values above the threshold for ripple formation. On the contrary, the value of the roughness increases sharply for $\theta > 65^\circ$ for a fixed fluence (as the sputtering yield also does, not shown), as a result of enhanced non-linear contributions

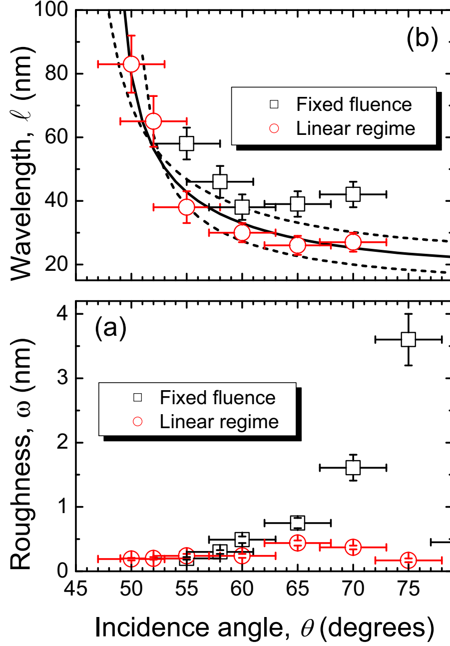

Fig. 6. Dependence of (a) roughness, W, and (b) wavelength, ℓ, on incidence angle θ for experiments performed at a fixed fluence of 5×10^{17} Ar^+/cm^2 (black squares), or for different fluences such that linear behavior holds for each θ (red circles), for E = 700 eV, and Ar^+ fluxes of 0.03 and 0.3 mA/cm^2, respectively. The solid line in (b) is a fit to Eq. (9), the dashed lines corresponding to the same fit but assuming a $\pm 3^\circ$ uncertainty in θ (see Section 5.3). When error bars are not plotted, they are equal to or smaller than the symbol size. Reprinted with permission from [58]. Copyright 2012, American Physical Society. (For interpretation of the references to colour in this figure legend, the reader is referred to the web version of this article.)

in this range of incidence angles. Likewise, experiments performed either at a fixed fluence or for a varying fluence that guarantees linear behavior for each θ, lead to different dependencies of ℓ with θ and ion energy, E. Such a result will bear importance to the contrast between experiments and theoretical models, see next item.

With respect to the evolution in the non-linear regime, the dynamics have been rarely studied under experimental conditions which are explicitly controlled with respect to contamination issues. The most relevant work, to our knowledge, is that performed by Keller et al. [67,68]. More or less simultaneously with Madi et al. [37,38], these authors also demonstrated the dependence of the pattern with the angle of incidence [67]. In their study, the Si(1 0 0) surface was irradiated with 500 eV Ar^+ ions impinging at $\theta = 67^\circ$. The main result is the development of an anisotropic surface scaling behavior at high ion fluences, ascribed to the formation of a two-mode ripple pattern. Thus, during the linear regime, parallel mode ripples are quite symmetric and similar to those in Fig. 3(b). However, as irradiation time increases, larger corrugations form and overlay the previous orthogonal ripples. These corrugations become more pronounced with further irradiation, until they dominate the surface morphology, as in the case of Fig. 3(c). For comparison, see the images in [67]. The anisotropy in this two-ripple mode regime is evident in Fig. 7, where typical surface profiles along parallel and perpendicular directions to the ripple wave-vector are shown. In this case, the profile is extracted from a broad-view, 5 μm AFM image from the same sample as that shown in Fig. 3(c). The lateral correlations of the surface roughness seem different along the two directions, particularly at large length scales.

Another relevant result on the non-linear dynamics of the pattern is the formation of faceted ripples for glancing ion incidence ($70^\circ < \theta < 80^\circ$). For instance, see the morphology in Fig. 3(d) for $\theta = 70^\circ$. This stage has been recently investigated by

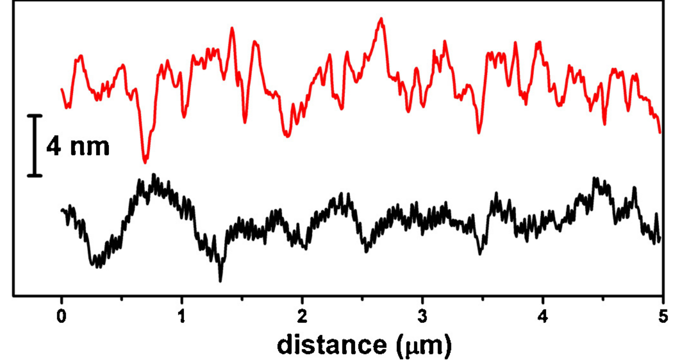

Fig. 7. Surface profiles of the sample displayed in Fig. 3(c), taken along the parallel (bottom) and perpendicular (top) directions to the ripple wave-vector.

Basu et al. [57,69]. They found, in analogy with the case of medium-energy ion bombardment (see Section 3.1.2), that shadowing effects are playing a critical role for the development of such morphology. This geometrical effect will be described in more detail in Section 3.1.2 since it becomes more evident at higher E, where both W and ℓ are larger. Very recently, Engler and co-workers [70] have studied the ripple formation and evolution on silicon surfaces under 2 keV Kr^+ irradiation at $\theta = 63^\circ$ and 75°. The experiments were performed under ultra-high-vacuum conditions and the irradiated surfaces were studied in situ by Scanning Tunneling Microscopy (STM). For both conditions a similar parallel-ripple formation process occurs during the initial low-fluence regime. In contrast, in the high-fluence regime the behavior depends strongly on the value of θ. For $\theta = 63^\circ$, the evolution is similar to that reported by Keller et al. [67]. However, for $\theta = 75^\circ$ quite a different morphology develops, which consists of a roof-tile structure with a strong coarsening behavior. Interestingly, the angles of this structure are close, but not equal, to those expected if shadowing effects dominate. In this sense, the authors invoke a non-local effect attributed to Hauffe [71] to explain the observed behavior. This mechanism consists of the reflection of an important fraction of the ions which impinge on the downwind face of the ripples. These reflected ions hit the next upwind face, where they do cause sputtering. Hauffe's argument has been also invoked to explain ripple dynamics on Ge surfaces irradiated by 1.2 keV Xe^+ at 75° [65]. Finally, an interesting observation in [70] is that the angle of the downwind ripple face with respect to the flat silicon surface remains constant for incidence angles in the 58–77° range.

As a final remark, an interesting question on the evolution of the ripple pattern is its lateral propagation [26], that allows for a certain analogy with the propagation of macroscopic ripples on e.g. sand dunes [72]. Indeed, Habenicht et al. [73] did observe such a propagation in *real time* with a focused ion-beam (FIB) column attached to a scanning electron microscope (SEM). They observed that the ripples propagate parallel to the ion beam, in further support to the analogy with the patterns on Aeolian sand dunes, which drift in the direction of the wind. However, this experiment was carried out with 30 keV Ga^+ at $\theta = 30^\circ$. Therefore, the potential influence of Ga impurities as a trigger for pattern formation should be taken into account. Recently, the propagation of ripples has also been verified by irradiation with inert ions by Hofsäss et al. [74]. In this case, the authors used markers (grooves) on the target to follow the movement of characteristic pattern features, as shown in Fig. 8. Remarkably, they observed that the pattern propagates in both directions, opposite to, or in the same direction as the projection of the ion beam, depending on θ. At $\theta \simeq 67^\circ$ the pattern remains more or less static. This is a relevant finding since the ripple propagation and the sign of its velocity can

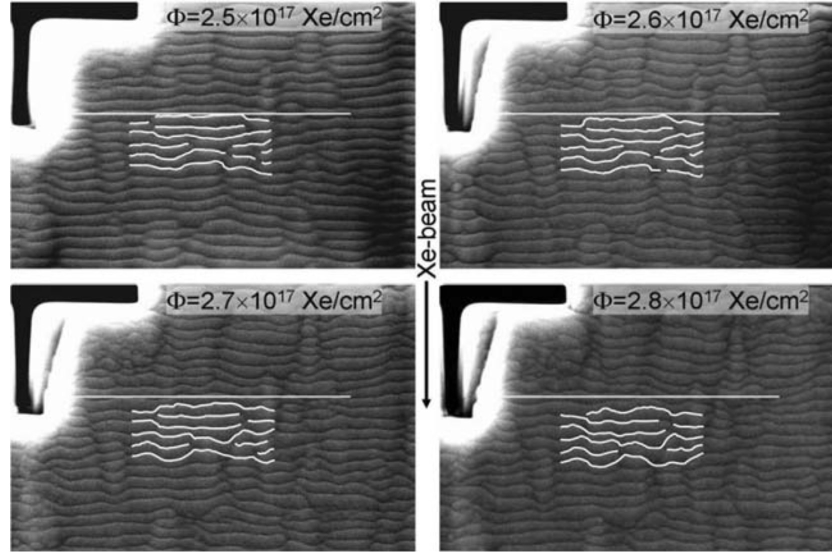

Fig. 8. SEM images of 3 μm × 2 μm size from Si samples irradiated with 10 keV Xe^+ ions at 70° at different fluences (see labels). The projected direction of the ion beam on the surface is indicated by the vertical arrow (from top to bottom). The ripple propagation occurs in the direction of the ion beam. Reprinted with permission from [74]. Copyright 2013, American Physical Society.

be used as additional inputs to validate the different mechanisms and models of pattern formation, which will be reviewed in Sections 4 and 5.

Dependence on ion energy. As noted earlier [3], the study of the dependence of the pattern characteristics on the ion energy is quite interesting because it can be also used to further validate experimentally predictions from different theoretical models [75]. For instance, most of the results which are available so far yield power-law behaviors, $\ell \sim E^m$, where usually $0 < m \leq 1$. These can not be reproduced by e.g. a BH framework in which relaxation is by thermal surface diffusion (implying a decaying behavior $\ell \sim 1/E^n$ [26]), which suggests the need to consider alternative, non-thermal relaxation mechanisms [58], see Section 5.

After the work by Madi et al. [37,38], the effect of E on the pattern characteristics has not been addressed specifically. In

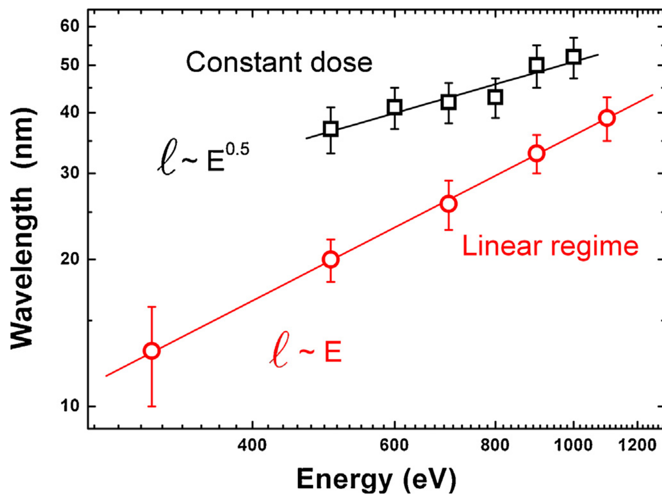

Fig. 9. Ripple wavelength dependence on the ion energy for fixed fluence experiments (black squares) and within the linear regime (red circles), for 1 keV Ar^+ irradiations at $\theta = 65°$. The solid lines are fits to power laws with the indicated exponents. Reprinted with permission from [58]. Copyright 2012, American Physical Society. (For interpretation of the references to colour in this figure legend, the reader is referred to the web version of this article.)

Fig. 9, a power-law behavior is indeed obtained for both types of experimental conditions explained above, that is, fixed fluence or within the initial linear regime. Moreover, the value of $m \simeq 0.5$ derived under fixed fluence conditions agrees with previous experimental results [3]. However, the value of this exponent can change, turning into a linear dependence ($m = 1$), if morphologies are considered systematically within the linear regime. Moreover, recall that the pattern dynamics is slower for higher E. Therefore, the linear regime lasts longer under such conditions. With respect to other materials, it is useful to consider experimental results obtained for carbon-based monoelemental targets, such as highly oriented pyrolytic graphite (HOPG) or diamond surfaces. Thus, Habenicht et al. [76] found $m \simeq 0.66$ for HOPG bombarded by Xe^+ ions at constant fluence and $\theta = 30°$. In contrast, Takahiro et al. [77] found $m = 1$ for both HOPG and diamond surfaces bombarded with Xe^+ ions at $\theta = 60°$ and a fixed fluence. Finally, for amorphous carbon irradiated with Xe^+ ions at $\theta = 60°$ and within the linear regime, a linear dependence of the ripple wavelength with ion energy [78] has been recently reported. All these values can be relevant in order to validate the different theoretical models, as will be discussed in Section 5.

Influence of the target temperature. Although temperature has a strong effect on pattern formation by IBS [3], studies are scarce under controlled impurity-free conditions. Thus, in view of the recent advances, the influence of temperature on the value of θ_c is an open question that should be systematically addressed. Some results were contributed by Brown and Erlebacher back in the early 2000s [79,80]. These experiments were performed under well controlled conditions in ultra high vacuum; hence, no impurities were incorporated during the irradiation. Here, Si(1 1 1) surfaces were irradiated with an Ar^+ ion-beam impinging at $\theta = 60°$, for ion energies between 250 and 1200 eV, ion fluxes between 0.38 and 3.0 mA/cm^2, and temperatures in the 500–750 °C range. Note that these temperatures are sufficiently high that recrystallization of the ion-damaged silicon occurs much faster than amorphization during individual ion impacts [81]. This is an important difference with respect to other experimental reports, and should likely play a key role in the specific behavior observed. Brown and Erlebacher studied the evolution of the pattern *in-situ* by UV light scattering spectroscopy (LiSSp) and *ex-situ* by AFM. The most striking

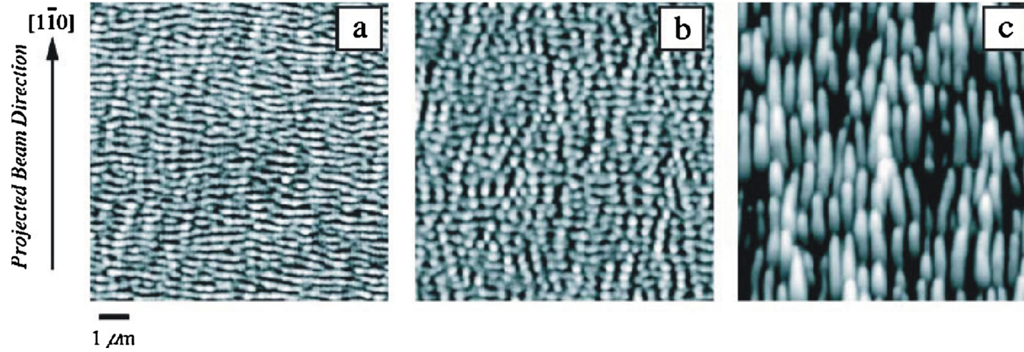

Fig. 10. AFM images showing the morphological evolution of 500 eV Ar^+ ion sputtered Si(1 1 1) at $\theta = 60^\circ$, $T = 637\,^\circ$C and ion flux of 0.75 mA/cm^2. (a) At t = 1800 s, parallel ripples form. (b) At t = 3600 s, perpendicular ripples appear, leading to a two-dimensional morphology. (c) At a much larger ion fluence, t = 10,260 s, perpendicular-mode ripples develop. Reprinted with permission from [80]. Copyright 2005, American Physical Society.

observation concerns changes with ion fluence. As Fig. 10 shows, at 637 °C the ripple pattern evolves from a parallel mode to a sort of bidimensional ripple pattern (i.e. with the contribution of both parallel and perpendicular ripples). Finally, at large fluences, a clear perpendicular-mode pattern remains. While this rotation of the pattern with time had not been observed before, it has been recently found in related theoretical models [82,83]. In the experiment, both ripple modes were observed to coarsen with time. Regarding the wavelength dependence on ion energy, for parallel mode ripples formed at 717 °C, it was found that $\ell \sim E^{-0.45}$, whereas for perpendicular mode ripples no clear trend was observed.

3.1.2. Medium-energy (10–200 keV)

The case of silicon nanorippling by medium-energy IBS is more difficult to organize under the framework of this review, since many of the reports date back to the last century. At that time, the effect of impurities had not yet been addressed in the sense we are considering. In particular, most of those reports lack a chemical analysis of the irradiated surface. However, ion beam irradiation in the medium-energy range is normally done with an ion implanter, which fulfills certain requirements that allow us to include these works within the label of impurity-free patterning, see Section 2. Specifically, filtered beams are usually employed, in which the selected ion is specified by switching magnets located in the beam line, just after the ion source. In addition, the beam is usually quite collimated and is scanned over a controlled area of the target. Thus, the incorporation of contaminants, either from the ion beam itself, from the beam-line walls, or from the target surroundings, is not likely to occur. Note also that these equipments have been extensively used in Microelectronics, where already a tiny amount of impurities can ruin the devices. In any case, as in the low energy case, the same criteria related to the existence of a non-zero critical angle should apply. As examples that support such a criterion, we can mention again the works by Carter et al. [45,22,46].

Dependence on the ion beam incidence angle. For Si irradiation in the medium-energy range, no studies exist on the dependence with θ which are as detailed as those reported for the low-energy case. However, some early studies proposed that the threshold angle should be below 45° for 10–40 keV Xe^+ ions [48,46], and below 55° for 30 keV Ar^+ ions [84]. Very recently, Garg et al. [85] have also reported that the threshold angle for 60 keV Ar^+ ions is larger than 30° and lower than 45°. These trends contradict in some way those observed for low-energy ions, where Xe^+ has a larger θ_c than Ar^+ [64], being closer to 45° in the latter case [37,38,58]. This suggests that some dependence of θ_c might exist with the ion species and the energy range. A relation could also exist with very early reports on the dependence of the pattern properties with the target temperature for the case of Ar^+ and Ne^+ irradiations [17,86]. In these cases, it was necessary to reduce the temperature in order to pattern the surface with lighter ions, in contrast e.g. with the case of Xe^+. We should point out that, in the recent study by Garg et al., the ripple wavelength decreased with increasing θ values, as is the case for low ion energies [37,38,58]. Finally, to our knowledge the only report on the formation of perpendicular mode ripples for IBS close to grazing incidence is due to Carter et al. in 1977 [44].

These results indicate that a deeper study should be envisaged, after the experience gathered during all these years. Issues such as the determination of the threshold incidence angle for nanostructuring, its dependence on ion species, ion energy and temperature, merit to be addressed. As already noted, at these relatively high ion energies, other ion-induced effects different from those operating at low ion energies, could come into play. In this sense, new systematic experiments in this ion energy range are welcome, since they would contribute to deepening our understanding of the IBS nanopatterning process.

Patterning dynamics (fluence dependence). The first studies to be considered here are the earlier works by Carter et al. [46,87], where silicon surfaces were irradiated with a 40 keV Xe^+ ion beam impinging at 45°. The main results are displayed in Fig. 11. In this work, the ripple amplitude was observed to increase linearly with ion fluence in the whole experimental window. In contrast, while initially ℓ was time-independent, a coarsening regime followed later, finally ending in saturation at the largest ion fluences. The authors performed the same experiment using Xe^+ ions with 20 keV and 10 keV; the observed wavelength was identical to that reported for 40 keV, but the growth rate of the ripple amplitude was smaller and started to increase later for lower energies, see Fig. 11.

It should be noted that coarsening is seen to occur when the pattern morphology changes from a sinusoidal to a faceted one, with ripple sides aligned normal and parallel to the ion flux. The origin of such a bimodal morphology (each ripple side has a well-defined slope) was explained by Carter in terms of shadowing [88]. This geometrical effect takes place when the local slopes of a sinusoidal ripple structure become so high that part of the upstream face is shadowed from the incident ion beam by the preceding peak. Under these conditions, the sinusoidal wave pattern would evolve towards a faceted or saw-tooth morphology. Assuming a perfectly sinusoidal morphology with an amplitude proportional to the surface roughness, W, and a wavelength ℓ, there is a threshold value for the aspect ratio W/ℓ of the ripples above which geometrical shadowing becomes operative. Such a threshold depends on the incidence angle, θ: for glancing angles shadowing occurs for smaller aspect ratios than for θ values

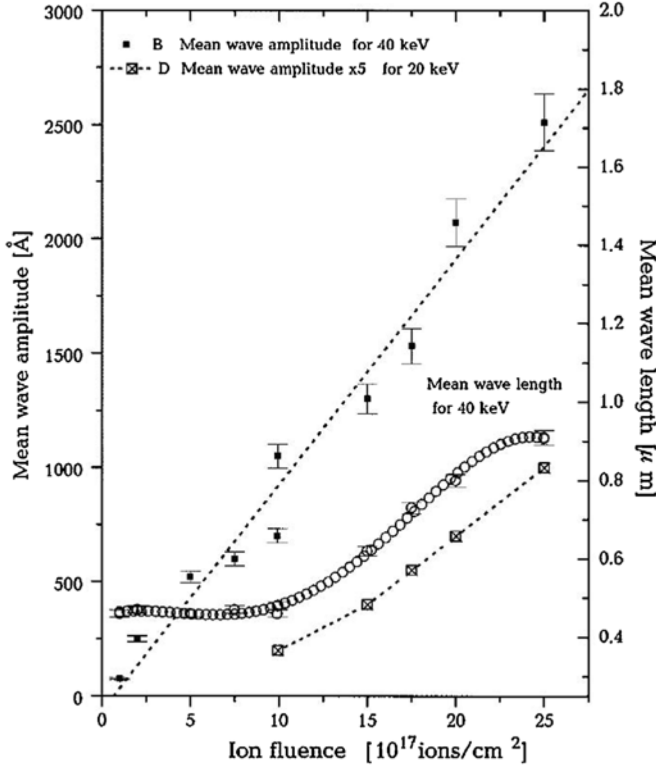

Fig. 11. Ripple amplitude and wavelength as a function of ion fluence, for a Si surface irradiated at $\theta = 45^\circ$ with Xe^+. Reprinted with permission from [46]. Copyright 1996, American Physical Society.

closer to normal incidence. It can be shown [88] that shadowing occurs if

$$2\sqrt{2\pi}\frac{W}{\ell} \geq \tan\left(\frac{\pi}{2} - \theta\right) \tag{1}$$

More recent studies have been reported by Chini et al. [89,90]. Their experiments consisted in irradiating Si surfaces by 60 keV Ar^+ ion beams impinging at 60° with high (175 μA/cm²) or low (18 μA/cm²) ion flux. The results are shown in Fig. 12. At the higher flux, the surface roughness initially increases as $W \sim t^{0.76}$, after which the scaling behavior changes to $W \sim t^{0.27}$. Also, in agreement with Carter et al. [46,87], ℓ was initially constant, while coarsening $\ell \sim t^{0.64}$ occurs later, again approximately correlated with the onset of geometrical shadowing. Finally, a regime in which $\ell \sim t^{0.22}$ was attained, which coincides with the late time regime observed for the roughness. These data were interpreted on the basis of the shadowing effect described above. In fact, in the asymptotic regime, both W and ℓ increase at the same rate, which indicates the sympathetic lateral and vertical growth of the faceted morphology already described by Carter [88]. For the lower ion flux it was possible to observe only the first two regimes, which were similar to those observed at higher flux in terms of the temporal dependencies of both W and ℓ. Wavelength coarsening also appeared when shadowing effects were operative, which occurred at a longer fluence under this flux condition. In a later study by the same group [84], the dynamics of the ripple pattern was analyzed under the same angle and low flux conditions, but using a lower energy, 30 keV. Qualitatively, the same behavior was found, but with smaller values for W and ℓ.

Another interesting and recent result related to the pattern dynamics has been published by Kumar et al. [91]. In their work, the authors show how the dynamics is altered by the *pre-amorphization*

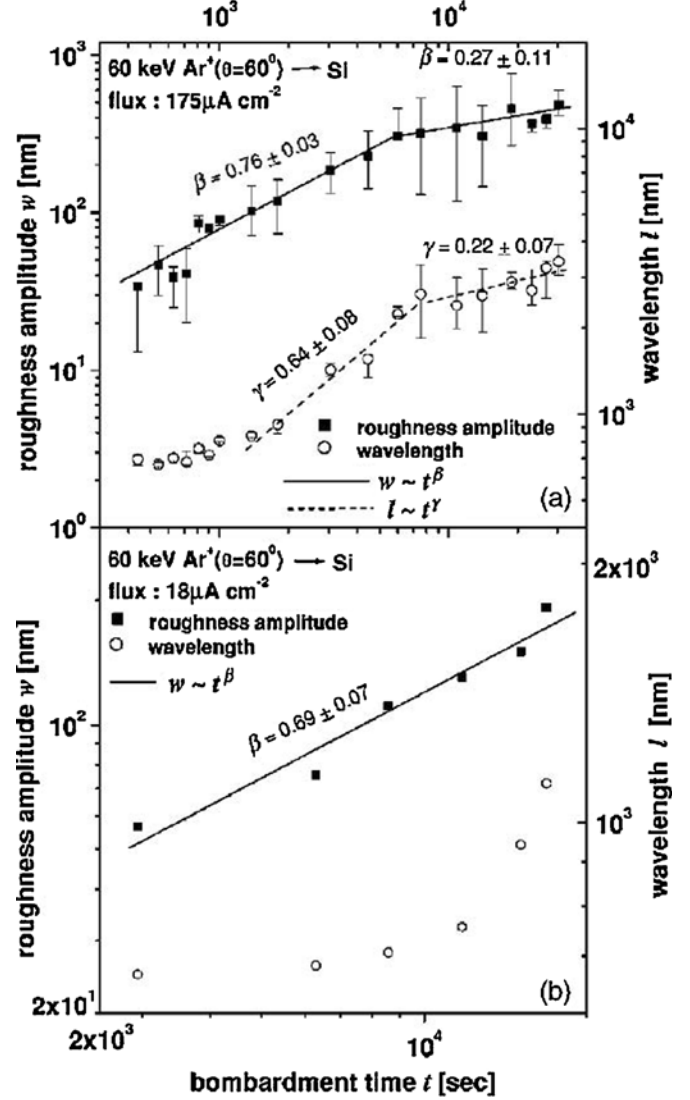

Fig. 12. Ripple wavelength, ℓ, and surface roughness amplitude, W, as a function of bombardment time. Ar^+ flux (a) 175 μA/cm² and (b) 18 μA/cm². Reprinted with permission from [90]. Copyright 2009, IOP Publishing.

of the surface. The results from this experiment are summarized in Fig. 13. Here, 50 keV Ar^+ ions are used to irradiate the silicon surface at $\theta = 60^\circ$ (left column) and at normal incidence (right column), for a relatively low fluence which is high enough that the surface becomes completely amorphized. Remarkably, the subsequent dynamics for ripple formation at $\theta = 60^\circ$ depends on the initial condition: the ripple amplitude is strongly attenuated in the *pre-amorphized* target at normal ion incidence, for which the initial amorphous layer is thicker[1]. This finding has been used by the authors to suggest that the *amorphous/crystalline (a/c)* interface may play a relevant role in the ripple formation.

The implications of the ripple microstructure in the pattern formation and dynamics with medium-energy ions has also been addressed by Biermanns et al. [92]. Specifically, the correlation between the free surface and the underlying *a/c* interface is studied. Recently, Biermanns et al. [93] have also reported that the formation of defects at such an interface can be tuned by the ion

[1] As we discuss in Section 4, it is customary to term such a region as the "amorphous layer", although "damaged layer" would be more accurate. Note that, in contrast with a non-damaged amorphous substrate, the density of defects in the irradiated layer is strongly dependent on e.g. ion mass and energy.

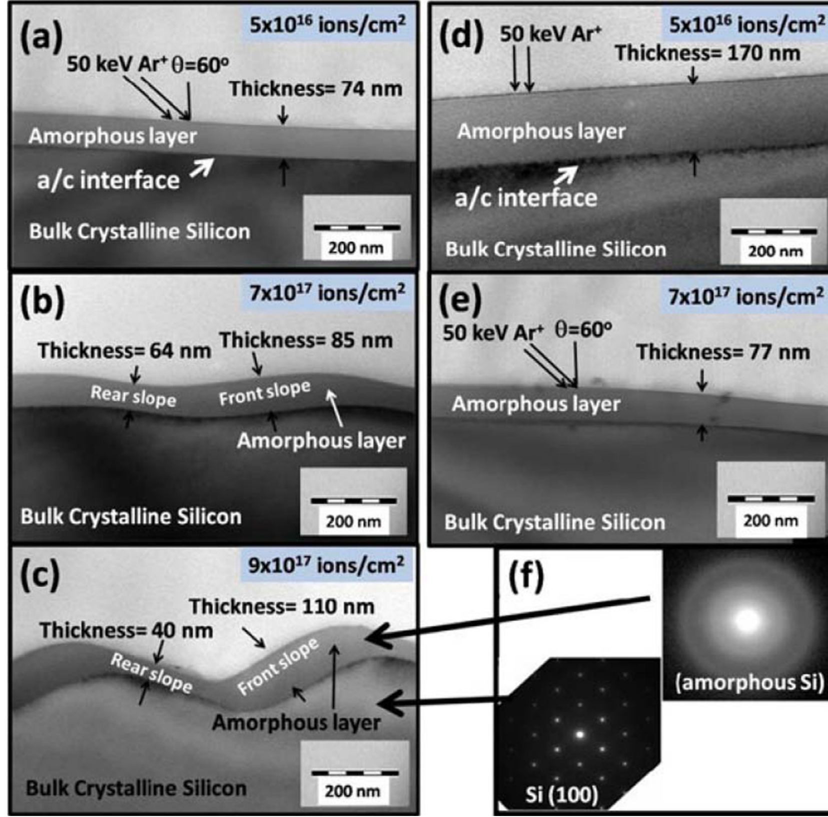

Fig. 13. Ripple formation after pre-amorphization with oblique (a–c) and normal (d and e) incidence 50 keV Ar^+. Clearly, the pattern formation is mitigated in amplitude when the initial target has a thicker amorphous layer (right), as assessed by TEM imaging. These results suggest a relevant role for the amorphous/crystalline interface (f) in the pattern formation. Reprinted from [91] under a Public Open Access License.

incidence angle, and that such defects are important for the pattern formation and dynamics.

In summary, under medium-energy conditions, where the ion penetration range is larger and the amorphized layer is thicker, there seems to be a connection between the *a/c* interface and the surface morphology. This issue will be further considered in Section 5 under the framework of a model in which they both play a role as the boundaries of the amorphous layer, which is considered to flow as a viscous material driven by the ion beam.

Ripple pattern dependence on ion energy. In the previous section, we have already introduced some of the results obtained at different energies. A general observation in these studies is that the ripple amplitude decreases with ion energy, although contradicting dependencies for $\ell(E)$ have been reported. However, it should be noted that different ions were used. Thus, Carter et al. [46] obtained that ℓ was approximately constant for Xe^+ energies in the 10–40 keV range. In contrast, Chini et al. [94] showed a decreasing ℓ with E for Ar^+ irradiation in the 30–60 keV range. Actually this work addressed the behavior of the ripple morphology within the broad 50–140 keV range and $\theta = 60^\circ$ under two configurations, namely, with and without beam scanning. The corresponding data are displayed in Fig. 14. With ion beam scanning, no clear dependence of the ripple amplitude with ion energy was found, while $\ell \sim E^{0.45}$. Remarkably, without beam scanning the wavelength decreased with energy as $\ell \sim E^{-0.56}$. Under this condition the ripple amplitude increased up to 80 keV, where it reached a constant value. The authors argued that these different behaviors should be related with the target temperature during the irradiation, see next item.

Ripple pattern dependence on temperature. In the medium ion energy range, no systematic studies seem available on the dependence of the ripple pattern on the target temperature. The different results reported by Chini et al. [94] with and without ion beam scanning are a clear indication that the temperature of the irradiated surface plays a key role on the pattern properties. Obviously, without beam scanning the surface would be expected to reach higher temperatures than when the ion beam is scanned. Moreover, the early results by Carter et al. [17,86] on the role of the target temperature further indicate the importance of this variable. Here, it was found that reducing the target temperature below room temperature promoted the initiation and evolution of roughening (patterning) at lower fluences.

From our point of view, these partial and, sometimes, conflicting results are demanding new systematic experiments to address the roles played by ion energy, ion mass, beam incidence angle, and target temperature in the medium-energy range. The experience gained during the last recent years in the low energy case, with respect to improved control in the design of the experimental set-ups, can prove to be very useful. In such a way, full comparison with the low-energy experiments could be carried out and, at the same time, the emerging theories could be assessed and validated. Again, we should note that at these energies the stopping processes of the impinging ions by the target atoms are physically different [50], a fact which theories and models should take into account.

3.2. Patterning with simultaneous impurity incorporation

3.2.1. Isotropic patterns: nanodot/nanohole patterns

Nanodot pattern formation. As mentioned in Section 2, the production by Facsko et al. [21] of nanodot structures on GaSb(1 0 0) surfaces via IBS at normal incidence, implied a major

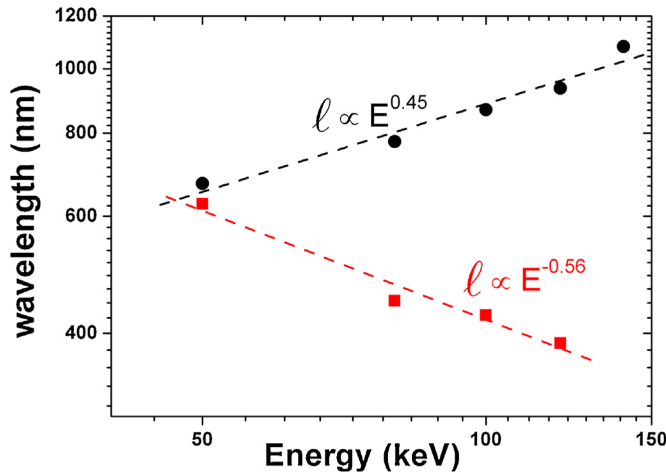

Fig. 14. Dependence of the ripple wavelength on the Ar^{+} ion energy with (black circles) and without (red squares) beam scanning. Adapted with permission from [94]. Copyright 2002, American Physical Society. Note that the original data error bars are not displayed. (For interpretation of the references to colour in this figure legend, the reader is referred to the web version of this article.)

step forward in the field. Shortly after this seminal work, Frost et al. [95] achieved the formation of similar nanodot patterns on InP(1 0 0) surfaces but, in this case, by oblique ion incidence with simultaneous target rotation. Both these first IBS nanodot patterns were thus achieved under isotropic irradiation conditions on bi-elemental semiconductors. However, as has been evidenced recently [96], additional effects like preferential sputtering could come into play with a significant role. In any case, the results in [21,95] triggered the interest to induce similar nanodot patterns by IBS on other systems, including monoelemental silicon surfaces themselves.

The first report on Si nanodot formation by IBS was published in 2001 by some of the present authors, under normal ion incidence with 1.2 keV Ar^{+} [13]. However, problems arose when trying to reproduce these results, as explained in Section 2. For instance, some set-ups only led to flat surfaces upon IBS [97,42]. In other cases, nanodot patterns were indeed produced [98], remarkably even with enhanced medium-range ordering [99]. Also, the possibility to tune this highly-ordered patterns between hexagonal and square arrays was reported [100]. It is worth mentioning that, at some stage of the research, issues on the ion gun characteristics and operation (such as broadness and beam divergence) were considered as rather relevant to explain the already diverse experimental findings [101]. However, as evidenced by Ozaydin et al. [29] and discussed in Section 1 above (recall Fig. 1), most of these findings were induced by metal co-deposition during IBS.

Fig. 15 shows the typical experimental set-up used for nanodot production with metal co-deposition. Note that a metallic mask (typically, from stainless steel) with an inner circular hole is located on top of the target. This piece acts simultaneously as a sample holder and as a source for metal co-deposition. The normal-incidence ion beam irradiates both the uncovered silicon surface and the metallic components in such way that sputtered metal atoms can land on the irradiated silicon surface. Thus, the latter becomes contaminated, containing both Si and metal atoms that are continuously irradiated. This set-up produces isotropic (i.e. nanodot) patterns at the center of the target as a consequence of the system symmetry, since the average flux of incoming metal atoms does not have a preferential direction and ion irradiation is under normal incidence.

The set-up shown in Fig. 15 with a stainless steel mask, as we now know, leads to the production of the nanodot patterns displayed in Fig. 16. Specifically, Fig. 16(a) and (b) show AFM images of silicon surfaces irradiated with 1.2 keV Ar^{+} at normal incidence after 6 min and 960 min of irradiation, respectively. The formation of a nanodot pattern is observed, which displays short-range in-plane hexagonal order, as the corresponding height two-dimensional autocorrelation functions show, see insets. The nanostructures have a height of 5–6 nm and a diameter between 40 and 50 nm. The inset of Fig. 16(b) shows the improved definition of the hexagonal arrangement in the correlation functions, which reveals the enhancement of in-plane order with sputtering time. RBS analysis of these nanodot patterns reveals the effective incorporation of Fe (and Cr) from the mask. Here, the residual (and stationary) amount of Fe is approximately 2×10^{15} atoms/cm^2, which is attained just after the first few minutes of irradiation.

Interestingly, in a recent work [102] the symmetry of nanodot patterns has been controlled by means of an experimental configuration which differs from the one depicted in Fig. 15. In this case, the set-up exploits the role of the impurity flux towards the sample in order to yield Fe-assisted patterns with a variety of designed symmetries and wavelengths. This is achieved by normal ion incidence and adjusting the size, distance, and arrangement of different metal pieces surrounding the silicon sample, see Fig. 17. This result highlights the potential of IBS nanopatterning under impurity co-deposition as a versatile nanofabrication tool.

The crystalline nature of the nanostructures induced on single-crystal semiconductors like Si(1 0 0) is a relevant issue for potential applications of IBS patterns in semiconductor and

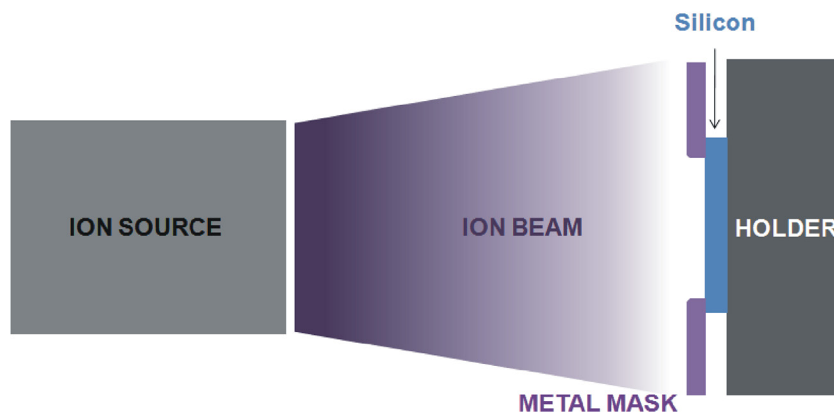

Fig. 15. IBS set-up for nanodot pattern formation by normal-incidence with concurrent metal co-deposition. A metal plate with an inner circular hole fixes the target to the holder and simultaneously acts as a mask. The uncovered parts of the target are co-deposited with metal atoms during irradiation.

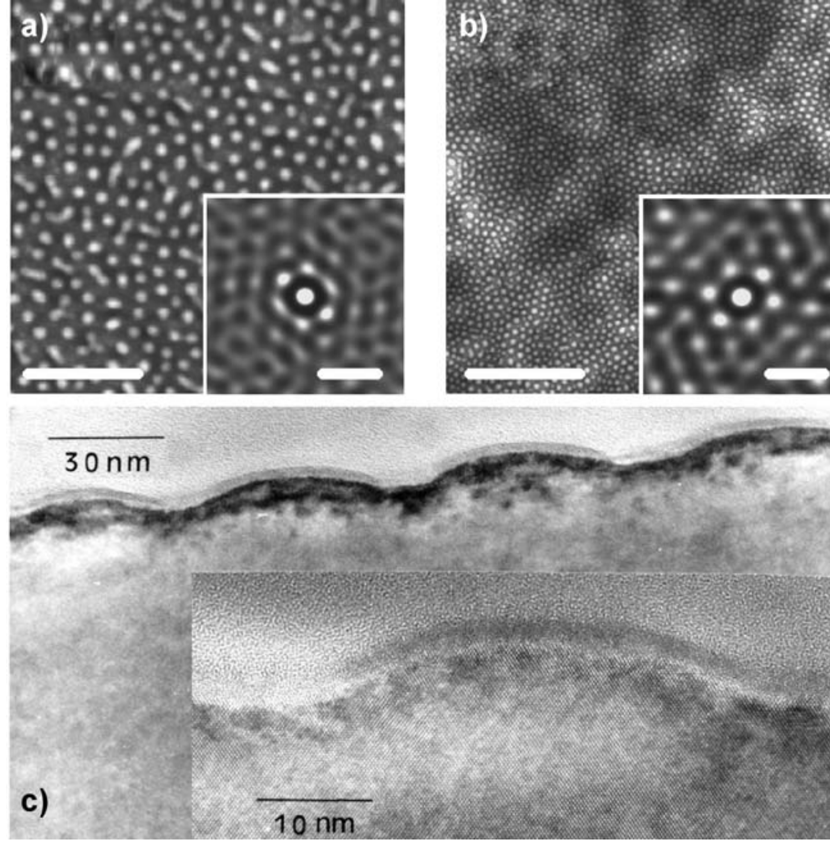

Fig. 16. AFM images of Si(1 0 0) surfaces irradiated with 1.2 keV Ar^+ at a current density of 0.24 mA/cm^2 for (a) 6 min and (b) 960 min. The insets show the corresponding autocorrelation functions revealing the short-range hexagonal order of the pattern. The bars represent 277 nm (a), 831 nm (b), and 111 nm (insets). (c) Cross-sectional TEM image of a Si(1 0 0) surface sputtered for 10 min. The inset is a high-resolution image showing the crystalline nature of the nanodot core. Reprinted with permission from [13]. Copyright 2001, AIP Publishing LLC.

optoelectronic applications, e.g. for the fabrication of quantum dots. A cross-sectional transmission electron microscopy (TEM) image along the $\langle 1\,1\,0\rangle$ direction of a Si(1 0 0) target sputtered for 10 min is shown in Fig. 16(c). The formation of crystalline nanostructures with lenticular shape covered by an amorphous layer roughly 2 nm thick is clearly observed. The height and width of the nanocrystals are in agreement with those obtained by AFM, once tip convolution effects are taken into account. The inset shows a high-resolution TEM (HRTEM) image of one of these nanostructures. In this case, $\{1\,1\,1\}$ lattice fringes are visible, revealing the crystallinity of the nanostructures and a low number of defects within the nanostructure core. Therefore IBS, albeit with metal co-deposition, is capable of producing crystalline nanostructures on silicon surfaces.

Nanodot patterning dynamics. In order to get further insight into the patterning mechanisms, it is mandatory to study the nanopatterning dynamics by quantifying the morphological features as a function of the irradiation time. An example of such study, as extracted from [103], is displayed in Fig. 18. Here, the height power spectral density (PSD) function is employed to assess the pattern characteristics from the AFM images. The PSD is defined as

$$S(k,t) = \langle h(\mathbf{k},t)h(-\mathbf{k},t)\rangle, \quad (2)$$

where $h(\mathbf{k},t)$ denotes the Fourier transform of the surface height profile, $h(\mathbf{r},t) - \bar{h}$. Here, $\bar{h}$ stands for the average height of this profile and $\mathbf{k}$ is wave vector of magnitude $k = |\mathbf{k}|$. The basic pattern wavelength (ℓ) is related to the emergence of a finite peak at $k = k_{max}$ in the *PSD* curve where $\ell = 2\pi/k_{max}$. Fig. 18(a) shows the PSD curves obtained from Si(1 0 0) surfaces irradiated with 1 keV Ar^+ for different times [103].

Clearly, the peak in the PSD curves shifts towards small k values as the irradiation proceeds, indicating an increase in ℓ with time (coarsening). Additionally, the increase of the intensity of the PSD with time at low k values reflects long-range roughening of the surface, as observed in Fig. 16(b). Moreover, the fact that the peak becomes narrower with increasing time, Fig. 18(a), indicates that the domain size of ordered structures increases [104], in agreement with the improvement of the order in the autocorrelation functions displayed in the insets of Fig. 16(a) and (b).

Figs. 18(b) and (c) show a quantitative analysis of the surface morphology after IBS for different ion fluxes. Initially, the global surface roughness, W, increases sharply, while a slower growth regime is observed at longer times [Fig. 18(b)]. Likewise, the initial coarsening [Fig. 18(c)] is *interrupted* for longer irradiation times, at which both W and ℓ reach stationary values. Fig. 18(b) and (c) also show that pattern formation occurs earlier for a higher ion flux. However, when the same data are represented as a function of the ion fluence [insets of Fig. 18(b) and (c)], they collapse into a single curve, which indicates that the final pattern characteristics are defined by the total number of ions that impinge onto the surface. In this case, the metal content derived from RBS measurements lies within the same range ($1–2 \times 10^{15}$ $atoms/cm^2$) for all the samples. Therefore, the pattern dynamics which is observed does not originate in a variation of the metal content during the experiment.

The solid lines in Fig. 18(b) and (c) refer to the simulations from a two-field continuum model [103], see Section 5. As evidenced, the simulations reproduce nicely nanodot pattern formation on silicon with metal co-deposition. Although further details will be given later, the successful description of such an *interrupted*

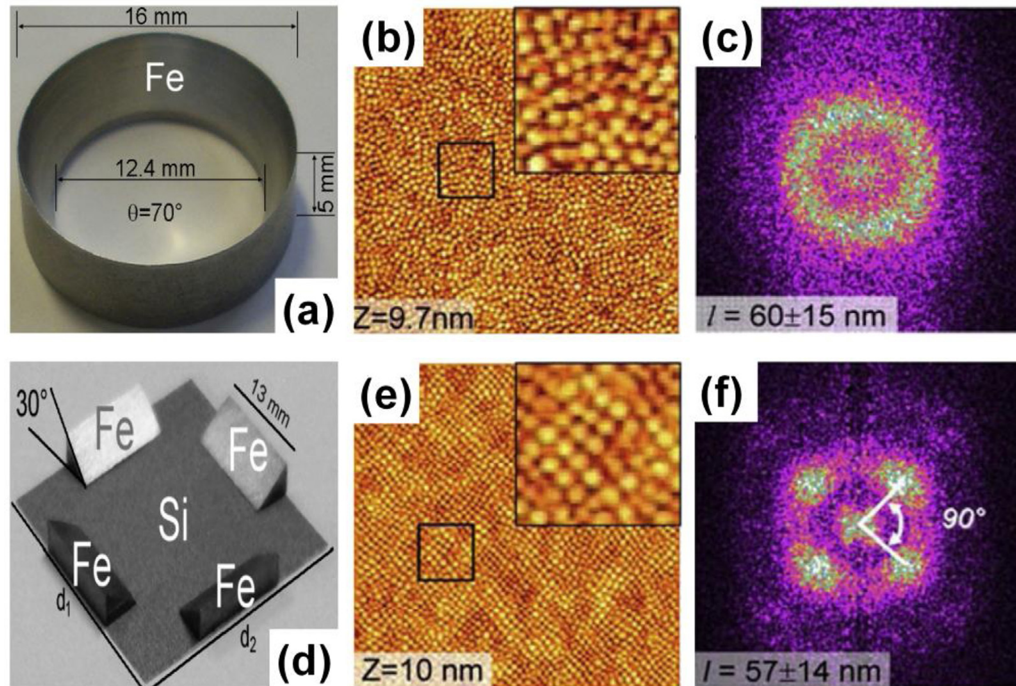

Fig. 17. Changes in the symmetry of nanodot patterns by adjusting the arrangement of metal co-deposition targets under normal incidence 1 keV Ar^+ IBS. The use of a cylindrical Fe piece (a) results into a dense nanodot pattern (b) that shows no preferential in-plane orientation in the fast-Fourier transform (FFT) analysis (c). On the contrary, the use of four Fe targets forming a square (or a rectangle) (d) induces the formation of an ordered nanodot pattern (e) with a clear 4-fold symmetry in the FFT image (f). The residual Fe content is 1.6 and 1.8×10^{15} ions/cm^2 for the patterns shown in (b) and (e), respectively. Adapted from [102] under a Public Open Access License.

coarsening behavior is of great relevance in the general context of pattern formation far from equilibrium. In our present case, *interrupted coarsening* is interesting because it allows to produce nanodots of reduced dimensions.

A quantitative analysis which is similar to that shown in Fig. 18 was carried out by changing the nature of the starting condition [105]. Specifically, the question addressed in this reference was the influence of the crystallinity of the initial surface on the evolution of the pattern. This issue has attracted the interest of many researchers in the field, ever since the earliest reports on nanodot formation on GaSb [106]. For the case of Si [105], both amorphous Si (*a*-Si) films and crystalline Si(1 0 0) (*c*-Si) targets were irradiated simultaneously with 1 keV Ar^+ ions at normal incidence. The simultaneous irradiation of both targets, together with the rotation (10 rpm) of the sample holder during the process, ensured equal irradiation conditions. The erosion time was limited to 45 min to avoid reaching the film/substrate interface in the case of *a*-Si films. Fig. 19 shows the AFM surface topographies before and after irradiation. The AFM images already suggest that the pattern characteristics and dynamics induced on both targets are rather

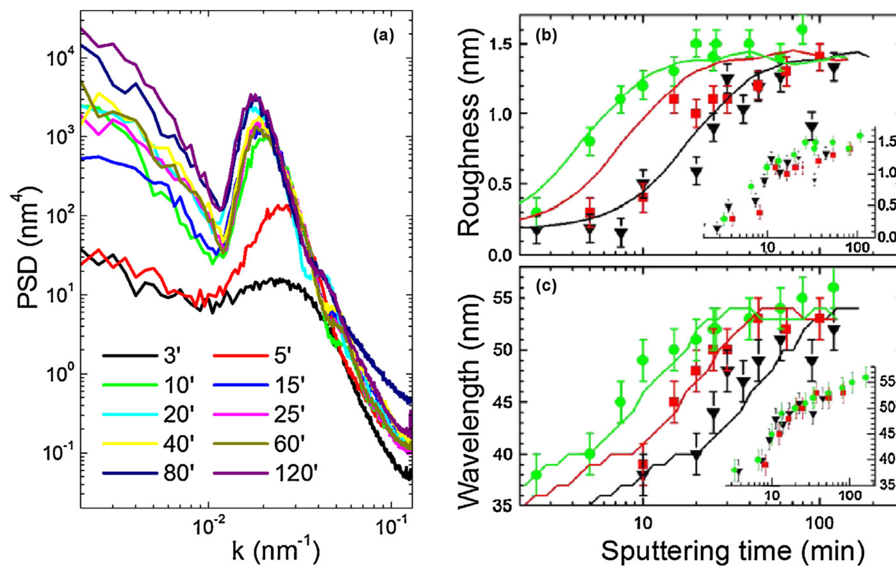

Fig. 18. (a) *PSD* curves derived from AFM images of Si(1 0 0) after IBS with 1 keV Ar^+, for different times at a current density of 0.36 mA/cm^2. Time evolution of the (b) roughness, *W*, and the (c) pattern wavelength, ℓ, for different ion current density values: 100 μA/cm^2 (black triangles), 230 μA/cm^2 (red squares,) and 420 μA/cm^2 (green circles). The solid lines represent the corresponding results from numerical simulations (see Section 5.2.1). The insets in (b) and (c) show the same experimental data plotted as a function of the ion fluence (units of the horizontal axis are 10^{17} ions/cm^2). Reprinted with permission from [103]. Copyright 2010, American Physical Society. (For interpretation of the references to colour in this figure legend, the reader is referred to the web version of this article.)

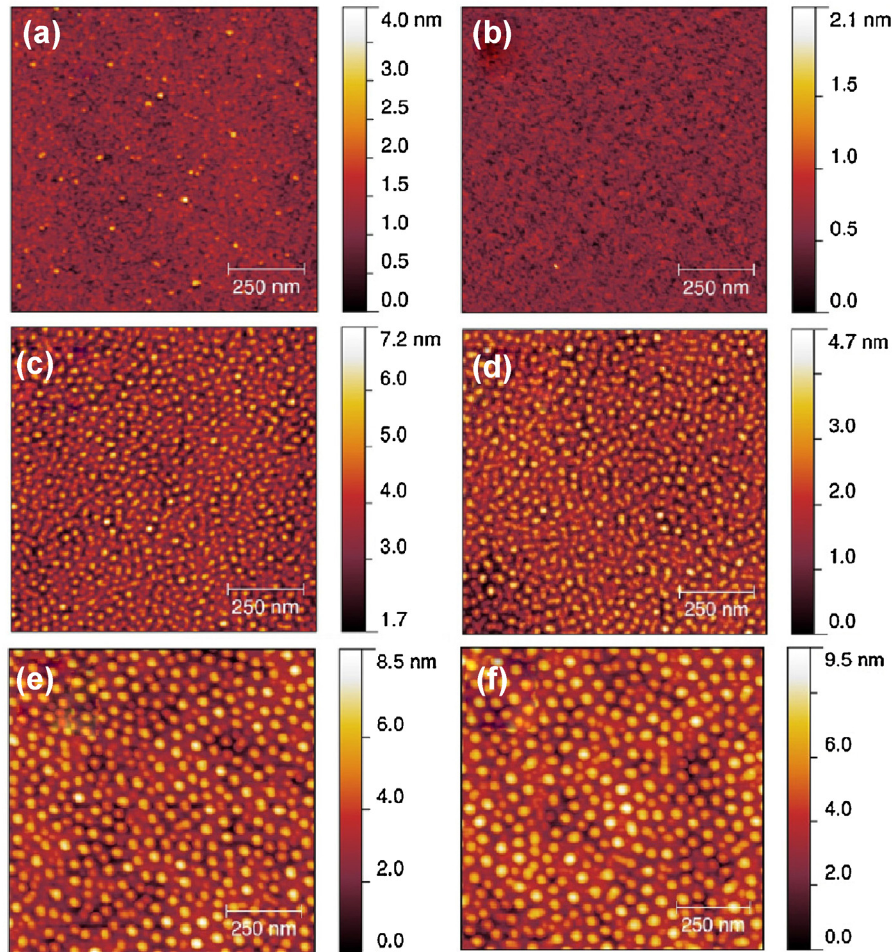

Fig. 19. 1 μm × 1 μm AFM images showing the evolution of initially flat amorphous Si (left column) and crystalline Si (right column) targets before [(a) and (b)] and after IBS with 1 keV Ar^+ ions during 7.5 min [(c) and (d)] and 45 min [(e) and (f)]. White scale bars represent 250 nm. Reprinted with permission from [105]. Copyright 2012, IOP Publishing.

similar, already from the initial stages of the nanodot pattern [Fig. 19(c) and (d)], and also during the later ones [Fig. 19(e) and (f)]. The morphologies produced look similar, both displaying pattern coarsening, and roughening at large scales and long times. These observations were quantitatively confirmed when the dynamics were analyzed similarly to Fig. 18 (not shown). The negligible influence on the dynamics of pre-existing amorphous material can also be explained by the fact that crystalline Si becomes amorphous for small ion fluences of 10^{14}–10^{15} ions/cm^2 [12], which implies irradiation for just a few seconds under our present working conditions. That is, the formation of the amorphous layer during IBS occurs in a time scale that is much faster than the temporal scale needed to induce a pattern on the surface. However we should note that, in a previous study performed with a similar set-up, but without target rotation [107], pattern formation was observed to depend weakly on the crystallographic surface orientation. Specifically, Si(1 1 1) surfaces showed an enhancement of pattern order with respect to that found for Si(1 0 0) irradiated under the same conditions.

Ordered dot patterns like the one shown in Fig. 20(a) have been achieved by Ziberi et al. [99]. Naturally, the high quality of the arrangements is reflected both in the AFM image and in its Fourier spectrum, Fig. 20(b), where well-defined rings are observed up to the third order. The high order is also evidenced by the radially averaged PSD shown in Fig. 20(c). Here, the small width of the main peak and the appearance of secondary peaks are indications of the relatively large sizes of ordered dot domains [104]. The experimental set-up by Ziberi et al. [99] for nanodot production differs from that depicted in Fig. 15. They employed $\theta = 75°$ and target rotation at a rate close to 12 rpm [108] during Ar^+ irradiation. In this case, target rotation induces the pattern isotropy. In principle, this configuration could result into nanodot pattern formation by itself [109]. But, as shown in the case of ripple patterns produced with the same set-up [108] (see Section 3.2.2), metal incorporation cannot be disregarded because the beam employed was quite broad (∼20 cm), likely inducing simultaneous bombardment of the chamber walls. Moreover, in a recent work Chowdury et al. [54] have reported the production of nanodot patterns with a similar experimental set-up, but under impurity-free conditions as assessed by EDX. They find quite a different pattern, composed by well-packed dot structures [Fig. 20(d)] whose size decreases as the rotation rate increases from 0.2 rpm up to 25 rpm. Although the corresponding autocorrelation function does show short-range hexagonal ordering [Fig. 20(e)], already visual comparison of both patterns can detect clear differences. This allows to conclude that metal co-deposition quite probably plays a relevant role in the production of highly-ordered patterns.

Nanohole pattern formation. Among the isotropic nanopatterns produced with simultaneous metal co-deposition, it is interesting to highlight those featuring nanohole structures. This kind of pattern has been scarcely found and reported. In particular, they were reported [34] after IBS with an alternating cold-cathode ion source (ACC-IS) (instead of the more conventional Kaufman ones),

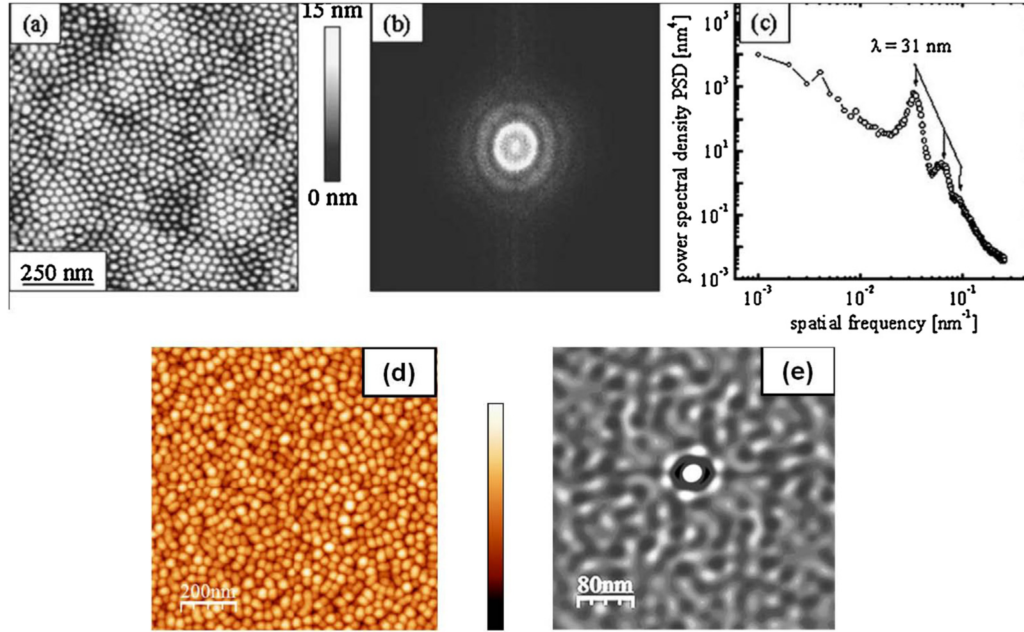

Fig. 20. (a) 1 μm × 1 μm AFM image of self-organized Si nanodots produced on Si(1 0 0) by 500 eV Ar^+, ion flux of 200 μA/cm^2 under 75° irradiation with simultaneous target rotation during 180 min. (b) Fourier spectrum of the AFM image showing high order peaks. (c) PSD function calculated from the AFM image, showing a mean dot separation/size of 31 nm and an average domain size of 165 nm, respectively. Reprinted with permission from [99]. Copyright 2005, AIP Publishing LLC. (d) AFM image of surface pattern produced with a similar set-up with an Ar^+ flux of 1100 μA/cm^2 and fluence of 4.75×10^{18} ions/cm^2 but with simultaneous target rotation at 12 rpm and under impurity-free conditions. (e) Corresponding autocorrelation function. Reprinted with permission from [54]. Copyright 2014, Elsevier.

using a similar set-up to that indicated in Fig. 15. Thus, Fe atoms are co-deposited due to the ion gun operation (since Fe is produced by the plasma erosion of the cathodes) and Mo atoms are incorporated onto the silicon surface from the fixing clamps. In this way, it was possible to produce both flat and smooth surfaces [Fig. 21(a)], as well as nanohole [Fig. 21(b)] and nanodot [Fig. 21(c)] patterns. Occasionally, a hole-dot mixed pattern was also obtained [Fig. 21(d)].

The different pattern types shown in Fig. 21(a)–(d) reflect in the corresponding height distributions [Fig. 21(e)]. This allowed to label each surface morphology through the quantification of the corresponding surface skewness, χ_1, which is defined as [110]

$$\chi_1 = \frac{\langle (h(\mathbf{r}) - \bar{h})^3 \rangle}{W^3}. \quad (3)$$

In particular, nanodot and nanohole patterns are associated with $\chi_1 > 0.2$ and $\chi_1 < -0.2$, respectively. The nanodot patterns displayed in Fig. 21(c) are rather similar to those produced with a Kaufman-type ion gun (see Fig. 16).

Nanohole and nanodot patterns share common features, as derived from the corresponding autocorrelation functions [insets of Fig. 21(b) and (c)] and PSD functions [Fig. 21(f)]. The former show similar short-range hexagonal ordering, whereas the PSDs almost overlap. Hence, both dense nanohole and nanodot patterns can be quite alike in terms of homogeneity, surface roughness, wavelength, and short-range order. Less ordered nanohole patterns have also been reported in the last years. In one case, hole nanostructures were also found in impurity-free experiments [41]. They wer explained as originating in multiple scattering events from the impingement of the primary ion beam on adjacent silicon shields [41]. In addition, nanoholes have also been found in experiments with metal co-deposition. However, in this case the metal incoming flux was rather directional and the holes were only found in the vicinity of the metal clamp [33]. In contrast, in our set-up the nanoholes were found at the center of the target where the metal flux was isotropic.

Another interesting feature of these nanohole/nanodot morphologies is the correlation between the residual metal content and the type of pattern. Fig. 22 shows the quantitative

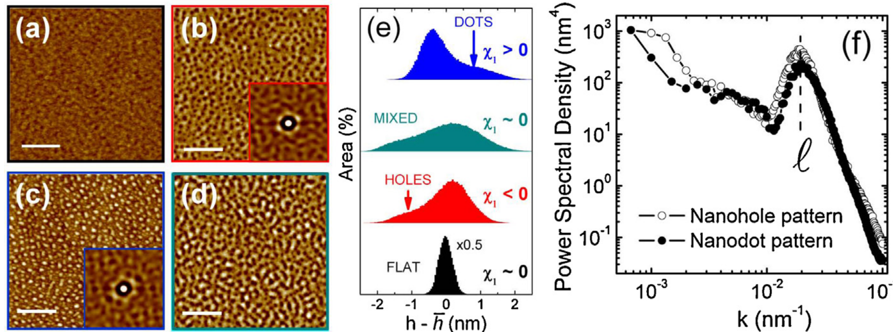

Fig. 21. Surface morphologies obtained after 1 keV Ar^+ erosion under normal incidence with an ACC-IS ion gun: (a) flat, (b) nanohole pattern, (c) nanodot pattern, and (d) mixed (nanohole/nanodot) pattern. (e) Height distribution and the corresponding surface skewness, χ_1, used as a parameter to classify the different patterns. (f) PSD functions of nanodot and nanohole patterns showing their similar features. Adapted with permission from [34]. Copyright 2008, IOP Publishing.

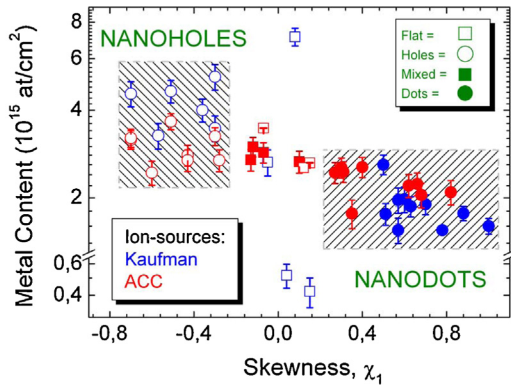

Fig. 22. Residual total metal content obtained from RBS measurements after 1 keV Ar^+ IBS under normal incidence with Kaufman (blue symbols) and ACC-IS (red symbols) ion guns, as a function of the surface morphology skewness. Reprinted with permission from [111]. Copyright 2009, IOP Publishing. (For interpretation of the references to colour in this figure legend, the reader is referred to the web version of this article.)

analysis, as derived from the RBS data as a function of the morphological pattern properties, i.e. skewness. No clear trend has been found with respect to the metal ratio when several impurities are employed. The total metal content in IBS targets roughly falls within the range from 10^{14} to 10^{16} atoms/cm^2. In agreement with other reports [32,33,36], 10^{15} atoms/cm^2 seems to be a rough estimate of the threshold for pattern formation, see shadowed areas in Fig. 22. Clearly, the metal content in Fig. 22 decreases with χ_1, indicating that more impurities should be incorporated onto the surface in order to induce a nanodot to nanohole transition. In addition, note that too many impurities would result into a flat morphology. XPS and AES spectroscopies were employed to further characterize the metal incorporation to the pattern surface. Thus, XPS analysis proved that the oxidation was restricted to the near surface regions and, hence, originated in air exposure after preparation. Also, XPS and AES analysis yield a metal content at the near-surface region between 5% and 10%. This range is in agreement with the RBS data and, noticeably, with the AES data reported by Ozaydin et al. [29]. This means that metals are not constrained to the surface and are mostly distributed within the 4–6 nm amorphous layer. Finally, high resolution XPS studies revealed that both metals, Mo and Fe, were forming silicides.

3.2.2. Anisotropic patterns: nanoripples

In the previous section, we have described how isotropic patterns mainly arise when the ion beam impinges close to normal incidence, concurrent with an isotropic metal flux. In principle, as we have discussed in Section 3.1, anisotropic (i.e. ripple) patterns can be obtained without metal co-deposition when θ is larger than a threshold value (around 45–50° for low-energy Ar^+ irradiation). However, ripple patterns were also obtained earlier for θ values smaller than this threshold, likely due to the unintentional incorporation of metal impurities during the ion irradiation. It should be noted that, in addition, metal co-deposition can be used to tune or modify the ripple patterns produced for $\theta > \theta_c$. Thus, in this section we will describe ripple patterns, some of them displaying long-range ordering and perfection, where the metal supply was apparently not controlled. We also describe more recent experiments in which the metal incorporation process was systematically addressed.

Low-energy ripples. The group of Frost et al. has been deeply involved in the past in the production of ripple patterns on silicon (see for example [112]), probably in most cases under metal co-deposition as evidenced later. In a review published in 2009 [108], they highlight the most ordered morphologies from an ensemble of 3000 samples obtained in a period of four years. Here, we will focus on some remarkable examples of ordered ripple patterns, such as those displayed in Fig. 23, obtained for different ions and irradiation conditions.

The ripple morphologies shown in Fig. 23 were obtained under ion incidence angles of 15° and 20°, well below the threshold angle recently reported for ripple production under impurity-free conditions. Therefore, as it is now understood, these patterns should be related to the influence of metal co-deposition. In all

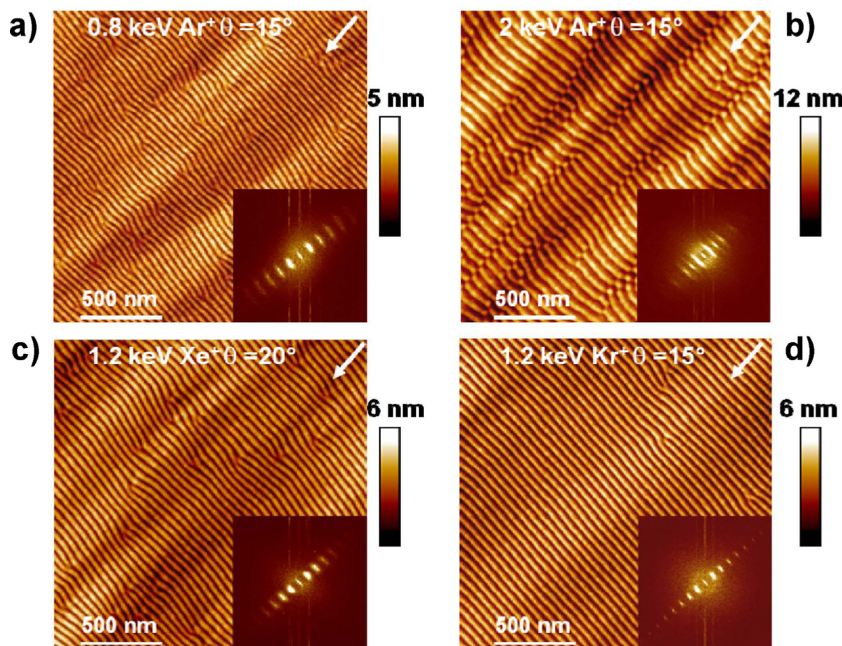

Fig. 23. AFM images of self-organized ripple patterns on Si surfaces after 800 eV (a) and 1200 eV (b) Ar^+ ion beam erosion at $\theta = 15°$; 1200 eV Xe^+ ion beam erosion at $\theta = 20°$ (c); 1200 eV Kr^+ ion beam erosion at $\theta = 15°$ (d). The corresponding Fourier transforms are included as insets. The white arrows indicate the direction of the incoming ion beam. Adapted with permission from [108]. Copyright 2009, IOP Publishing.

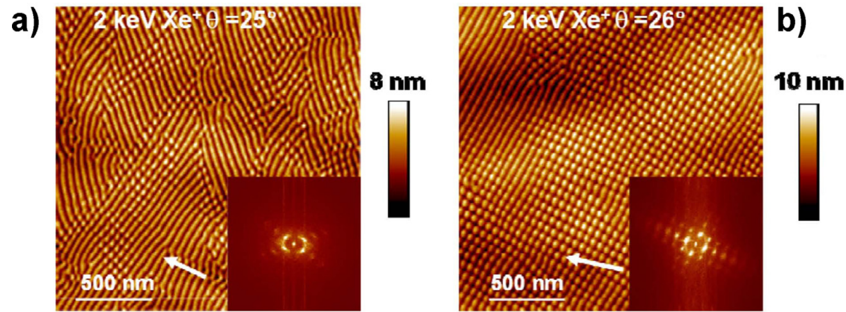

Fig. 24. AFM images of self-organized ripple patterns on Si surfaces after 2000 eV Xe^+ ion beam erosion at (a) $\theta = 25°$, where ripples with different orientations coexist with dot structures; and (b) $\theta = 26°$ for which an almost perfect square array of dots is observed. The corresponding Fourier transform images are included as insets. The white arrows indicate the direction of the incoming ion beam. Reprinted with permission from [108]. Copyright 2009, IOP Publishing.

cases, the corresponding fast-Fourier transform (FFT) images are shown as insets. The enhanced order of the patterns is evident from the multiple spots in the spatial-frequency spectra. Also, it is interesting to note the dependence of the ripple wavelength on the ion energy [Fig. 23(a) and (b)]. The high degree of order obtained for the case of Kr^+ irradiation, for which long, parallel, straight ripples are produced, is quite remarkable. Finally, a sort of mixed pattern morphologies were also reported for incidence angles for which no patterns appear when there are no impurities. Fig. 24(a) and (b) show two examples. In Fig. 24(a) ripple morphologies with different orientations coexist together with some small nanodot domains with square order. This dot morphology becomes dominant for slightly different irradiation conditions, as shown in Fig. 24(b).

The experimental set-up in [108] produced a great variety of morphologies. In some cases, very slight changes in the experimental parameters already led to different shapes, as shown in Fig. 24. It is worth noting the interest of these results. In particular, it is evident that the (in this case, inadvertent) incorporation of impurities during the irradiation can lead to more perfect patterns, different geometries, and enhanced ordering at the nanoscale. Thus, knowledge and control of the mechanisms involved in the process and in the impurity incorporation pathways, could eventually lead to the achievement of improved IBS nanopatterns. The continuation of the prolific work in [108], but now addressing metal co-deposition explicitly, was provided in [113,114]. The same system was considered, but now composition-controlled experiments were performed by placing a stainless steel hollow liner in the path of the ion beam from the source towards the sample. In this way, the putative metal sputtering from the chamber walls, particularly when using highly divergent ion beams, was mimicked and promoted. Additionally, it was possible to tune the incorporation of Fe onto the irradiated surface by changing the liner position and geometry, and/or the ion beam configuration. Ripples were produced with 2 keV Kr^+ ions at different incidence angles, also observing that a certain steady state of metal coverage (in the range of 10^{15} atoms/cm^2) is needed for the pattern formation. In a recent study of those samples, the formation of silicides at the surface was determined by XANES. The dominant contribution of $FeSi_2$ was evidenced, which is affected by a variable fraction of Fe-rich silicide (Fe_3Si). X-ray reflectivity (XRR) was also employed to determine the variations in the Fe depth profile, finding larger in-depth metal distribution in patterned samples [115].

Recent efforts have focused on the systematic incorporation of impurities during IBS, with the goal of exploring the morphologies and unveiling the underlying physical mechanisms. In this context, in 2008 Hofsäss et al. coined the term "*surfactant sputtering*" [116]. It refers to the steady-state coverage of a target (e.g. silicon) surface with up to 10^{16} atoms/cm^2 of foreign or self atoms, by combined ion irradiation and atom deposition. These surfactant atoms strongly modify the substrate sputtering yield from atomic to macroscopic length scales. Thus, depending on the surfactant/substrate combination, this technique allows enhanced smoothing of surfaces, or the generation of novel surface patterns and nanostructures. A scheme with a typical example of the experimental set-up used for *surfactant sputtering* is displayed in the left panel of Fig. 25. In this case, the Si(1 0 0) substrate can be irradiated under normal or oblique incidence. Simultaneously, the foreign (i.e. impurity) atoms come from an adjacent plate (named target in Fig. 25) located at the extreme of the substrate with a given tilt. This plate becomes co-sputtered by the incoming ion beam so that, during irradiation, the foreign atoms deposit on the silicon surface. Sputter yield modifications and chemical reactions with the Si substrate are identified as relevant issues to define the final pattern characteristics. For example, Fig. 25 shows how the surface morphology of Si(1 0 0) substrates can be modified with the amount of self (Si) (top row) or foreign (Au) (bottom row) impurities. Different *surface coverage* of *surfactants* is attained with distance *d* from the target: according to the notation in Fig. 25, in this case the coverage increases with *d*.

Similar experimental set-ups have been employed to carry out a series of systematic studies aiming to understand the role of metal incorporation in IBS [64,33,32]. These works focused on Fe co-deposition, as many components in the standard ion beam equipments contain stainless steel. Thus, a plate of the latter material is attached close to the sample at a certain angle, acting as a metal source. Macko et al. [64] proposed this set-up attaching a metal plate normal to the sample surface, as shown in Fig. 26(a), while Zhang et al. [32] considered a more versatile configuration in which the angle of the plate can be changed. In both cases, the metal flux (Φ_{metal}) towards the silicon surface is proportional to the primary ion beam flux (Φ_{beam}). Moreover, as shown in Fig. 26(a), the incoming metal flux at a given location on the silicon surface depends on its distance to the metal plate. Therefore, the analysis of the pattern morphology and metal content as functions of this distance will be one of the main foci of these studies. With this experimental set-up, the beam current controls not only the erosion rate of the sample but also the metal deposition rate on it. Under these conditions, the surface coverage changes continuously with ion fluence. Due to the balance between the erosion and the deposition processes, a steady-state value is expected at long enough times [33]. With this set-up, the direction, energy, and flux of the sputtered metallic species are relatively broad. Moreover, the reflected primary beam also influences the plate, preferentially impinging at surface regions closer to the latter. As represented in Fig. 26(a), this indirect beam causes an additional local ion erosion that induces an inhomogeneous surface profile (at macroscopic scales) and metal distribution. The metal content is maximum close to the position of the plate and decreases with distance

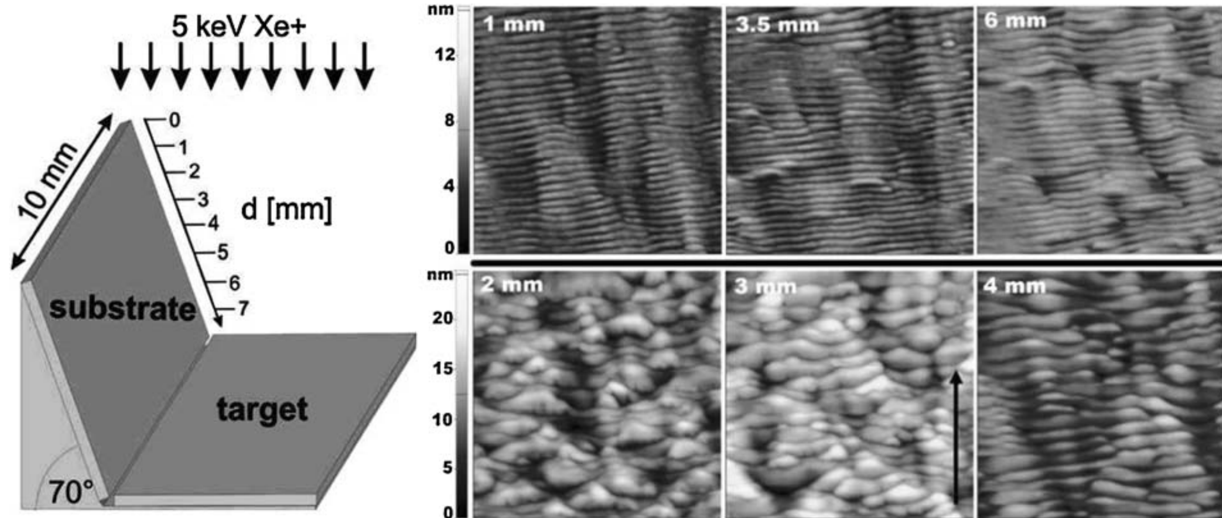

Fig. 25. *Left*: Set-up for "*surfactant sputtering*". Surfactants are ejected onto the Si(1 0 0) substrate by the simultaneous irradiation of a target of the surfactant species. *Right*: Changes in the morphology of Si(1 0 0) surfaces with the distance (surfactant coverage) along the substrate for Si (top row) and Au (bottom row) surfactants (targets). Adapted from [116] under a Public Open Access License.

beyond this location. Due to the existence of a most probable emission angle for the sputtered metal, there is also a pronounced directional effect of the metal deposition on the silicon surface at a certain distance to the plate. However, this effect becomes negligible at larger distances. In the experiments of [64,33,32], the ion incidence angle with the substrate surface, θ, was chosen under conditions for which flat surfaces were obtained in absence of simultaneous metal supply.

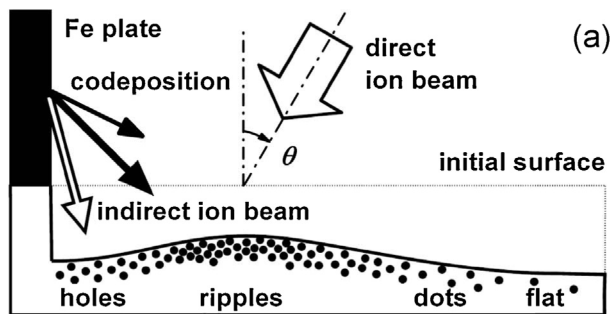

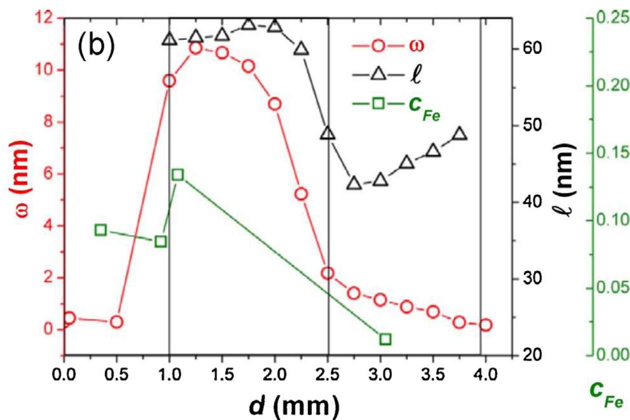

Fig. 26. (a) Experimental set-up for IBS nanopatterning with metal co-deposition (adapted from [64]). The change in the surface profile, composition, and morphology is due to the interplay between direct erosion, Fe co-deposition and indirect erosion. In this case, at the θ value employed, IBS should not produce any patterning on the silicon surface without metal co-deposition. (b) Surface roughness (ω), pattern wavelength (ℓ), and Fe concentration (c_{Fe}) as a function of the distance, d, from the Fe plate. Reprinted with permission from [64]. Copyright 2010, IOP Publishing.

With the set-up shown in Fig. 26(a), Macko et al. [64] studied the surface patterns induced on the silicon surface by the irradiation with 2 keV Kr^+ at $\theta = 30^\circ$ as a function of the distance, d, from the metal plate. As shown schematically in Fig. 26(a), they established: *(i)* the absence of well-ordered patterns close to the metal plate, due to the secondary erosion process (disordered nanohole-like structures were observed); *(ii)* the existence of ripples in metal-rich regions at intermediate distances, their wavevector being parallel to the direction of the co-deposited metal; *(iii)* the formation of dots at larger distances where the metal concentration and the directional effects are small; and *(iv)* the existence of flat regions far away from the metal plate. The corresponding morphological features and the metal ratio on the surface are shown in Fig. 26(b). Initially, these observations were qualitatively explained on the basis of the interplay between the erosion and deposition processes, taking into account the sputtering rates and the directionality of the ions reflected from the metal plate. However, the mechanisms through which the incoming metal atoms had such a large influence on the patterning processes remained unknown.

Zhang et al. [32] used a slightly different set-up in which the 5 keV Xe^+ ion beam was kept normal to the Si substrate, but the angle of the metal plate with respect to the silicon surface could change between 20° and 60°. They found, in agreement with Macko et al. [64], that ripples only form for high steady-state metal contents (in the $5 \times 10^{15}–10^{16}$ Fe atoms/cm^2 range), whereas dots appear for low steady-state metal concentrations ($2 \times 10^{15}–4 \times 10^{15}$ Fe atoms/cm^2). Moreover, they studied the dynamics of the pattern at a fixed target location and steady-state metal content, as shown in Fig. 27. A progressive transition from dot to ripple patterns with ion fluence can be observed for the highest metal content (top row). This transition is not observed for the lower steady-state metal coverage (bottom row), likely due to the narrow temporal window. The ripple length (pattern defect density) increases (decreases) with ion fluence and develops some degree of curvature. The latter has been related to the angular distribution of the metal flux [32]. In fact, in the case of metal co-deposition the ripple orientation is not defined by the ion beam incidence (see Section 3.1) but rather by the metal flux since ripples appear with wavevector parallel to the projection of the latter on the surface [64]. It is interesting to note that the nanodot patterns shown in Fig. 27 form even with a rather directional flux (i.e. from left to right) of co-deposited metal atoms, as reported

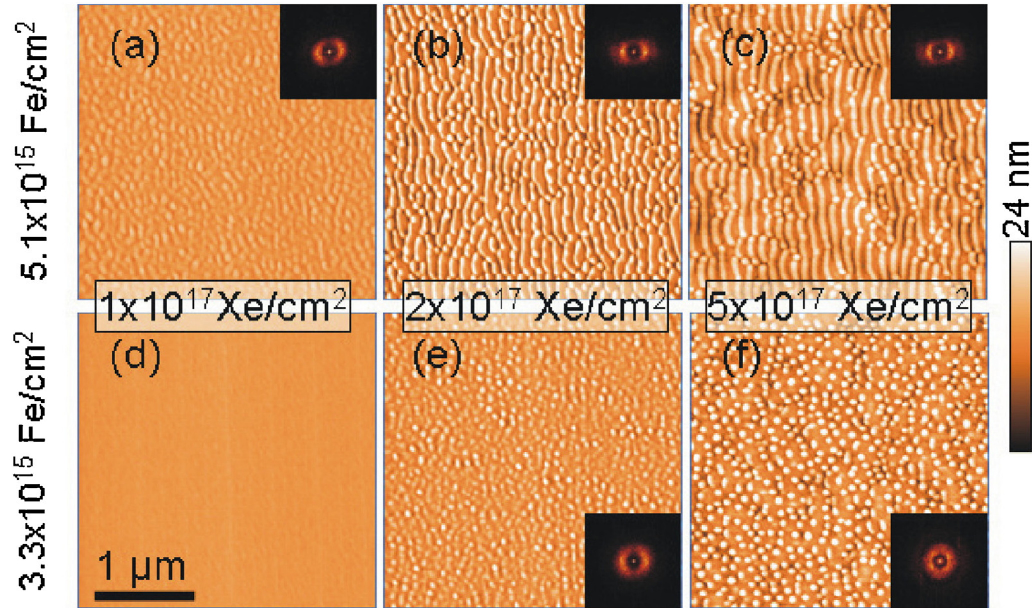

Fig. 27. 3 µm × 3 µm AFM images of samples irradiated with 5 keV Xe^+ ions and Fe co-deposition with Fe steady-state coverage of 5×10^{15} atoms/cm^2 (a–c) and 3×10^{15} atoms/cm^2 (d–f) for Xe^+ ion fluence increasing from 1×10^{17} to 5×10^{17} ions/cm^2. The projected Fe-deposition direction is from left to right. The corresponding FFT transforms are shown in the insets. Reprinted from [32] under a Public Open Access License.

previously by Macko et al. [64]. Also, there is a threshold value of metal content ($\sim 2 \times 10^{15}$ Fe atoms/cm^2) below which only flat surfaces are produced. Detailed TEM and EDX analysis did show that the Fe atoms formed silicide (Fe_xSi) aggregates on the ripple structures. Recently, Hofsäss et al. [74] have studied the propagation of the ripples induced under Fe incorporation in their set-up. They have found that, in contrast to the case of the metal-free case, the ripples propagate always in the same direction, which is towards the Fe clamp.

In a work which is contemporary to that in [32], Macko et al. [33] carried out a series of systematic experiments based on the previous set-up described in Fig. 26(a). In this case, the silicon surface was irradiated with 2 keV Kr^+ ions at $\theta = 30°$, for which no pattern should be induced under metal-free conditions. The authors studied again the dependence of the induced pattern morphology with the increasing (decreasing) distance to the metal plate (metal content). Basically, they confirmed the dependence observed in their previous report [64], as the irradiated surface showed a sequence of holes-ripples-dots-flat morphologies with increasing distance. This sequence was observed to be practically unchanged in the 140–440 K range. In addition, TEM and EELS analysis allowed to verify that the co-deposited material had its highest concentration on the ripple facet facing the incoming metal flux. Recently, Macko et al. [117] have extended their research to higher temperatures (660 K), for which the Si surface remains crystalline, with the same experimental set-up. At these temperatures, phase separation induced by thermal diffusion dominates, and pattern formation results into high aspect ratio structures of sponges, walls, or pillars. Metal silicide at these temperatures is polycrystalline and grazing incidence X-ray Diffraction (XRD) scans demonstrate that it is also limited by the available composition, i.e. it depends on distance to the Fe plate. Nanoscale patterns produced from room temperature to 660 K or cone patterns induced at even higher temperatures are seen to be linked to silicide formation as the crucial step for pattern (roughness) build-up. Pattern formation remains largely temperature-independent, as long as the ion-beam-induced mobility exceeds thermal mobility. As soon as thermal mobility supersedes ion-induced mobility, pattern formation becomes strongly temperature-dependent [118].

Medium-energy ripples. The findings described in the previous section correspond to low-energy (< 10 keV) ions. The performance of similar experiments at medium energies also provides relevant information about the process of IBS nanopatterning with metal co-deposition. In particular, it is interesting to check whether the same behaviors and mechanisms are operative for higher ion energies. As already mentioned, for medium-energy ions the penetration range (i.e. ion-induced amorphous layer) and the pattern features (larger W and ℓ) are amplified. Therefore, the influence of metal impurities and, specially, their distribution can be studied with improved resolution. Since medium energies in the 10–100 keV range cannot be achieved with conventional ion sources, such kind of experiments requires the use of ion implanters. Hence, following the spirit of the previous low-energy experiments in [32,33], Redondo-Cubero et al. [35] carried out ion implantations with 40 keV Ar^+ under metal co-deposition. This experiment was also carried out using a similar set-up to that displayed in Fig. 26, allowing direct comparison with the low-energy case. However, the main difference is that now the incidence angle is $\theta = 60°$, for which patterning is induced on the surface by IBS without metal co-deposition. This condition was chosen in order to additionally compare the pattern dynamics with the metal-free case reported in [89], see Section 3.1 for further details.

Concerning the metal content, the lateral profile found is in very good agreement with the low-energy one, i.e. there is a maximum close to the metal plate and the concentration decreases with distance. In addition, the metal content clearly saturates for long irradiation times. However, the steady-state value found is roughly one order of magnitude higher ($\sim 10^{17}$ Fe atoms/cm^2) than the one reached at low energies [32,33,64]. This difference is explained by the higher in-depth ion beam mixing, and by radiation-enhanced diffusion at medium energies [119], resulting into a deeper Fe incorporation. High resolution XPS studies of the patterned samples also demonstrated the existence of a chemical shift of 0.45 eV in the binding energy of the Fe peak with respect to the pure metal case, which agrees with the formation of iron silicide ($FeSi_2$) [35]. This silicide formation might be partially enhanced at medium energies, even inducing the formation of nanocrystals, due to the larger ion-induced mixing and thermal spike processes.

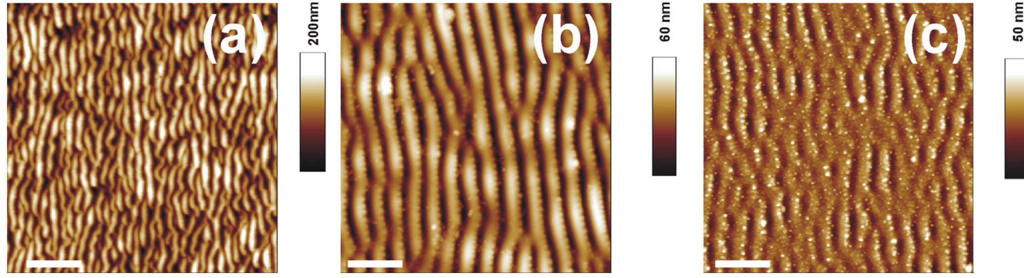

Fig. 28. AFM images of Si irradiated surfaces for 2 h by 40 keV Ar^+ impinging at $\theta = 60^\circ$ and measured at d = 1.5 mm (a), 3 mm (b), and 5 mm (c) away from the steel target. The ion beam goes from the left to the right of the images, whereas the direction of the Fe flux is the opposite. The horizontal bars correspond to 2.5 μm. Adapted with permission from [35]. Copyright 2012, American Physical Society.

Furthermore, HR-TEM analysis showed that this silicide is mainly confined within the outermost layer of the surface patterns. Moreover, it is mostly in an amorphous state, although small nanocrystalline grains are sporadically observed. Interestingly, the formation of crystalline silicide phases has been also reported recently at low energies, but only at very high temperatures [117]. Hence, these results suggest that thermal spike effects might play a significant role at intermediate energies.

Redondo-Cubero et al. [35] carried out a similar analysis to the one performed at low-energy in [32,33], studying how the pattern morphology depends on the distance to the metal plate, d. In addition, the pattern dynamics was addressed at three different d values. The pattern morphology changed from a ripple or faceted pattern close to the metal plate, to a dotted ripple pattern at larger distances, and a slight ripple morphology at the largest distances, as illustrated in Fig. 28. Thus, these experiments show that at higher ion energies the pattern morphology also depends on the Φ_{metal}/Φ_{beam} ratio. Moreover, the patterns found at larger d evolve, for long enough irradiation times, in a form that resembles the short time evolution of those which are closer to the metal plate. In fact, the sequence displayed in Fig. 28 with decreasing distance from (c) to (a) is equivalent to that found at a given d for increasing irradiation time. Furthermore, the pattern dynamics is slower as d is higher.

Under low-energy IBS with metal co-deposition, silicide phase-segregation was observed [32,33]. At higher ion energies, silicide formation has been detected by XPS [35]. In order to study whether there is any silicide segregation, an ensemble of techniques were employed, such as EDX (both in TEM and SEM facilities), XPS, and conductive AFM (C-AFM) [35]. In particular, the novel use of C-AFM to study IBS nanopatterns, proved to be a powerful technique to address silicide formation at the early stages of pattern formation. This analysis relies on the fact that Fe-richer regions (silicides) are more conductive (yield higher currents) than the surroundings. Thus, it was possible to demonstrate by C-AFM that Fe-rich silicide nanodomains form randomly on the surface during the early stages of irradiation, uncorrelated with ripple formation. Thus, some segregation exists before the pattern emerges, but this ripple formation is not triggered by compositional-dependent sputtering (recall that the angle of incidence is 60°). As the ripple structure evolves, a preferential formation of Fe-rich dots takes place, due to the glancing angle of the Fe flux, that leads to the onset of shadowing effects in the deposition process. Fig. 29 displays the topographic and current images taken simultaneously on the same area of this morphology. Clearly, the dot structures yield a higher current due to their silicide composition. This silicide composition induces a decrease of the sputtering rate of the dots as compared with that of the surrounding area. This is the reason why they constitute isolated dots.

Because of the geometrical conditions imposed by the emerging morphological features and the glancing deposition of metals, preferential formation of silicide aggregates takes place on the side of the ripple pattern that faces the metal flux. Once this compositional pattern forms, the reduced sputtering rate of the silicide phase and the asymmetry in the ion-metal fluxes contribute to further roughening of the pattern morphology. This subsequently promotes faceting due to the shadowing of the incident ion beam by the most protruding features. This long-time pattern is characterized by a saw-tooth morphology along the projection of the ion beam direction, similar to the one previously reported on metal-free silicon surfaces [88,84]. For prolonged irradiation of Si targets by inert ions, this faceted morphology evolves and displays a sympathetic increase with time of its amplitude and wavelength [45,120,17]. In such asymptotic conditions, the facet inclinations become quite close to being parallel or normal to the ion flux direction, with a strongly bimodal slope distribution. Such a morphology can be seen in the TEM image in Fig. 30(a). As irradiation proceeds, the facets originated in

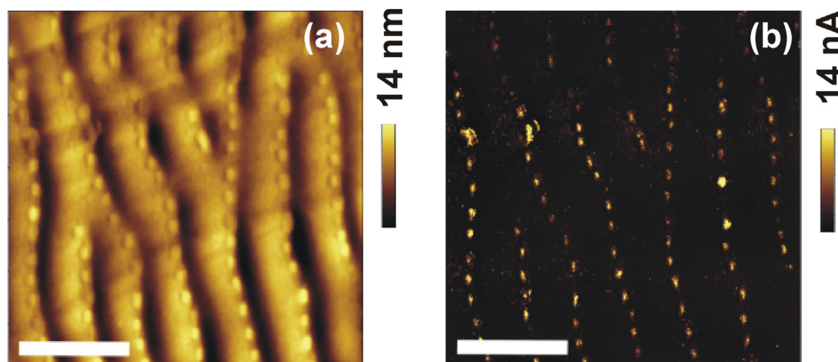

Fig. 29. Simultaneous topographic and current AFM images of the dotted rippled morphology produced by 40 keV Ar^+ irradiation at $\theta = 60^\circ$. Note how the dot structures yield higher currents. The bar indicates 1 μm.

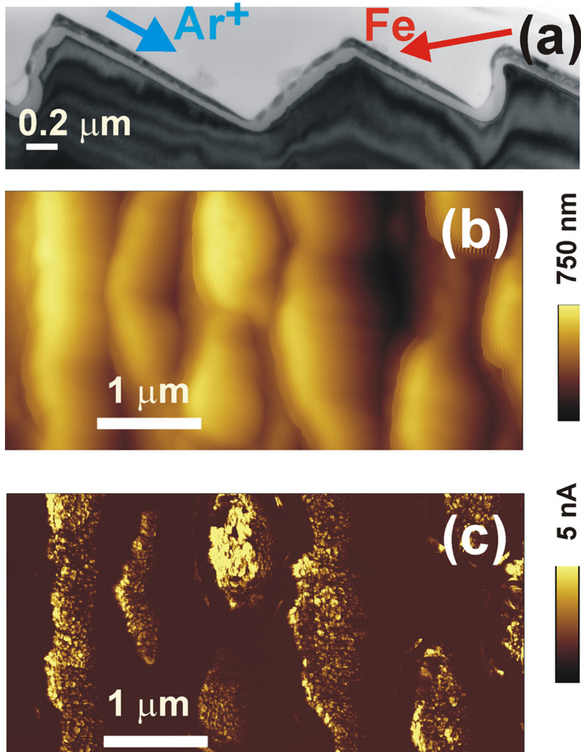

Fig. 30. (a) Bright-field TEM image of the saw-tooth structure formed at $d \simeq 1-2$ mm from the Fe source after 16 h of irradiation. Note the continuous Fe-rich slab on the rear ripple sides in contrast to the discontinuous Fe agglomeration on the front sides. The fringes are due to sample thickness fluctuations. The Ar^+ beam and Fe flux directions are indicated. Topographical (b) and C-AFM (c) images measured simultaneously on well-developed faceted structures located at d = 1.5 mm after 8 h of irradiation. Adapted with permission from [35]. Copyright 2012, American Physical Society.

this way grow substantially in roughness and wavelength. Moreover, the metal flux becomes shadowed on the sides facing the ion beam by the rough saw-tooth morphology. Thus, the Fe-rich silicide domains are mostly found on the sides that face the metal plate. This is evidenced in the TEM image of Fig. 30(a) by the darker contrast (denser material) preferentially obtained on these sides. Moreover, the topographic and C-AFM images, Fig. 30(b) and (c), respectively, clearly show an enhancement of the measured current on the rear slopes. Therefore, these results demonstrate the development of both, a faceted topographical pattern and a compositional pattern, with typical scales in the micron range.

3.2.3. Mechanisms for IBS patterning with metal co-deposition: systematic studies

Relevant conclusions can be drawn from the systematic experiments described above. Thus, Zhang et al. [32] explained their results on the basis of phase-separation of the amorphous silicide surface region into regions with higher and lower Fe content, driven by ion-induced diffusion. This process could induce local changes in the sputtering rate, giving rise to development of roughness and the nanodot pattern formation. Later on, the directional deposition of the Fe atoms on this patterned morphology would lead to the appearance of shadowing effects that result into ripple development.

Likewise, Macko et al. [33] also singled out these effects, sputtering rate differences, preferential deposition, and shadowing as a result of the directional metal deposition, as important reasons for the observed behaviors. However, they noted that in all these experiments the metal co-deposition was strongly coupled to the ion beam irradiation since the deposited metal was in fact sputtered away from the adjacent metal plate by the same ion beam. Thus, Macko et al. [33] designed a nice experiment in order to assess the generality of their results. They irradiated a silicon surface with 2 keV Kr^+ ions at $\theta = 30°$ and, simultaneously, evaporated the metal atoms on the silicon surface. With this experimental arrangement, they had independent control on the angle between the ion beam and the metal flux, and on the ratio between the metal and ion fluxes (Φ_{metal}/Φ_{beam}). Fig. 31 shows the morphologies obtained under coupled co-deposition (insets) and uncoupled co-evaporation (large images) for equivalent Φ_{metal}/Φ_{beam} ratios. In this case, the ion beam and the Fe fluxes impinge at 30° and −75°, respectively. The similarity between both types of patterns is evident. Moreover, when the angle between the ion and metal fluxes was decreased to 30°, no pattern was observed for the same ion fluence. Thus, the angle defined by these two fluxes seems to play an important role. This contradicts the conclusions of Zhang et al. [32], which ruled out directional effects as the primary cause for pattern formation, but is consistent with the observation of nanodot formation at normal incidence with metal incorporation from the target-fixing metal clamps [13,121]. In addition, the Φ_{metal}/Φ_{beam} ratio proved to be a critical parameter for the selection of the pattern (dot, hole, or ripple), as shown in Fig. 31. This is in agreement with the findings of Zhang et al. [32], under the assumption that metallic content increases with Φ_{metal}/Φ_{beam}, and with those of Sánchez-García et al. [111] for normal incidence experiments in nanodots/nanoholes using quite a different experimental set-up.

In the light of the findings described above, a model based exclusively on phase separation and diffusion cannot sufficiently account for all the features obtained under metal co-evaporation.

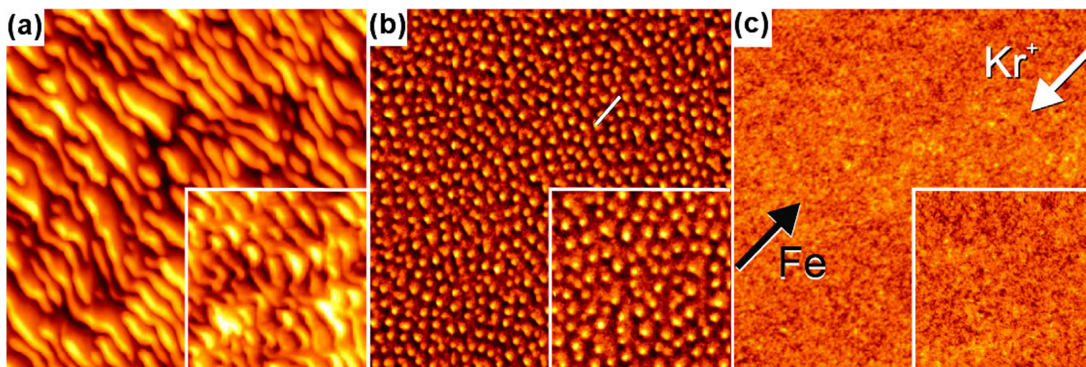

Fig. 31. Morphologies found for 2 keV Kr^+ IBS ($\theta = 30°$) experiments with metal co-evaporation (incidence angles $\theta = 30°$ and $\theta_{Fe} = -75°$) at 300 K for different Φ_{Fe}/Φ_{Kr}: (a) 0.04, (b) 0.03, (c) 0.01. Insets correspond to equivalent morphologies for IBS experiments with metal co-deposition at 300 K. The image sizes are 1 μm × 1 μm. The inset sizes are 500 nm × 500 nm. Adapted from [33] under a Public Open Access License.

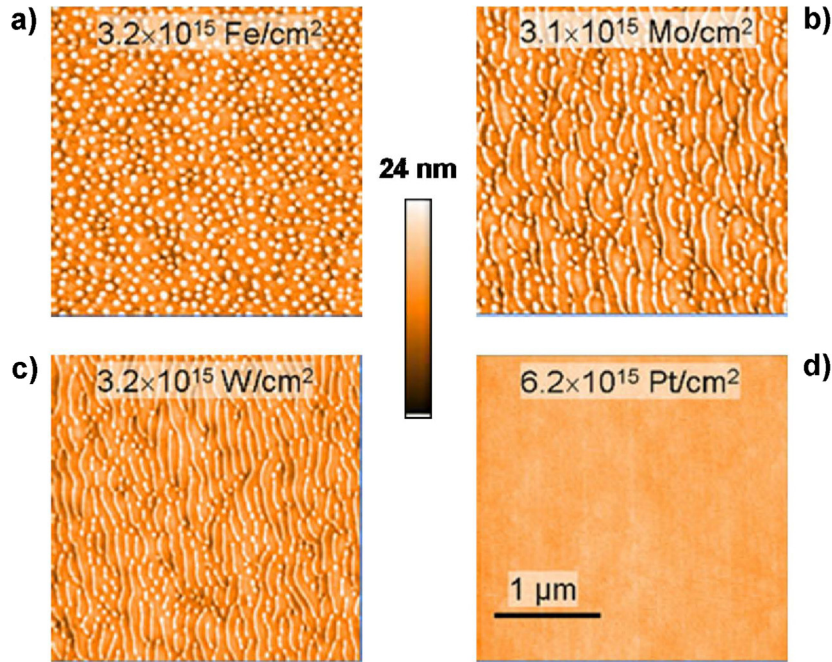

Fig. 32. AFM topographic images of surface patterns induced on silicon at a fluence of 5×10^{17} ions/cm^2 using 5 keV Xe^+ ions at normal incidence. The set-up was as shown in Fig. 26 with a 60° plate tilt and for different co-deposited metal atoms: (a) Fe, (b) Mo, (c) W, and (d) Pt. The metal surface coverage was measured with RBS and is indicated in the label for each case. Adapted from [122] under a Public Open Access License.

Thus, Macko et al. [33] proposed a scenario in which patterns essentially arise from (*i*) height fluctuations due to ion impacts, (*ii*) preferential silicide formation on the slopes facing the incoming Fe flux, leading to a compositional pattern, and (*iii*) further amplification due to erosion-rate differences on both sides of the surface features.

It is important to note that, except for the mechanisms triggering the pattern formation, the models proposed in [32,33] coincide in several aspects, particularly in the formation of a metal silicide and the promotion of the pattern via composition-dependent sputtering [40]. This paradigm is also in agreement with the results obtained at higher energies [35]. Under medium energy conditions, ripple formation occurs due to the high incidence angle (above threshold without metal co-deposition), and is uncoupled from the metal silicide segregation. In turn, selective silicide formation occurs on the rear slopes of the ripples due to shadowing, which leads to local changes in the sputtering rate and compositional and (faceted) morphological patterns.

The relevance of silicide formation and the emergence of sputtering rate differences on the target surface were recently confirmed by Hofsäss et al. [122]. In this study, the authors again used the same experimental set-up depicted in Fig. 26 with a plate tilt of 60°, but now different plate materials were employed. Specifically, they used Fe, Ni, Cu, Mo, W, Pt, and Au plates and irradiated each metal plate-silicon target ensemble with normal incidence 5 keV Xe ions. The selected metals can be divided into two groups, Fe, Ni, and Cu, on the one hand, and W, Pt and Au on the other hand. Each group is homogeneous with respect to the collision cascade behavior, but the two groups differ strongly with respect to their tendency to silicide formation. In fact, clear ripple patterns were only observed for co-deposited metals (Fe, Mo, Ni, W, and Pt) which are prone to the formation of mono and disilicides. Some of the morphologies obtained in [122] are shown in Fig. 32.

However, there seems to be more than silicide formation to pattern formation in these experiments. As Fig. 32 clearly shows, there seem to exist differences among the topographies obtained, depending on the metallic species. Under similar contents [see panels (a)–(c) in Fig. 32], when Fe is employed an isotropic nanodot pattern is produced, whereas for Mo and W a sort of anisotropic dot-ripple nanostructure develops, the ripples being longer for the W case. In contrast, for a metal content which is roughly two times higher, Pt incorporation induces a flat morphology [Fig. 32(d)]. It should be noted that for longer (larger) irradiation times (metal content) a ripple morphology develops in all four cases. Thus, although silicide formation and segregation evidently play key roles in metal-induced pattern formation, the operating mechanisms that may explain morphological differences like these remain to be fully understood, and should be addressed in future works.

Silicide-induced patterning has been also addressed very recently by Engler and co-workers [123]. In this work, 2 keV Kr^+ irradiation simultaneous with metal co-deposition has been performed using a similar experimental set-up for Pd, Ir, Ag, and Pb. The first two elements do form silicides, whereas Ag and Pb do not. Also, Ag-Pd and Pb-Ir are close in nuclear charge, which allows to distinguish between collisional and chemical effects. In agreement with [122], only the co-deposition of metals prone to silicide formation did lead to surface nanopatterning. However, the authors of [123] argue that the ability of the co-deposited metal to form silicide appears to be a necessary, but not a sufficient condition for nanopatterning. Such a conclusion is derived both, from the experiments in [123], and from comparison with previous experiments in which the co-deposited metal was supplied by evaporation, and, therefore, was uncoupled with the irradiation process [33]. In this sense, a bi-directional coupling between surface composition (phase separation) and height fluctuation is proposed to lead to the surface destabilization which finally leads to pattern formation. Interestingly, in [123] the authors performed TRIMP simulations to evaluate the erosion rate of silicide domains. Surprisingly, it was found that for Pd and Ir the erosion rate of the corresponding silicides was larger than that of pure Si. This finding contradicts the role of preferential sputtering as one of the driving forces for IBS patterning with metal co-deposition. However, the authors argued that, as in the steady-state regime the eroded metal is immediately replenished, only the partial silicon sputtering rate

within the silicide, which proved to be lower than in the Si regions, has to be considered. This fact has to be confirmed. In any case, the argument would apply to the steady-state regime, but not to the initial stages of patterning in which the metal content is evolving.

In the assessment of impurity effects, a novel experimental strategy that seems promising is the use, under impurity-free conditions, of a beam of metallic ions (i.e. Fe^+). This idea was formerly suggested by Macko et al. [33]. This set-up avoids anisotropies in the metal flux (usually from the adjacent metal plates), and misalignment between the directions of the ion and the metal flux directions. The first work employing this approach has been reported by Khanbabaee et al. [124]. Thus, these authors implanted a Si(0 0 1) wafer homogeneously with a scanned Fe^+ beam of 5 mm diameter at 5 keV ion energy and $\theta = 65°$, for different total fluences. They only reported a ripple pattern for an intermediate fluence. Following their previous work [115], they studied the samples by XRR. These studies showed the incorporation of Fe atoms in a 5 nm layer below the surface, with a maximum density at a depth of about 3–4 nm. For patterned surfaces the strong decay in the reflected intensity hinders a detailed evaluation. However, XRD analysis did reveal a net reduction of the surface density in all implanted samples, which was explained on the basis of the roughening and likely amorphization of silicon [124].

From the above, it is clear that the most systematic efforts to investigate the mechanisms involved in IBS patterning with metal co-deposition have been made in systems in which the metal flux is rather directional, i.e. when anisotropic ripple patterns develop, even if isotropic patterns may emerge at short times. In contrast, there are not many studies for the case of nanodot patterns, like those described in the first part of this section. In general, the main efforts in this field have been devoted to the production of ordered patterns, or to the analysis of the pattern dynamics, but not to the specific mechanisms leading to nanodot patterns with short-range order. Interestingly, we have illustrated how the dynamics can be quantitatively explained by continuum models that employ two fields, one for the height and a second one for the composition of the irradiated surface. This will be further discussed in the theoretical section. Actually, a number of models have been very recently proposed along these lines, but so far few of them feature a dedicated set of experimental studies designed to validate the theoretical predictions. In this context, we can e.g. note the work by Zhou and Lu [125], which does compare experimental data with theoretical analysis. In this study, in the presence of Fe, a surface stress-induced instability together with curvature-dependent erosion is argued to overcome ballistic smoothing, leading to formation of a dot pattern. In addition, preferential sputtering, cooperating with the morphological instability, would account for the patterning in composition. Studies like this show how the understanding of IBS patterning has progressed in the last years. But, at the same time, they suggest the importance of issues which remain to be investigated, such as universality and material independence of the process, influence of the ion/target combination, stress, effects associated with the sputtering rate, etc. Now, once the experimental scenario is becoming more clear, the conditions to undertake more refined studies are adequate in order to reach meaningful and consistent conclusions.

4. Atomistic simulations

In this section we attempt a bridge between the experimental observations provided by many groups worldwide, of the type described in the previous section, and the theoretical continuum approaches that are employed to describe the large-scale properties of surface nanopatterning by IBS of silicon targets. The great benefit of theoretical models is that they can help to unveil the role of the physical mechanism under consideration. Hence, either through reproducing experiments or by providing novel predictions, such type of models can be tested. However, being mainly based on partial differential equations, they often lack the ability to provide quantitative predictions beyond trends or order-of-magnitude estimations, because some of the parameters in those equations are either unknown or cannot be easily determined from empirical data.

In this context, numerical simulations appear as an ideal alternative to theoretical models. This approach relies strongly on the computing feasibility and the level of description which is required in each case. Thus, computer technologies determine the degree of detail that simulations can encompass. However, as we summarize below, the great majority of works performed in this area do not address the general problem of pattern formation by ion-beam erosion, and have been limited to ion-matter interactions. This is not due to a lack of interest, but rather to the strong computational limitations to access the macroscopic time scales at which non-trivial pattern evolution unfolds.

4.1. Physical mechanisms involved in IBS

At a microscopic level, ion-beam irradiation of solid targets involves a large number of processes and mechanisms, making its precise theoretical description a challenging goal that would properly require a multi-scale approach, given the wide range of time and length scales involved in the relevant processes. Nevertheless, here we will highlight the most significant physical mechanisms that are relevant to the discussion in the following sections.

4.1.1. Mechanisms related to ion damage

Generally speaking, the most salient phenomenon associated with ion-beam bombardment is the generation of cascades of atomic displacements in the target, by the impact of the energetic ions. When an ion collides with a target atom, it exchanges kinetic energy producing what is referred to as a *recoil* [50]. The displaced atom and the ion can induce further collisions, and similarly for subsequently displaced atoms, in such a way that a collision cascade is generated. These collisions are actually highly complex many-body processes which involve the nuclei and electrons of the ion and target atoms. In this way, the beam induces both energy deposition and matter rearrangement in the eroded solid. These processes allow for a statistical description whose detailed properties depend on the mass of the ion and the target atoms and, of course, on the ion energy. For instance, regarding energy deposition, a linear cascade approximation restricted to binary atomic collisions leads to a Gaussian distribution for their shape around the initial ion track [126], that agrees quite accurately with experiments for ion energies in, say, the 100 eV to 10 keV range [50]. This collective collision cascade creates many defects, changing dramatically the local order inside the amorphous layer, which is quantitatively different from that of an as-grown amorphous Si sample (see Fig. 33).

With respect to material redistribution, Si becomes amorphized and stressed under this type of irradiation [12]. Partial relaxation of defects, as mentioned above, leads to the generation of a residual stress that is confined to a thin amorphous layer which builds up beneath the surface, and which reaches a stationary thickness shortly after the early times of irradiation for the typical flux values considered in the previous sections [128–130]. On the other hand, also *surface* redistribution effects take place, through the generation of permanent displacements of the atoms near the surface, also known as *craters*. The potential contribution of these to the dynamics of the target surface in macroscopic time scales has started to be assessed by Molecular Dynamics (MD) simulations

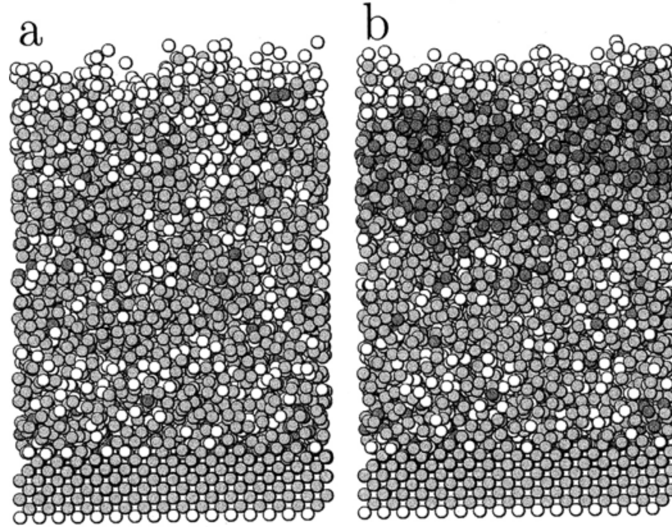

Fig. 33. Cross-sectional view (20 Å thick) of an irradiated Si target (a) before and (b) after irradiation with 0.1 keV Si atoms for a fluence of 2.6×10^{15} atoms/cm^2. Atoms are shaded according to their coordination number Z_i. White: under-coordinated ($Z \leq 3$). Grey: 4-fold coordinated ($Z = 4$). Dark: over-coordinated ($Z \geq 5$). As can be seen, the effect of irradiation goes beyond a mere amorphization of the sample. In this sense, it would be more accurate to refer to irradiated Si as *damaged*, rather than simply *amorphous*. Reprinted with permission from [127]. Copyright 2001, Elsevier.

only very recently [131–134], although limitations to the procedure seem to exist [135–137]. In Fig. 34 we show a single crater simulated by MD by argon irradiation of silicon at oblique incidence.

Finally, also when the interaction is sufficiently close to the surface, some displaced atoms receive enough energy so that they can break their bonds and be ejected away (*sputtered*) from the target. This is the effect that ultimately leads to net erosion of the latter. The dependence of the efficiency of sputtering with many experimental conditions, such as average ion energy and flux, ion/target combination, etc. has been thoroughly studied [50]. In particular, surface effects are expected to decrease in relevance for increasing energies due to an increased ion penetration. Also for increasing energies, the main contribution with respect to ion stopping within the bulk changes from nuclear (100 eV to tens of keV) to electronic-dominated (above 100 keV) scattering [50].

4.1.2. Mechanisms related to material relaxation

Kinetic energy transfer from the ion beam does not only contribute to driving the solid away from local equilibrium, but it can also contribute to the enhancement of counteracting relaxation mechanisms that aid in reaching such a local equilibrium state. A noticeable one is local thermalization, usually referred to as thermal spike formation. Thus, the energy supplied by the ion allows defects, such as vacancies and interstitials, created in the collision cascade (or residual defects that exist in the material due to previous cascades or to its previous state) to overcome energy barriers and eventually annihilate, either by recombination, or by migration to the free target surface, see e.g. [2] and references therein. Point-defect diffusion and vacancy-interstitial recombination have very complex behaviors which can be studied by MD simulations. See the work in Ref. [138] for a in-depth study of these phenomena.

In particular, the role for IBS of the so-called ion-induced viscous flow, historically formulated in the context of interface relaxation of fluid media by Mullins [139], has been recently recognized [140]. As will be seen below, under appropriate conditions this type of flow may be restricted to a thin layer underneath the surface [141] (hence being referred to as surface-confined viscous flow), and may actually be the main surface relaxation mechanism, as stressed in Ref. [142].

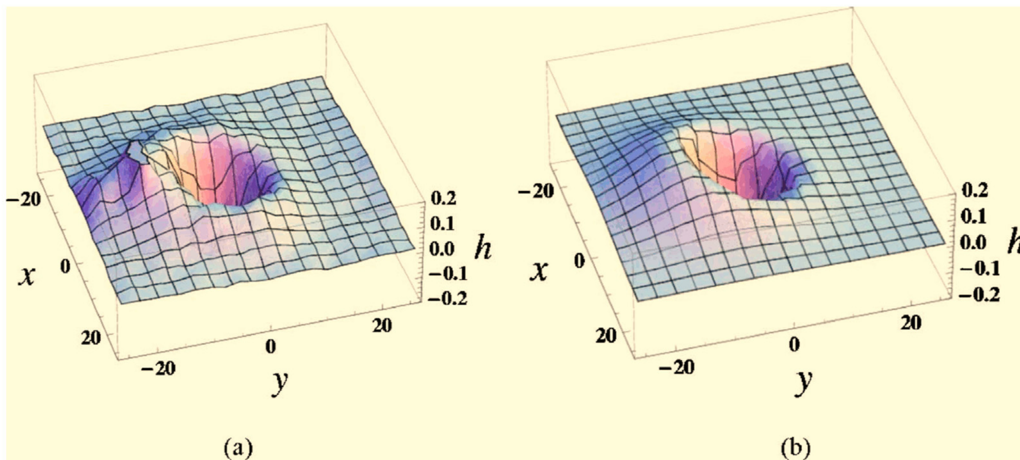

Fig. 34. Comparison between the average crater shape (left) induced by a single 0.5 keV argon ion as computed by MD and a fitted crater function (right), for an incidence angle $\theta = 28^\circ$. All dimensions are in angstroms. Reprinted with permission from [131]. Copyright 2008, AIP Publishing LLC.

Aside from the external driving imposed by the ion beam, thermal fluctuations also mediate relaxation mechanisms which in general lead to an overall healing of damage in the material. For instance, available species (adatoms, ad-vacancies) can migrate on top of the surface (*surface diffusion* [139]), or else get stuck as induced by local energy barriers at the surface. This phenomenon is specially important in the case of metallic targets, see e.g. [23], for which there are parameter ranges in which surface diffusion kinetics dominates over the ion beam with respect to the induced surface dynamics, although this is beyond the scope if this work. Both bulk and surface diffusion are thermally activated process whose rates show an Arrhenius (exponential) dependence on temperature. Consequently, they are expected to be more relevant for higher temperatures, although the interplay between temperature and other experimental parameters may be far from trivial [23,2,3]. For the specific case of Si, as has been mentioned above, experiments at high enough T indicate that the target actually recrystallizes very efficiently, which does not necessarily free its dynamics from morphological instabilities [79,80].

4.2. Overview of numerical simulation methods for IBS

From a historical perspective, the evolution of these techniques ranges from very small systems in which the focus was made on the best choice for the interaction potential, to large-scale simulations of implantation events catalyzed by the interest of implanted Si for the semiconductor industry, thus motivating exhaustive collections of quantitative data obtained by MD [143].

In general terms, we can distinguish among three approaches, each of them having their own merits and limitations. At the highest level of description, the dynamics of atoms under irradiation can accurately be described by the so-called *ab-initio* methods (see Ref. [143] and references therein). Their main goal is to obtain effective interaction potentials from quantum mechanical descriptions of the ion-atom interactions. This approach involves huge computational efforts and has been traditionally used to test other *coarser* approaches like Molecular Dynamics or Monte Carlo (MC) simulations [144].

Both *ab-initio* and density functional theory methods are not very widely used in low energy simulations of Si irradiation, as they can only simulate 10^2 molecules, hence we refer the reader to Refs. [145,146] for some examples.

At the next level of description we find Molecular Dynamics methods (MD). Here, the atoms are considered as classical *particles* (namely, they obey Newton's laws) subject to effective interaction potentials that are tested to determine if they are able to reproduce accurately different physical observables and properties, such as, for instance, the melting point. They typically connect the micro and macro-world through the application of Statistical Mechanics [147]. Although MD simulations are computationally more efficient than ab-initio approaches, they are still limited both in time and space. Notwithstanding, with the proper choice of potential, they have been proven to successfully reproduce quantitative information from experiments.

The coarser level of description (and, hence, the fastest one) is generically termed Monte Carlo methods (MC). In this case, the dynamics of events occurring in the irradiation process is discretized into a number of known *reactions*. Statistical sampling of these reactions provides a fast way to explore large scale situations. Among MC methods, the most widely spread one is based on the celebrated Binary Collision Approximation (BCA) [148]. BCA models, in general, and Transport of Ions in Matter method (TRIM) in particular [149], comprise the majority of works in this and related fields. However, in this review, we will focus only on those works that conceptually address low-energy irradiation on silicon, as the literature on ion-matter irradiation is otherwise huge. However, accurate MC simulations require precise knowledge of the dynamics of defects. Thus, hereafter, we will focus almost exclusively on MD approaches to Si irradiation. Thus, although the works on MD were scarce until very recently, their interest has reborn since, together with MC, they are known to predict some relevant observables with a reasonable accuracy, specifically at low energies.

4.3. Historical account of simulation results

4.3.1. Early works: comparison between methods

One of earliest attempts to test the validity of the three approaches mentioned above was the work by Eckstein et al. [144]. In that work the coefficients of reflection and sputtering yields were compared for TRIM, *ab-initio* methods, and different MD potentials (in particular, Molière and Ziegler, Biersack and Littmark (ZBL) potentials). The authors showed that, while the two observables were similar in all cases, there were some significant differences among them, which limits the range of validity of TRIM or MD. More recently, BCA and MD simulations have been similarly compared in Ref. [150].

Another huge leap regarding the validity of TRIM was performed by Norlund [151]. Although limited by current standards, this author showed that recoils cannot be accurately simulated using TRIM. Moreover, the range of energies available for MD simulations is also very limited. That work also opened the door to specific improvements in the simulation procedure that could accelerate the simulation time, thus allowing MD to be used to determine ion ranges and deposited energies of recoils.

As a follow-up of the pioneering work in Ref. [151], several potentials were tested shifting the focus from the events on the surface (i.e. the yield) to those occurring beneath the surface (defect creation) [152]. From a less fundamental perspective, the same group compared the dynamics of semiconductors with that of metals. They concluded [153] that the main difference between them is that, for the former, the damage created at the surface does not change strongly the damage in the bulk phase. Once the potentials were tested, more accurate calculations of the collision cascades can be used as an improvement over TRIM results [154].

Once the need of using a MD approach over TRIM was settled, there have been many efforts to determine the optimal potential to quantitatively predict experimental observables. To cite a few, some have focused on the sputtering yield [155], ion ranges [156], or implantation curves of different dopants [157].

4.3.2. Amorphization and annealing after irradiation

In general, most of the works on Si irradiation performed up to date (with notable exceptions) deal with the interaction between a single ion and a crystalline silicon target. In these cases, there are strong effects due to the orientation of the crystal planes. Thus, using an Stillinger–Weber potential and a novel way to quantify the degree of disorder, in Ref. [158] the role of crystallinity on surface reconstruction and bulk annealing was accounted for. In Ref. [158] the authors showed that, despite the well-known role of ion channeling in crystal irradiation, the precise angle of incidence does not change significantly the relaxation of defects. This result is important since, in typical ion-beam experiments, the material is amorphized [159] long before the patterns start to develop, thus pointing out to defect relaxation in the amorphous phase, rather than to the existence of preferential directions in the crystal, as the main cause of viscous flow.

Also focusing on the dynamics of defects on the surface, some works were devoted to the specific role of ion interactions on surface step reconstruction [160] (a more recent account of this problem can be found in Ref. [161]) or as a way to assist epitaxial growth [162]. Besides, the specific form in which amorphous

pockets relax is far from trivial [163,164], motivating the need to combine MD with kinetic Monte Carlo simulations for the relaxation events, see [165] for a thorough account of these combined methods. Actually this type of kinetic MC relaxational mechanisms have been very recently combined with a BCA description of the ion–solid interaction by Liedke et al. [166]. In this work the three-dimensional evolution of Si targets under Ar^+ irradiation at low energies and oblique incidence angles is actually described, with promising results with respect to the ripple formation process, albeit in absence yet of detailed descriptions on the dependence of pattern properties with experimental parameters.

Although MD was gaining popularity in this context in the late 1990s, elucidating the most accurate potential for low energies has recurrently been studied by analyzing different criteria. In Ref. [167], based on the dynamics of defects and a quantitative account of the Si melting point, the authors suggested that Tersoff's potential is a better alternative than previously used potentials, both binary, as Molière's, or more complex, as Stillinger–Weber.

As stated above, one of the limitations of MD at that stage of the field was related to the fact that only a few atomic collisions could be simulated, so that cumulative effects of defect creation and occasional relaxation were out of the scope of those works. To overcome these computational limitations, in Ref. [168] the authors introduced a highly parallelized software that could perform massive simulations. In particular, they were able to average over a large number of single ion impacts after an initial amorphization step, being closer to what occurs in actual experiments, in which every single ion finds a damaged material due to the effect of previous impacts. Moreover, once they produced an amorphized material, they were able to track the evolution of different properties and average them over multiple realizations. In Ref. [168] the crucial role of amorphization and defect creation was also emphasized, which was then studied in Ref. [169]. Interestingly, only a few works have focused on the topography of the surface and the concentration of surface impurities [134,170], and their influence in the sputtering yield.

Note that amorphization is specially critical in semiconductors [171], as metal atoms can diffuse more efficiently and recrystallize in much shorter time scales. In order to overcome the computational limitations of studying large doses of irradiated ions and to further understand the dynamics of defect relaxation inside the material, in Ref. [172] the authors introduced a fast simulation scheme based on two simple ideas: On the one hand, they used periodic boundary conditions to remove surface effects and, on the other hand, they generated *artificially* the distribution of velocities of the recoils to diminish the typical timescale of relaxation events while maintaining realistic velocity distributions.

Another heuristic way to study large scale systems was to employ collision cascades generated by TRIM as an input for more accurate MD simulations [173]. This procedure allows to generate surface topologies and compare them with those obtained by alternative experimental methods, such as thermally-activated solid phase epitaxy.

As mentioned, the cumulative effect of ion impacts produces the subsequent amorphization of the material and, hence, a fluence-dependent behavior. Thus, many predictions coming from simulations were not able to capture the proper range profiles. To overcome this limitation, in Ref. [174] the authors developed a method that allows to consider cumulative damage build-up. However, the most straightforward (and accurate) approach to characterize damage accumulation is by performing sequential impacts on the same target. Thus, although this method is limited by prohibitive computational times, it can still be used to assess different properties, like the sputtering yield [175] or the sharpness of the amorphous-crystalline interface [175,176], during the stage of formation of the amorphous layer.

The latter studies emphasize the need to properly account for the interplay between ion-induced damage and recrystallization. Thus, events occurring in the relatively long times between impacts can be replaced by thermal relaxation events triggered by the large power exchange between the ion and the target [177]. However, the approach in Ref. [177] neglects the fact that relaxation is a long-time process in which different stages occur at time scales separated by several orders of magnitude in time [178]. Recently, and with the use of up-to-date computational facilities, these long-term events (amorphous and defect relaxation) can be properly studied and, probably, will deserve additional efforts in years to come [179].

4.3.3. Atomistic simulations in the context of surface nanopatterning theories

Thus far, we have summarized the historical evolution of simulation approaches—with a special emphasis on MD—, with the general ion-matter interaction in mind. But this interaction is not the only one. The present is a many-body problem and there is also a huge amount of work on cluster impacts in the context of IBS, see for example [180] and quotes to that article for further information.

In recent years, and catalyzed by the promise of IBS as an inexpensive and efficient technique to produce order at the nanometric scale, some authors have focused their efforts on those questions which are relevant to the emergence of surface patterns by IBS. One of the pioneering works in these aspects is due to Moore et al. [127]. In particular, the authors were the first to simulate a large number of subsequent impacts (up to a hundred), which allowed to better understand the dynamic formation of the amorphous layer. Beyond characterizing in detail the formation and characteristics of the amorphous surface layer, the final goal of this work was to consider the influence on sputtering yields of e.g. the ensuing surface roughening and Ar implantation; see Ref. [12] for a comprehensive account of related MD results in these aspects. Along similar lines, for instance in Ref. [181] MD simulations were performed considering only erosive effects, without relaxation by e.g. surface diffusion, to study the stability of sinusoidally prepatterned rippled structures in silicon. The main result was that only long-wavelength ripples are stable, contradicting expectations from the prevailing theory at the time for topography evolution, namely the Bradley–Harper (BH) theory, to be described in the next section.

On the other hand, as will be discussed in Section 5.3, stress seems to be a relevant actor in pattern formation of this type of surface nanostructures. From this perspective, some works in the past have addressed the generation of stress in Si under irradiation, by means of MD simulations. In Ref. [182], the authors studied the relaxation of previously applied stress on a Si sample, as induced by ion impacts. Although the authors considered contributions to the stress coming from the kinetic energy (that has been shown to overestimate the overall stress [183]), they showed convincingly that defect creation and residual stress are related to the irradiation conditions. In a sequel of Ref. [182], the same authors showed that the capability of the ion to create defects goes beyond the amorphization of a crystalline material [184]. Specifically, even when starting with an amorphous material, the ion is able to create long-living defects that affect the ion range of subsequent incoming ions. Moreover, if an external stress is applied, the compressed sample shows distinct stress changes that depend strongly on the ion energy. Such a stress dependence with energy has been subsequently observed experimentally, e.g. for amorphous hydrogenated Si thin films [185].

More recently, with a simulation set-up similar to that employed in [127], Kalyanasundaram et al. [128,129] have further characterized the dynamics of stress generation for Ar bombardment of an initially flat, crystalline Si layer. Up to three dynamical regimes could be identified: an initial one after the first few impacts, in which tensile stress is produced due to creation of surface vacancies and bulk interstitials near the surface. In the second regime, ion-induced stress becomes compressive; the authors account for it based on substitutional argon defects. Finally, in the third regime stress reaches a steady value. The variation of the stress profile with depth from the free surface was assessed, concluding that higher compressive stresses are observed in regions of greater damage, see Fig. 35. The evolution of stress generation has also been studied by other groups in the range of low energies [186].

4.3.4. From MD to continuum models (crater function approach)

An alternative hypothesis to residual stress as the main driving force to account for pattern formation can be formulated in terms of the so-called crater function [187]. In this context, MD "experiments" can be performed, wherefrom the moments of a distribution function that accounts for the net effect of single ion impacts can be reconstructed. Although in principle these moments describe the topography at small scales, they can be incorporated into continuum models to describe the surface morphology at much larger scales. This in turn allows to provide estimates for many of the parameters of these large-scale formulations [188,130–133,189]. Hence, this formalism represents a multiscale approach to connect atomistic MD simulations to the continuum models which will be reviewed in the next section. The idea of the crater-function approach can be better understood in the context of the BH theory, see Section 5.1.2. The average space distribution of energy deposition employed by BH—a Gaussian as estimated by Sigmund [20]—is now replaced by a kernel which is directly evaluated by MD simulations. Thus, to some extent the crater function represents the average change in the surface shape due to a single-ion impact. In principle this procedure enables a separate evaluation of the contributions to the interface dynamics due to erosion (sputtering) and from redistribution of target atoms. In a number of works on pure Si [130,133,190], it is found that the dominant contribution arises from redistribution.

In most of the mentioned works, the erosive and redistributive effects of the impinging ions are evaluated from the MD simulations. Additional contributions to the evolution of the surface height are added *ad-hoc* in order to stabilize the patterns at small distances. Note that, as already noted by BH [19], on dimensional grounds such type of non-purely collisional contributions have to occur if one is to describe a ripple wavelength that can be much larger than the average ion penetration depth, a. Crater contributions in any case originate in collisional processes, and unavoidably scale with a. This limitation is overcome in [190], where the surface diffusion taking place at much longer time scales is treated using kinetic Monte Carlo simulations, to conclude again that mass redistribution is the main mechanism for pattern formation on Si.

In principle, crater functions have allowed to account for a number of experimental properties of IBS on Si. Most notably, the existence of a critical angle for pattern formation, or the behavior of the ripple wavelength with incidence angle [133]. Additional results have been obtained, such as the rotation of the ripple pattern for sufficiently glancing incidence angles [191]. More recently, this approach has been also adapted to the case of binary targets [192]. In this work many parameters of the differential equations describing the irradiation of binary materials (see Section 5.2.2) have been estimated. In particular, this was done for irradiation of GaSb by Ar^+ to also get, as in the case of Si, that redistribution is dominant over erosion.

Despite the appeal of the crater-function idea, the outcome of the procedure has been recently shown to strongly depend on the local curvature of the surface [134], questioning the quantitative accuracy of the approach. Specifically, most studies based on crater functions evaluate moments for planar surfaces, a procedure called truncated crater function theory [135]. However, MD simulations for 500 eV Ar^+ irradiation of amorphous Si [134] lead to the conclusion that the sputtering yield, crater functions, and the angular distribution of sputtered particles, all strongly depend on curvature. Furthermore, the neglect of curvature in the crater function leads to consistency restrictions which seem not to be fulfilled in experiments using Ar^+/Si and Kr^+/Ge ion/target combinations [135]. For incidence angles below 45°, agreement between theory and experiments remains qualitative. Similar conclusions are reached at in [136], where it is shown that taking into account curvature effects actually recovers BH results. Hence,

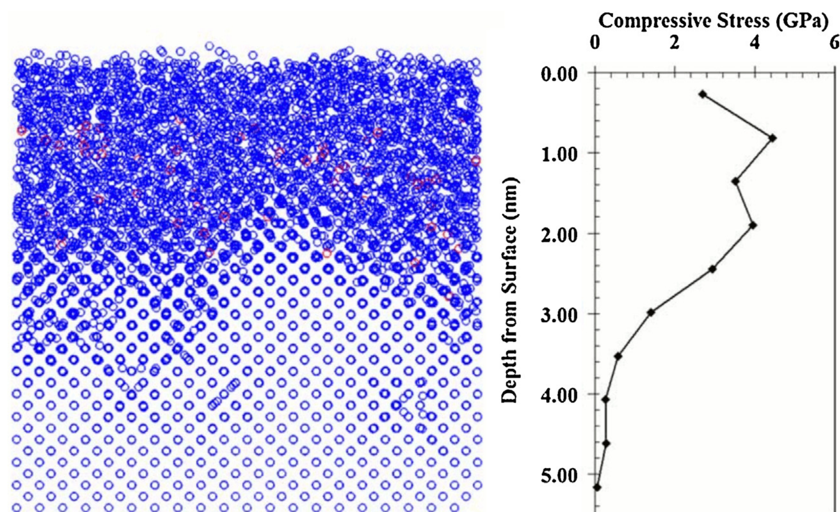

Fig. 35. Left: Amorphized silicon (blue circles) after irradiation by Ar ions (red circles) after a fluence of 2.71×10^{14} ions/cm^2. Right: Total stress as a function of depth with respect to the surface. Reprinted with permission from [130]. Copyright 2006, Elsevier. (For interpretation of the references to colour in this figure legend, the reader is referred to the web version of this article.)

the different results obtained from crater functions as compared with the classic theory may originate in the type of expansions performed. Overall, both references [135,136] similarly conclude that an accurate estimation of the parameters appearing in large-scale descriptions of IBS nanopatterning through MD-evaluated crater functions will probably require much more computational power than initially thought.

Working along a similar but alternative approach, additional recent results seem to contradict ion-induced mass redistribution as the dominating contribution to pattern formation [193]. In this work, the crater function philosophy is assumed, but MD simulations are replaced by binary collision Monte Carlo results (as obtained through SDTrimSp [194]), which provide improved statistics. Then, results are analyzed from the point of view of continuum equations, such as the BH and the Carter-Vishnyakov (CV) theories—which will be reviewed in the next section—and a proposed generalization of them (HH model). The latter includes a novel inward-relaxation term, akin to the full viscous flow process also to be described in the next section. The conclusion is that curvature-dependent erosion (namely, the BH mechanism) is the main quantitative contribution to pattern formation on silicon, for a broad range of experimental conditions. Such a conclusion is illustrated in Fig. 36, where the contributions to the curvature coefficients in the HH model from [193] are compared with the prediction from the crater-function (cf) model [133], and from the BH and CV theories. For instance, while the BH+CV or the SDTrimSp-cf analysis do not predict perpendicular ripple formation at any angle, similar to MD-based crater functions [133], the HH analysis does predict perpendicular ripple formation for incidence angles above 70°, as seen in experiments [39]. Even if a number of approximations are made (e.g. a planar surface is also assumed in the MC simulations, and the constitutive equations of the HH require strong assumptions) whose relevance to the results remain to be assessed, this approach seems a promising bridge between (approximate) atomistic and continuum descriptions. Its detailed relation to full MD simulations on the one hand, or to more elaborate continuum models capable of accounting for further physical effects, such as stress, seems worth investigating in future.

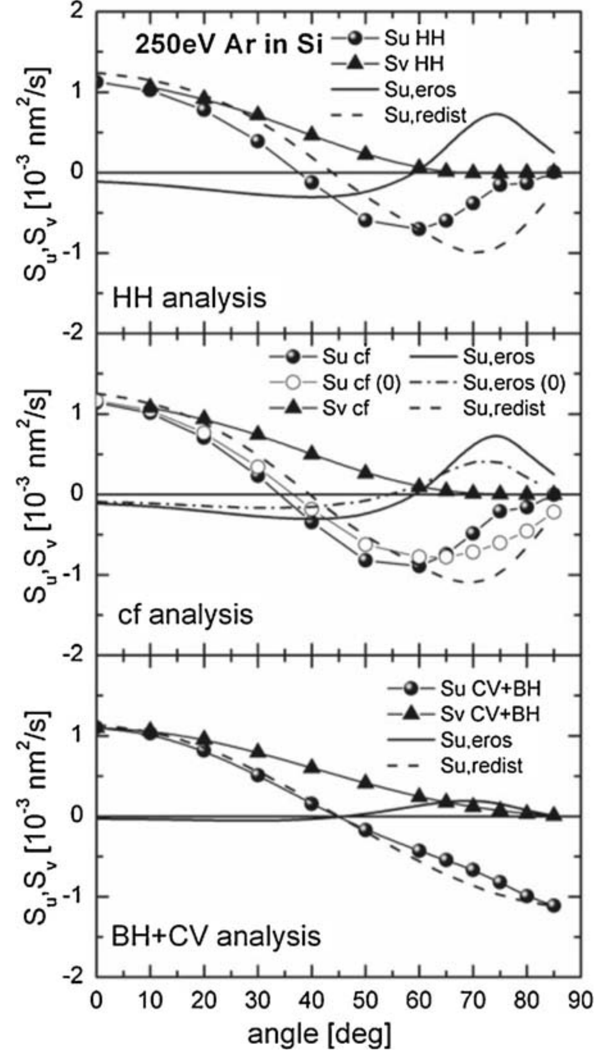

Fig. 36. Quantitative curvature coefficients contributions to the linear dispersion relation in directions parallel, S_u, and perpendicular, S_v, to the projection of the ion beam (see Section 5.1 for details) coming from the erosive and redistributive contributions, calculated within the framework of the HH model from [193], the so-called crater function (cf) as in [134], and the BH and CV theories, for Si irradiated by 0.25 keV Ar^+ ions for 1×10^{12} ions/cm^2. Negative curvature coefficients are defined as destabilizing. Reprinted from [193] under a Public Open Access License.

5. Continuum models

5.1. Early theories of IBS surface nanopatterning

We have seen in the experiments described in Section 3 that, for the ion fluxes which are usually employed, the patterns that emerge by IBS evolve non-trivially in macroscopic time scales (of the order of tens of seconds or larger), and have a coherence length that can reach several microns. As seen in the previous section, this poses a formidable challenge to microscopic modeling, since the scales that are currently reachable to e.g. MD studies remain typically below 1 ns and 1 μm. With the aim to overcome this and other limitations, it is natural to consider continuum methods, which can probe larger scales in a natural and efficient way [195,196]. In what follows, we will consider this continuum approach with a historical perspective that will allow to appreciate the successive improvements required to reach our present level of understanding of IBS on silicon.

As also discussed above, surface nanopatterning experiments by IBS were historically performed without explicit control on the degree of contamination of the samples. This was based on the large degree of universality found for the main properties of the pattern dynamics, for a wide range of ion/target combinations; see e.g. [26], [48], or [2] for overviews on the literature up to 2007. Thus, theoretical descriptions were unsensitive to composition-related issues and were based, rather, almost exclusively on the effect of ion cascades on the eroded surface. They moreover neglected the coupling of the interface dynamics to potential transport or relaxational mechanisms, even those taking place in the near-surface region.

5.1.1. Geometric methods based on the sputtering yield

Among the earliest continuum models put forward to describe the evolution of surface features under IBS, a number of them were developed in the 1970s and roughly up to the early 1990s. The starting point was the mean sputtering yield as a function of the incidence angle, $Y(\theta)$. Naturally, in principle the sputtering yield depends on many parameters, such as the energy, ion/target combination, angle of incidence, etc. [50]. For the case of Si, Fig. 37 shows experimental and simulated yield curves for different ions and energies, and as a function of incidence angle for a fixed ion and several energies [197,119].

Given the ion/target combination and the ion energy, the main qualitative features of the yield curve $Y(\theta)$ include: A non-zero value for normal incidence, an increase for small θ values—approximately as $\cos^{-f}\theta$, with $1 \leq f < 2$ within the so-called Sigmund's linear cascade approximation to sputtering [198]—, a

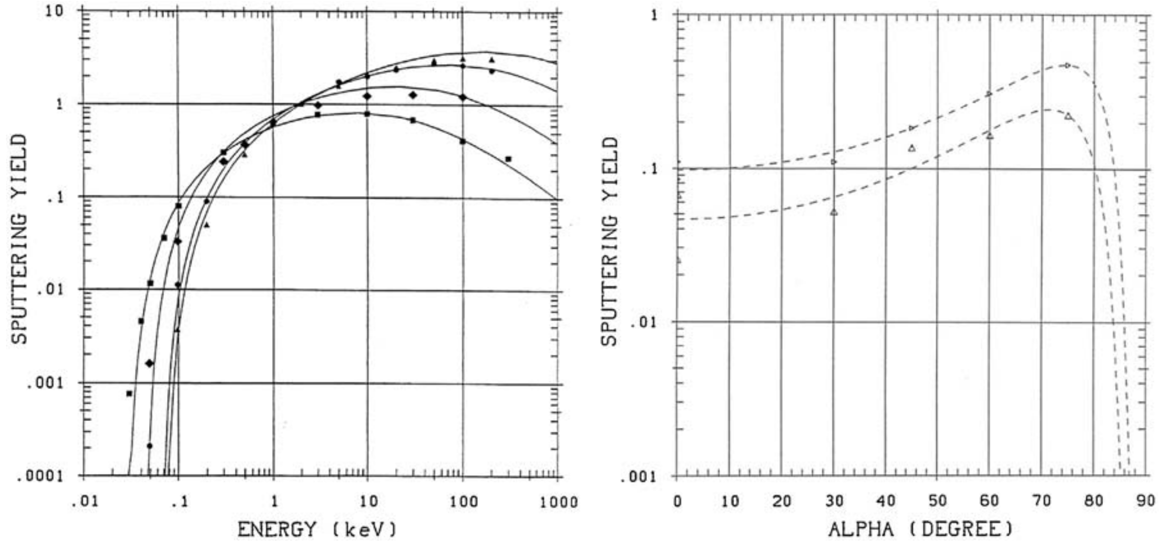

Fig. 37. Left: TRIM simulations (lines) vs experimental (symbols) sputtering yields of Si for Ne (**squarf;**), Ar (◆), Kr (●), and Xe (▲) ions, as a function of ion energy. Right: As in left panel, now as a function of incidence angle α, for He ions with energies 0.2 keV (△) and 3 keV (▹). Adapted with permission from [197]. See also [119].

finite maximum, and then a drop at very glancing angles due to e.g. ion reflection at the surface. If needed, such a drop can be empirically parameterized with a high precision [199]. Based on these behaviors, a number of continuum theories attempted to describe the time evolution of surface features, by assuming that the average yield curve $Y(\theta)$ illustrated in Fig. 37 can be assumed to also hold locally at an arbitrary surface point. Then, the main idea is to assume that the surface erodes along the local normal direction there, with a velocity that depends on the sputtering efficiency $Y(\theta)$. Therefore, the interface is considered to evolve as a wavefront obeying a form of Huygens principle. Various methods that implement this idea are surveyed relatively recently by Carter in [48]. Although they can account for a number of properties of *erosion* systems and can make contact in a natural way to more general interface problems including *growth* systems [200], we will not pursue them further here. As remarked in [48], these continuum models are appropriate to describe feature development above one micron, but not the type of nanometric-sized patterns we are presently interested in. Mathematically, in terms of the function $h(x, y)$ that represents the height of the eroding surface above a reference point (x, y) on the target plane, these approaches are sensitive to low order derivatives of h (the surface slopes, $\partial_x h$, $\partial_y h$). We will see next that a key ingredient to describe e.g. nanoripple formation is sensitivity to higher-order derivatives, e.g. related with the surface curvatures, such as $\partial_x^2 h$, etc.

5.1.2. The Bradley–Harper theory

The continuum model of the pattern-inducing effect of surface erosion by ion irradiation, that has set the paradigm in the field until very recently, was put forward 26 years ago in a seminal work by Bradley and Harper [19]. Following an earlier observation by Sigmund [20], these authors proposed a simple mechanism by which the local erosion rate at a point on the target surface depends primarily on the features of energy deposition in its surroundings. Mathematically, they proposed that the local normal velocity of erosion at any point **O** on the surface, $v_{\mathbf{O}}$, behaves as

$$v_{\mathbf{O}} \propto \int \Phi(\mathbf{r})\varepsilon(\mathbf{r})\, d^2\mathbf{r}, \tag{4}$$

where the integral extends to the solid. In Eq. (4), $\Phi(\mathbf{r})$ is the local ion flux given by the product of the homogeneous initial flux Φ_0 and the cosine of the angle between the beam direction and the local normal (as the consequence of the flux modification due to the local surface orientation), and $\varepsilon(\mathbf{r})$ is the local distribution of deposited energy. Following Sigmund's linear cascade approximation [125], $\varepsilon(\mathbf{r})$ is a Gaussian function, as depicted in Fig. 38. Conceptually, Eq. (4) is not far from the basic qualitative idea of the geometrical models mentioned above, in the sense that it posits the interface velocity to be proportional to the *local* erosion rate. However, by performing a Taylor expansion in which the average ion penetration depth was assumed much smaller than the surface radii of curvature, and exploiting the simplicity of

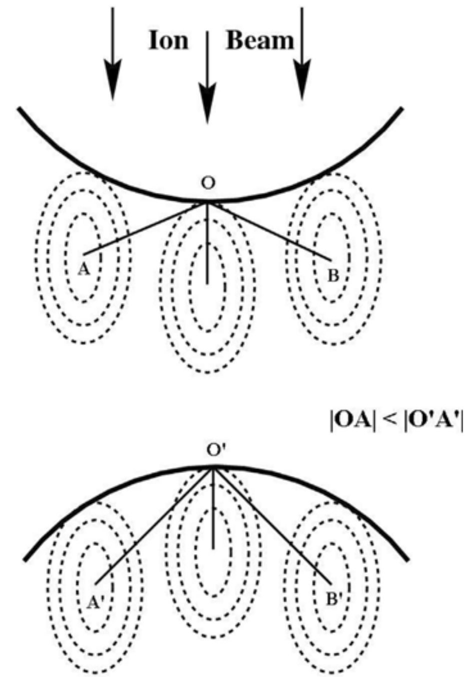

Fig. 38. Illustration of the energy deposition for two different surface profiles (solid lines), explaining the BH morphological instability. The deposited energy (thus, the erosion rate) at O is larger than at O' since, for example, the distance $|OA|$ is larger than the distance $|O'A'|$. Hence, valleys are eroded faster than peaks and height differences are amplified rather than smoothed out. Adapted with permission from [26]. Copyright 2002, Elsevier.

Sigmund's Gaussian, BH were now able to obtain a closed equation for the evolution of $h(x, y, t)$, as

$$\partial_t h = -\nu_0 + \gamma_x \partial_x h - \nu_x \partial_x^2 h - \nu_y \partial_y^2 h - B\nabla^4 h. \quad (5)$$

Here, ν_0 is the average erosion rate for a flat substrate and B is related to surface diffusivity [138], see below. An important aspect of the derivation of Eq. (5) in [19] is the fact that ν_0 and the remaining coefficients γ_x, ν_x, and ν_y, were explicitly related to the features of the Gaussian distribution $\varepsilon(\mathbf{r})$ (average ion energy, flux and penetration depth, and vertical and lateral spreads), ion energy, flux, and angle of incidence. Thus, Eq. (5) is remarkable, in part because of its simplicity, but also because it was able to predict a number of observed properties for ripple patterns, such as the ripple rotation when the angle of incidence is sufficiently high. Specifically, such a rotation was seen to occur in the model as a consequence of the fact that the sign of the curvature coefficients $\nu_{x,y}$ controls the emergence or absence of patterns. Thus, the surface will display a pattern along that direction, x or y, that features the largest *positive*[2] value of the corresponding ν_j coefficient, which turns out to depend on the value of the incidence angle in a way that agreed with a number of observations [2,3]. At normal incidence, $\nu_x = \nu_y > 0$ [19] and formation of a pattern is still expected, in which the x and y directions are equivalent. This is the so-called BH morphological instability. It becomes the mathematical expression of the physical fact that, within the present Sigmund approximation, the local sputtering yield is higher at a surface minimum than at a surface protrusion, as illustrated in Fig. 38. Thus, any initial differences in values of the height will be amplified by the sputtering process.

The BH theory has been an essential step in the modeling of IBS nanostructuring, and is still playing an important role. At the time it was put forward, one remarkable feature of this continuum model was that, as seen in experiments, it was able to predict formation of ripples whose wavelength (tens of nm) was substantially larger than the typical scale in the problem, that is, the average ion *penetration length* (typically a few nm). This was achieved through the introduction of the last term on the right-hand side (rhs) of Eq. (5), so that a smoothing mechanism dominates at small scales, controlling the behavior of the system. Physically, the choice of BH corresponds to thermal surface diffusion as classically described by Mullins [138]. In such a case, the coefficient B becomes proportional to parameters such as the surface diffusivity, that only depend on temperature in Mullins' derivation. In general, non-thermal processes, like irradiation itself, are also expected to influence surface diffusion [201].

The BH theory also provides predictions for a number of additional properties, like the dependencies with experimental parameters—such as the average ion energy and flux—of the ripple wavelength, or the velocity at which the pattern travels on the substrate plane as a whole. Roughly for 20 years after the publication of [19], a large number of experiments have been devoted to assessing the various BH predictions, with a varying degree of agreement, see detailed discussions in [2,3]. For instance, the BH model predicts a decrease of the ripple wavelength ℓ with increasing ion energy E. However, a number of experimental works report the opposite behavior (increasing ℓ with increasing E) for conspicuous materials, such as graphite or silicon [2,3]. Likewise, the in-plane transport velocity of the ripple pattern is predicted in the BH model to oppose the direction of the ion beam up to high angles of incidence, in contrast with experiments on e.g. glass [202], while agreeing with recent data on Si [74]. And we have already mentioned in the first sections the conflict between the BH prediction of pattern formation at any angle of incidence and the experimental existence of a threshold angle for ripple formation on Si.

At any rate, being linear in the height field h, the BH equation cannot possibly provide a full description of the dynamics, as it predicts exponential blow-up of the surface height with irradiation time. Physically, such a blow-up is not observed. Rather, at sufficiently long times the surfaces are usually seen to enter a steady state in which pattern properties, such as the roughness and wavelength, are seen to become time independent. Or else, they evolve further, but at a much moderate rate [2,3]. Mathematically, it is natural to expect non-linear terms in surface derivatives to become relevant, which are left out within the BH linear approximation. This motivated a number of different improvements of the theory which will be discussed next.

5.1.3. *Refinements of Bradley-Harper theory*

Further elaborations within the BH framework have been subsequently attempted, including both linear [46] and non-linear effects [24–26]. The former [46] include the proposition by Carter and Vishnyakov (CV) of an alternative mechanism to erosion that could account for the experimental results obtained by themselves on Si at 40 keV. Recall that in their experimental work [46] these authors observed no trace of pattern formation for small angles of incidence. Such observations contradicted the BH paradigm. Specifically, CV argued that the ion beam could transfer momentum to the target atoms. Within a coarse-grained description, this would amount to a net current of material being transported along the surface. The authors considered a one-dimensional surface and projected such a current onto the tangent line to the surface. Assuming no feedback between sputtering and this momentum-transfer mechanism, the latter would imply the addition of a term with the following form to the rhs of, say, a 1d version of Eq. (5):

$$+J\Omega f(E)\bar{d}\cos(2\theta)\partial_x^2 h. \quad (6)$$

Here, J is the average ion flux, Ω is the atomic volume of sputtered species, $f(E)$ is the number of recoils generated by each ion, and $\bar{d}$ is the characteristic distance for this momentum transfer. Notice that the net sign of the coefficient multiplying the $\partial_x^2 h$ curvature term is positive for small values of θ, corresponding to a morphologically stable term that would counteract the unstable erosive contributions. However, for $\theta > 45^\circ$ this contribution also becomes unstable, enhancing ripple formation. The 2d generalization of Eq. (6) has been noted in [203]. More recently, the early proposal by CV has received support from atomistic MD simulations for tetrahedral amorphous carbon [204] and amorphous Si and CuTi [205], and is being also reassessed numerically within binary-collision Monte Carlo descriptions [78,206]. Indeed, it is also playing an important conceptual role in the current reassessment on the true nature of the mechanism driving pattern formation by IBS as we will see below.

Another interesting attempt to improve the BH description has been discussed in [203,207,208], by incorporating the effects of stress into the linear interface equation. Here, a reduction in the strain energy of the surface is assumed to occur via changes in the surface morphology, as in the classic Asaro-Tiller-Grinfeld instability, well-known in the context of heteroepitaxial growth to lead to ripple formation [209]. We will reconsider this approach later in Section 5.3 from a different point of view.

Meanwhile, we can summarize the most salient features of further generalizations of the BH model [24–26], some of which are also found in more recent developments. The original motivations included, on the one hand, the need to identify non-linear effects which are able to tame the BH instability and drive the surface to a steady state. On the other hand, once fourth-order derivatives of h

[2] In contrast to curvature coefficients as defined in Fig. 36, in this section unstable curvature coefficients will be defined as positive.

are allowed into the evolution equation to describe surface transport as in Eq. (5), erosion should be described at a similar space resolution. Moreover, if this could introduce surface diffusion terms with a non-thermal origin, one might account for a number of experimental observations in which $\ell \sim E^p$ with $p > 0$, and ℓ is temperature-independent [2,3]. Carrying out the BH expansion also at the lowest non-linear order in h, the ensuing interface equation reads for normal incidence [24–26],

$$\partial_t h = -\nu\nabla^2 h - \mathcal{K}\nabla^4 h + \lambda(\nabla h)^2 + \xi. \tag{7}$$

Here, a noise term ξ is allowed in order to account for random fluctuations in the underlying atomistic processes, such as ion arrival, sputtering events, etc. However, the large-scale fluctuations developed by the deterministic ($\xi = 0$) equation itself [63] reduce the importance of such stochastic contributions. An important feature of Eq. (7) is the quadratic nonlinearity in the surface slope. Geometrically, it reflects the assumption that the surface moves locally along the local normal direction, as in the earlier geometrical models. Moreover, it implements the non-equilibrium nature of the erosion process [210]. With respect to the surface diffusion term in Eq. (7), it now features a modified coefficient $\mathcal{K} = B + D_{\text{eff}}$. This parameter collects an erosive contribution, D_{eff}, together with the previous Mullins'-type one, B. It has been shown recently [211,212] that the contribution D_{eff} is a spurious artifact due to the truncated expansion in the height derivatives, see also below. Nevertheless, the form of the modified term already anticipates the result of more correct formulations, in which non-trivial interaction occurs between erosive mechanisms and surface transport.

In the context of Non-linear Science, Eq. (7) is known as the (stochastic) Kuramoto-Sivashinsky (KS) equation. It is a paradigm for chaotic spatially extended systems [63]. Actually, the large-scale behavior of the stochastic and of the deterministic equations are statistically equivalent. The various anisotropic versions of it, derived in [24–26], include the "minimal model" [24]

$$\partial_t h = \gamma\partial_x h - \nu_x\partial_x^2 h - \nu_y\partial_y^2 h + \lambda_x(\partial_x h)^2 + \lambda_y(\partial_y h)^2 - \mathcal{K}\nabla^4 h + \xi, \tag{8}$$

which is the one most frequently described in the literature as the anisotropic Kuramoto-Sivashinsky (aKS) equation. The main feature of the dynamics described by the (a)KS equation consists in an initial (BH) morphological instability in which a preferred (dot or ripple) wavelength is selected. This regime corresponds to exponential growth of e.g. the surface roughness. After this transient time, the surface amplitude stabilizes, entering a second regime in which the pattern evolves in a highly nonlinear fashion, becoming disordered both in plane and in the growth direction, with fluctuations that display kinetic roughening properties [213]. The latter type of interfacial behavior is associated with so-called universal behavior, whereby systems which differ strongly in physical nature can nonetheless be described by a common large-scale equation. This fact may be behind the relevance of a model like Eq. (8) to the observed evolution of some IBS nanoripple patterns [214]. In particular, the aKS equation has been recently shown [82,83] to be a promising model to account for the rotation of the ripple pattern with increasing fluence, which has been experimentally observed on Si targets at elevated temperature [79,80] and was discussed in Section 3.1. It has also been used to rationalize experiments of Kr^+ irradiation of Si at $\theta = 63^\circ$ [70]. Another successful application of the nonlinear generalization of the BH equation occurs in a case in which, rather than assuming a small-slope expansion as in Eqs. (7) and (8), arbitrary values of the slope are allowed for [215–217]. This has been shown to provide a good description for the propagation of high steps or ridges on Si targets [215,216], even leading to a fabrication method for patterns made of knife-edge ridges [217].

Still, the technologically interesting case in which *well ordered* dots or ripples form, remains far from description by the KS equation. Thus, various attempts have been made at improved descriptions through further generalizations of the KS equation. We can mention the damped KS equation, in with a linear term of the form $-\alpha h$ is added to the rhs of Eq. (7) [218]. This additional term is well known in the Pattern Formation context [63] to readily allow for improved ordering of the cellular structure (dots) for appropriate parameter conditions. However, although it has been argued to be related to re-deposition effects, to date there is no unambiguous physical interpretation of the damping parameter α, see e.g. [219] and references therein. Moreover, re-deposition has been recently argued to be an inherently non-linear effect [220]. In this connection, also recently Diddens and Linz have combined a non-local model for particle re-deposition with the KS equation using a sophisticated numerical integration model, to show that re-deposition can stabilize and form well-ordered dot structures for a certain range of parameters in their model [221,222].

Another possibility to go beyond the KS equation is to carry out the BH-type expansion to still a higher non-linear order, as indeed was done in [223], obtaining an interface equation that for normal incidence reads

$$\partial_t h = -\nu\nabla^2 h - \mathcal{K}\nabla^4 h + \zeta^{(1)}(\nabla h)^2 + \zeta^{(2)}\nabla^2(\nabla h)^2 + \xi. \tag{9}$$

Unfortunately, coefficients $\zeta^{(1,2)}$ take the same sign as functions of phenomenological parameters, so that there is a cancellation mode in Eq. (9) [224,225]. This means that the $h_{k_{\text{canc}}}(t)$ Fourier mode of the height which corresponds to wave-vector value $k = k_{\text{canc}} = (\zeta^{(1)}/\zeta^{(2)})^{1/2}$ is linearly unstable; moreover, nonlinear terms cancel each other *exactly* for its equation of motion, so that its amplitude blows up exponentially, as a result of which the continuum description breaks down.

In summary, higher-order linear and non-linear refinements of the original BH equation not only may be of a limited physical applicability, but are also affected by issues on mathematical consistency. Note that probably this is not necessarily due to the approximations involved in Sigmund's Gaussian description of energy deposition: As seen for exponential [226] as well as for more general [203] energy deposition functions, the main qualitative pattern-forming properties are essentially unchanged as compared with those induced by Gaussian decay. Actually, as has been recently discussed, [212,211], formula (4) relating the local surface velocity with collisional energy deposition is morphologically unstable at all length scales. Thus, mathematical features associated with its various linear and non-linear truncations, such as negative values of D_{eff} [25,26], or cancellation modes [223], are probably nothing else than manifestations of this physical fact. All this indicates the need for a description that improves the present models, both from the physical and from the mathematical points of view.

5.2. Two-field models of IBS nanopatterning

5.2.1. Two-field models for single-component systems

In order to improve upon the physical and mathematical limitations of the continuum models just described, an observation by Aste and Valbusa [227] brought back the attention to the analogy with macroscopic pattern formation. Such an analogy had been a suggestive one ever since the earliest reports on ripple formation by IBS [16]. The idea is that Aeolian and underwater sand ripples can be successfully described (see [228] for a review) by explicitly coupling the dynamics of the height with that of the density of species subject to transport at the surface. Thus, one

needs to describe in more detail the near-surface region in order to properly account for the system dynamics. Incidentally, in the more closely related Nanoscience context of growth of strained binary alloy films, analogous two-field models have also proved quite successful since the beginning of the 2000s [229]. In this case, the interface dynamics is coupled, rather, to the concentration field of one of the elements of the alloy. The coupling to the concentration of the other element occurs then implicitly through mass conservation. We first focus on the case of monoelemental targets, which allows to introduce the main ideas in a more direct way, and will consider the case of compound targets (or else irradiation in the presence of impurities) in the next section.

As discussed above, the formation of a thin amorphous layer on top of a crystalline bulk on semiconductors under IBS is well documented [12], see for example Fig. 13. For Si, typical MD results indicate [127] a stationary thickness of 2–3 nm for 500 eV Ar^{+} irradiation, that is readily achieved for a fluence of 4×10^{14} ions/cm^2. With a sputtering yield that stabilizes at around 0.45 atoms/ion, this implies that, during the non-trivial evolution of the morphology, the ion beam mostly amorphizes the solid while maintaining a stationary amorphous layer. Most atoms that are eroded from the crystalline bulk remain at the surface, provided the amorphous layer is so thin that it can be loosely identified with the surface itself. Actually, the idea of a thin surface layer that is subject to ion-induced viscous flow had allowed Umbach and coworkers [141] to improve their description of the temperature dependence of the ripple wavelength for experiments on irradiation of silica, and to account for their observation of a ripple wavelength which increases with ion energy.

Capitalizing on these ideas, a "hydrodynamic" approach has been developed for the cases of normal [28,230] and oblique incidence [231,232]. Note that this is not a full implementation of the Navier–Stokes equations, see in contrast Section 5.3. The general structure of these models is that of a reaction-diffusion system,

$$\partial_t h = -\Gamma_{\text{ex}} + \Gamma_{\text{ad}}, \tag{10}$$

$$\partial_t R = (1-\phi)\Gamma_{\text{ex}} - \Gamma_{\text{ad}} + D\nabla^2 R, \tag{11}$$

where h is the surface height and R is the density of species that are subject to (diffusive) transport within the amorphous layer. In Eqs. (10) and (11), Γ_{ex} (Γ_{ad}) are rates of excavation (addition) from (to) the crystalline bulk, which depend on h, R, and their derivatives, and parameter ϕ controls the amount of actual sputtering. The idea is that removal of material locally decreases the value of h and increases that of R, and it is the latter that is transported with diffusivity D. While (10) and (11) are statements on conservation of matter, proper constitutive laws are required that relate the rates $\Gamma_{\text{ex},ad}$ to the physical fields, h and R themselves. A natural choice for Γ_{ex} is to consider the BH-type statements on the local erosion velocity from Eqs. (5) and (7), inheriting some of their limitations as discussed above. On the other hand, the addition rate Γ_{ad} was chosen to reproduce Mullins' surface diffusion in the absence of irradiation.

In principle, predictions on the surface dynamics can be already obtained from the full system of coupled equations (10) and (11). For instance, one can perform a linear stability analysis of periodic perturbations around a flat solution. This provides the dependencies on phenomenological parameters for e.g. the ripple wavelength and the velocity of in-plane ripple transport [232,230]. Very recently, such predictions have been argued to successfully account for ripple propagation on glass surfaces, as induced by FIB irradiation with 30 keV Ga^{+} ions [233]. A different simplification of the continuum model can be achieved by exploiting the fact that the time scale associated to erosion is much faster than the diffusive characteristic time. This implies that the R field evolves in a much shorter time scale than the height, so that a single closed equation for h can be obtained to lowest nonlinear order in a power expansion. For normal incidence ($\theta = 0$), this reads [28]

$$\partial_t h = -\nu\nabla^2 h - \mathcal{K}\nabla^4 h + \lambda^{(1)}(\nabla h)^2 - \lambda^{(2)}\nabla^2(\nabla h)^2, \tag{12}$$

see [231,232] for oblique incidence. As in previous models, coefficients appearing in Eq. (12) are functions of the phenomenological parameters characterizing e.g. Sigmund's Gaussian, and actually couple the various concurrent mechanisms in a natural way. Two improvements over previous models are thus achieved: On the one hand, although Eq. (12) has the exact same form as Eq. (9), thanks to the sign of second non-linear term on the rhs, it can become free of cancellation modes [28]. On the other hand, sputtering couples in a natural way to material transport, so that nonthermal contributions to $\mathcal{K}\nabla^4 h$ occur, which are induced by erosion [232]. This circumvents the need to introduce high (fourth) order terms in the description of the surface geometry, as in [25,26]. Actually, the term with coefficient $\lambda^{(2)}$ in Eq. (12) implements the effect of such a coupling between erosion and surface transport at the lowest nonlinear order.

As discussed in [28,230], Eq. (12) leads to a nanodot pattern with short-range order, whose typical wavelength coarsens at intermediate times [234]. In spite of the fact that this model has been derived for a mono-elemental substrate in absence of contamination, it seems to describe the full morphological evolution of ordered dots obtained in the presence of impurities [103]. This is illustrated in Fig. 18, where experimental data on Ar-irradiation of Si under such type of conditions are shown, together with predictions from Eq. (12), for different values of the ion flux. Agreement ensues irrespective of the structure (crystalline vs amorphous) of the starting target [105], and can be established thanks to the fact that Eq. (12) depends only on four parameters, which one can fix in the experiment by making the same number of independent observations. Namely, the time for instability onset, the ripple wavelengths within linear stage and after coarsening interruption, and the ripple amplitude at long times, for all of which approximate theoretical predictions exist which are given in terms of the parameters in Eq. (12) [230]. In order to see how such an agreement can be obtained, note that continuum equations of the type we are describing apply to the large-scale behavior of the system. As mentioned above, in this limit a great deal of universality frequently occurs [235,195,63]. This means that systems that differ in their microscopic nature may nevertheless display the same large-scale properties. Actually, Eq. (12) has been also derived as a model for the interface dynamics that ensues in very diverse systems, from growth of amorphous thin films at nanometric scales [236,237] to macroscopic patterns on snow fields [238]. An additional proof of the universality of Eq. (12) within the IBS context has been recently provided in Ref. [239], where the system fluctuations in the saturated regime are compared with those predicted by the damped KS equation (see Section 5.1.2) [218]. In contrast to the latter, the numerical integration of Eq. (12) shows that the temporal correlation of the structures increases with time when the roughness has essentially saturated, dynamics becoming progressively slower. This slowing down is known as ageing, a phenomenon which occurs in many processes far from equilibrium. For IBS systems, it has been experimentally demonstrated in the case of GaSb targets [240].

The two-field approach just described makes a number of physical simplifications and thus has important limitations. For instance, one of such simplifications is to consider that the "re-deposition" parameter ϕ is constant, since the fraction of eroded material which is eventually sputtered probably depends on the

local surface morphology. An even more drastic one concerns motion of the target atoms: One might expect it not to be random, since incident ions apply some directional force in the mobile layer. This force is a key ingredient to understand e.g. why silicon remains flat under IBS for normal incidence, as will be discussed in Section 5.3, and it is not considered in this model. Still, CV-type effects which introduce a non-zero value of θ_c can be incorporated in a phenomenological way into Eqs. (10) and (11), see e.g. [28]. With respect to describing a directed motion by the isotropic diffusion term $D\nabla^2 R$ in Eq. (11), one could argue on the basis of simplicity combined with a correct effective behavior: Such a term leads to an effective description of surface-confined viscous flow [140] since, coupled with sputtering, it contributes to the fourth-order derivative term in the effective equation (12). Nevertheless, more solid justification is highly desirable. Overall, it seems that a description of IBS of silicon targets needs to account for the dynamics of the amorphous layer in a still more detailed way; recent proposals are discussed below. In contrast, the present two-field approach is probably better suited to e.g. metallic materials under erosive conditions [23], in which the substrate remains crystalline and the mobile material is more correctly described by diffusive adatom currents, than by flow of an amorphous material. For successful applications of Eq. (12) to describe experiments on “nanobead” formation on pre-patterned gold targets, see e.g. [241,242].

5.2.2. Two-field composition models

Binary materials. In the two-field approach introduced above, the role of contaminants is not taken into account, nor is the fact that many irradiated materials are compounds containing initially well-mixed species, which in particular may sputter at different rates. Thus, both from the theoretical and from the practical points of view it would be interesting to develop models that explicitly address compositional heterogeneity in the species involved in the sputtering process. In view of the versatility of two-field descriptions for IBS and for *growth* of binary alloy films [229], in 2007 Shenoy, Chan, and Chason [40] put forward a model for IBS of a binary compound with two atomic species, A and B, in which the dynamics of the surface height h was now coupled with that of the fluctuation in composition, ζ, around the local equilibrium for one of the species, say, A. It reads

$$\Delta\partial_t\zeta = \Omega[(c_b - 1)(\delta F_A + \nabla\cdot\mathbf{J}_A) + c_b(\delta F_B + \nabla\cdot\mathbf{J}_B)], \tag{13}$$

$$\partial_t h = -\Omega[\delta F_A + \delta F_B + \nabla\cdot\mathbf{J}_A + \nabla\cdot\mathbf{J}_B], \tag{14}$$

where c_b is the stoichiometric surface composition in A species, Δ is the thickness of the surface layer that features such composition on average, and δF_i are the changes in the flux of sputtered i-atoms (with $i = A$ or B), that depend on the corresponding yields and on the local sputtering velocity, which is assumed to be given by the BH approximation made for Eq. (5). On the other hand, $\mathbf{J}_i$ represents the diffusive mass current of i species, that incorporates both a standard Fickian term akin to that in (11), and thermal surface diffusion [40].

The two-field system (13) and (14) predicts that, concurrent with the ensuing morphological BH-type instability, the differences in diffusivities and sputtering yields between the two species induce a spontaneous modulation of the composition, that can be in- or out-of-phase with the ripple topography. The results in [40] were obtained only within the linear approximation. A more complete study including non-linear effects was provided by Bradley and Shipman [243,244]. Their model [245] can account for nanodot and nanohole pattern formation, qualitatively of the type discussed in Section 3.2, see e.g. Fig. 21(b). In Fig. 39 we can see the topography and composition of ordered hexagonal and roll patterns predicted by this model for two different parameter sets at two different times. Note the high degree of spatial in-plane order of the structures.

Recall that, as discussed in Section 3, under pattern formation conditions for e.g. monoelemental Si, the growth rate of periodic perturbations $\omega_{\mathbf{q}}$ has a band of unstable modes that extends from $\mathbf{q} = \mathbf{0}$ to $\mathbf{q} = \mathbf{q}_0$ such that $|\mathbf{q}_0| > |q_*|$, with $\mathbf{q}_*$ the wave-vector associated with the ripple structure. This property is actually shared by all the continuum models discussed in Sections 5.1 and 5.2.1, with the exception of the damped KS equation. As is well established in the theory of Pattern Formation [63], this implies that the ensuing pattern can have at most short-range order. In contrast, in the theoretical works by Bradley and Shipman, a CV mechanism is incorporated in the diffusive currents $\mathbf{J}_i$. Such a mechanism induces the existence of a narrow band of unstable height modes, namely, the only unstable periodic perturbations which have a positive value of $\omega_{\mathbf{q}}$ have wave-vectors in a finite range $|\mathbf{q}| \in [q_1, q_2]$, with $q_1 \neq 0$. This is known [63] to imply an improved in-plane ordering of the ensuing patterns, and is the case for many parameter choices in [243,244]. This is a first physical proposal for a description of such a remarkable property of many experimental systems [3]. Nevertheless, the assumed origin for the necessary morphological instability is still the BH mechanism, which does not seem likely for mono-elemental targets at small incidence angles, as we have seen above. Likewise, MD simulations employing crater functions seem to question the numerical importance of the BH mechanism under such conditions, as shown in [133] and [246] for Ar-irradiated Si and GaSb, respectively. In these works, the parameters controlling the sputtering and the preferential redistributions are estimated and do not satisfy the requirements to induce the ordered pattern formation obtained in the Bradley and Shipman’s models. Still, as discussed above the numerical accuracy of crater functions has been recently questioned. We can still note a result by Bradley [247], who has shown that in a model related to those in [243–245], but in which the curvature dependence of the sputtering yield and thermal surface diffusion are both suppressed, still an instability occurs, due to amplification of sputter yield differences. However, the order of the pattern is expected to be short-ranged in such a case. On the other hand, a generalization of the latter models has been proposed in [248], which includes the effect of ion-assisted phase separation. Even when the BH instability, preferential redistribution, and chemical diffusion are absent, the resulting model has a narrow-band instability that can explain the order of observed patterns. This work also provides a characteristic signature that may be employed to distinguish whether the origin of the instability is chemical or morphological.

While the models studied in [243–245] are for normal-incidence bombardment, their generalization to oblique incidence has been reported in [249]. The conclusion of this work is that virtually defect-free ripples can be produced by ion bombardment of a binary material if the ion species, energy and angle of incidence are appropriately chosen. Experimental studies are available on defect elimination from pre-formed ripples on mono-elemental Si by so-called sequential IBS [250]. Specifically, ripples are first produced by irradiation at 67°. Once formed, the target is rotated by 90° and further irradiated at 85° incidence. The result is a high-quality rippled surface with few defects. The process is qualitatively described by the damped KS equation, which, akin to the models studied in [243–245,249], features a narrow band of unstable Fourier modes. Nevertheless, the whole process differs from the result in [249], which in principle predicts high-quality ripple formation in a single-step IBS treatment for a binary target.

An important prediction from [243,244] is that composition segregation will lead the high-yield species to remain at the top of the structures produced, as has been reported for experiments on

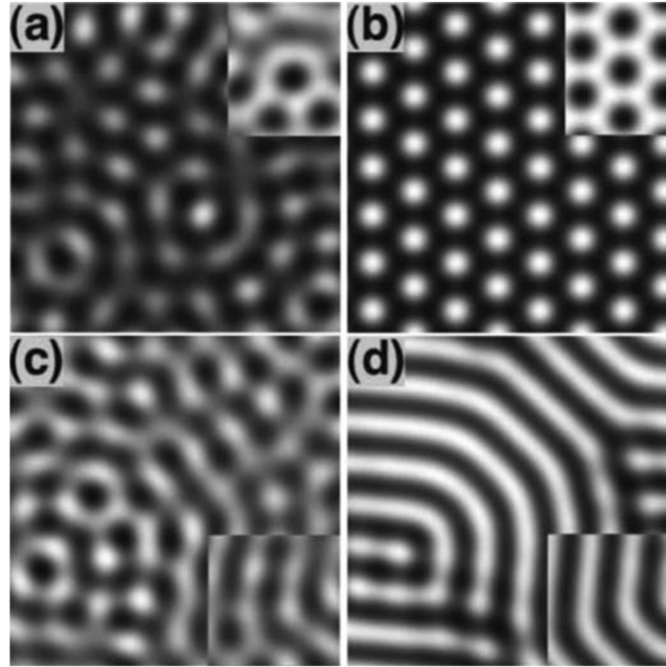

Fig. 39. Plots of the rescaled surface height (main panels) and composition (insets) for two different sets of parameter values (first and second rows) at two different times (first and second columns). Reprinted with permission from [243]. Copyright 2010, American Physical Society.

GaSb dot formation, in which ripple peaks are reported to be Sb-rich [51]. This is a consequence of the fact that, due to the BH instability, ripple troughs are eroded more efficiently, and therefore they become depleted in that species that sputters faster. However, this is in contrast with observations of GaSb cone formation in [96] and [251]. In these experimental and theoretical works, the origin of the instability is claimed to lie with phase separation, whereby Ga droplets form and shield the underneath substrate due to their reduced sputtering yield, leading to cone formation.

These unconclusive results can serve to illustrate the current status of development in the field, and stress the need for further experimental and theoretical studies that allow for a full clarification of the mechanisms that are driving the morphological and compositional patterning in the case of compound targets. Systematic work, such as that presented in Section 3.2 of this review, seems instrumental as a basis for the development of a consistent understanding of the topic. Concurrently with such type of developments, applications of the tools and ideas developed in this context will undoubtedly develop in related problems and fields, suggesting potential new phenomena. As recent examples we can mention the possibility of long-lived temporal oscillations of the sputtering yield for e.g. ternary alloys [252], or that of compositional banding at the nanoscale for ion-beam assisted *deposition* of binary thin films [253,254].

Monoelemental materials with surfactant co-deposition. A context which is closely related to the case of binary materials is that of a mono-elemental target that is undergoing IBS in the presence of (intentional or accidental) contaminants of a different species. For the case of Si, it has been extensively considered in Section 3.2 from the experimental point of view. With respect to continuum descriptions of this class of experiments, an initial proposal was put forward in [255], in the context of so-called surfactant co-deposition. It takes the form of a two-field system, in which the evolution of the impurity (surfactant) density is coupled with that of the local velocity of the eroding surface. The surfactant species are in general assumed to have a sputtering yield that differs from that of the target atoms. Results of Monte Carlo-type models (see [256,257] for reviews) in the presence of surfactants were then rationalized in the framework of numerical simulations of the continuum model. All these simulations already hinted at the existence of interesting patterns and a non-trivial modulation of the chemical composition at the surface. However, the continuum model was not analyzed in further detail.

In the wake of the recent theoretical progress made for the case of binary targets, a number of additional proposals have appeared more recently in the literature, which address this situation [124,258–260]. All of these are two-field models in which the dynamics of height and composition are coupled in a form which is closely related to the models just described for compound targets. For instance, in [124] a numerical study is provided on the linear stability properties of a model in which CV-type relocation mechanisms, tensile stress, and surface-confined viscous flow are taken into account. Both the ion and the impurities are assumed to impinge at normal incidence, and a BH-like unstable dependence of the sputtering yield with curvature occurs. An assumption is made on a sharp interface separating the surface layer with altered composition from the unsputtered target. Moreover, Fickian diffusion of the mobile species through such a layer is neglected. This mechanism is akin to the surface transport defined in the earlier two-field models for mono-elemental targets seen in Section 5.2.1. As discussed there, such a mechanism reflects in the effective evolution equation for the height with the form of surface-confined viscous flow, hence these two physical mechanisms have to be considered in a consistent way. The strong approximations in [124] are later relaxed in [258]. Moreover, analytical results are now provided within the linear regime of the evolution. In the latter work, it is assumed that, once deposited, impurities become immobilized due to e.g. silicide formation of the type discussed in Section 3.2. Then it is predicted that, for an impurity concentration above a certain threshold, the assumed CV mechanism is deactivated due to such immobilization, and pattern formation ensues. Qualitatively, the existence of such a threshold agrees with many experimental observations, see Section 3.2. In [259], a way of generalization of [258] to the case of off-normal

impurity co-deposition is put forward, although surface viscous flow is assumed, rather than thermal surface diffusion as in the latter. Moreover, both the CV and the BH mechanisms are neglected in order to elucidate a morphological instability that arises as a consequence of differential sputtering rates between impurities and target atoms, in interplay with a phase shift between the concentration and the height profiles. However, in the case of the Fe/Si system the erosion rate of iron is higher than in silicon, and this represents a limitation of the previous models. Such a limitation has been overcome in a recent work by Bradley [260] for the case of obliquely deposited impurities and when the target atoms and impurities can react to produce a compound. In this work he studies the ripple formation and movement emerging purely from the interaction between the topography and the surface composition. As an important consequence for the case of silicon, the conclusion from [260] is that silicide formation is required for ripple formation.

In general, note that, although the models discussed in this section are important steps forward in our understanding of the case for non pure mono-elemental targets, they have a number of features that require further reflection and development. For instance, at times they are combining different mechanisms independently, such as BH erosive contributions and CV restructuring, while physically such mechanisms should be somehow related with each other, since they are both of a common collisional origin. Moreover, not always is the non-trivial angle dependence of the CV mechanism taken into account. Furthermore, in many cases the origin of the instability needs to be traced back to the BH mechanism. However, as discussed in Section 3.1, at least up to relatively high incidence angles such a process does not seem to be operative for materials like Si in the absence of contamination. Technically, in some cases results have been obtained only for a particular geometry, while most predictions are confined to the linear stage of the surface evolution. These facts indicate room for further development of the theoretical description of IBS nanopatterning, also in the cases of compound targets or of impurity co-deposition. Still, and in parallel with the situation for monoelemental targets, new and promising connections with related systems are appearing. For instance, use of metallic atoms as ions, rather than as impurities, can lead to interesting and novel patterns. Thus, irradiations with Au^- ions at energies around 20 keV and at an incidence angle of 60° lead to a ripple pattern with a remarkable degree of order on Ge, and to a novel structure with ripple patches at oblique orientations, for the case of Si targets [261]. Notably, a two-field theory for these ion-implanted systems can be developed, which is inspired by those available for IBS with concurrent deposition of impurities. Qualitative agreement with experiments is achieved [261].

5.3. Stress-driven hydrodynamics of irradiated silicon targets

In face of the new experimental data in which spurious effects due to contaminants in silicon irradiation are explicitly avoided, see Section 3.1, the basic ingredients that are required in the continuum description of IBS surface nanopatterns have been recently reconsidered [262,58,196,263–265,193]. The goal is to account within a single framework for, at least, the most salient features of the recent experimental picture of the process. We have seen in the previous sections that the near-surface layer seems to play a crucial role in the dynamics of the system, both in the single and multicomponent cases. Hence, a natural choice is to focus on its evolution and leave morphological dynamics to arise, rather, as a byproduct of the physical phenomena that are taking place there. For the case of clean amorphous or amorphizable targets, the dynamics of this layer (with a thickness of the order of the ion penetration depth [141]) is studied through a hydrodynamical description using full Navier–Stokes equations [58,196,263–265]. In principle, this description should retrieve results for thin layers, so that some connection with other models, like those discussed e.g. in Section 5.2.1, is expected in appropriate parameter ranges. Actually, previous experimental [266,267] and theoretical [202,268] approaches to the IBS problem through the effects of viscous flow are available, although no general description of the process had been thus achieved so far. For example, in [202] Alkemade postulated that viscous flows does occur in a thin layer with variable stress, and employed a Navier–Stokes formulation for flow on a undulating substrate, combined with a BH-type behavior for the sputtering yield. In this way he was able to estimate a value for the radiation-induced viscosity and the ripple velocity which, in contrast to BH theory and in agreement with his own experiments in SiO_2, is in the direction of the ion beam projection. This model has some limitations. For instance, the flow has only a stabilizing effect and the instability has a purely erosive origin. Moreover, collisional processes are accounted for within a thermal-spike picture, which has been questioned for the energy range considered, see e.g. [269].

In order to provide a proper description for the viscous flow behavior, the conservation and constitutive laws that apply in the system should be specified. Note that any fully hydrodynamical approach has to rely on the fact that the present type of material flow is highly viscous, so that actually Stokes flow applies. Indeed, viscosity of the amorphized layer is in the 10^8 Pa s range [139], so that the Reynolds number is much smaller than 1. The simplest mathematical models that account for viscosity are Newtonian fluids. In [58,196,263] the flowing layer is considered to be Newtonian and incompressible, and of a stationary thickness R_0. This is achieved by setting the erosion rate at the free interface equal to the erosion rate at the amorphous/crystalline (a/c) interface. As additional boundary conditions, surface tension is assumed to act at the free interface, and a no-slip condition is taken at the amorphous-crystalline interface. The effect of the ion beam is then incorporated in two complementary ways:

- as introduced in [262,196,263], it can be implemented through a body force acting in the bulk of the fluid, taking into account the local variation of the ion flux on an undulated free surface. Typically, it can be written as an amplitude of the force, f_E, times an angular dependence which is assumed $\cos(\theta)$ for geometrical reasons;
- or else, as a uniform stress whose effect is only reflected on the surface of the material [263,264].

Both formulations are equivalent in the limit in which the thickness of the amorphous layer is much smaller that the ripple wavelength. Hence, for definiteness here we discuss the case of a body force. Such a mechanism is reminiscent of that of CV [46], but is crucially not restricted to act *along* the surface but is present, rather, in the *bulk* of the flowing layer. The coefficient f_E mediating this mechanism has units of a stress gradient, and its value can be estimated [262] from experiments [37–39,41] and MD simulations [130], agreeing with morphological data on Si and being 0.42 kg/(nm^2 s^2). Notice, flow of the amorphous layer is here actually a relaxation mechanism, which implements the reaction of the system to the external driving imposed by the ion beam. With a view to understand the physics behind the critical angle for ripple formation, we neglect for simplicity sputtering effects, and consider [262,263,58] that the main driving force is the stress that sets throughout the amorphous layer as a consequence of the ion-induced damage produced by the collision cascades. In order to assess this effect, one can consider its dependence on e.g. the average ion energy, E [58]. Thus, if one simply considers the volumetric strain produced by atom displacements from their equilibrium positions, a certain scaling law results

[270]. Corrections to it taking into account defect relaxation [271,269] lead to $f_E \sim E^{-7/6-2m}$, where $m \in [1/3, 1/2]$ [58].

The fluid dynamics with which the amorphous layer has been endowed has an effect on the shape of the free boundary. In order to assess this, one typically considers a flat interface and studies its linear stability with respect to periodic modulation of wave-vector q, finding that perturbations evolve with an amplitude proportional to $\exp(\omega_q t)$, where [262,196,263]

$$Re(\omega_q) = -\frac{[f_E \cos 2\theta + q^2\gamma][-2R_0 q + \sinh(2R_0 q)]}{2q\eta[1 + 2R_0^2 q^2 + \cosh(2R_0 q)]} + Re(\overline{\omega}_q). \quad (15)$$

Here, η is the ion-induced viscosity, γ is surface tension, and $\overline{\omega}_q$ is the contribution by purely erosive mechanisms to the dispersion relation, that will be henceforth neglected. Eq. (15) shows that, in this hydrodynamic formulation, ion-driving and material relaxation couple in a natural, albeit non-trivial, way which generalizes known results. Thus, in the absence of the beam ($f_E = 0$), Eq. (15) reduces to the classic result by Orchard [140] on the rate of smoothing for the free surface of a fluid layer of arbitrary thickness. Actually, it corresponds to Mullins' [138] rate of surface relaxation by bulk viscous flow, employed in [266,267] to account for experimental results on smoothing of silica targets. In contrast to the previous result, which holds in the thick film limit, in the case of a thin layer ($R_0 k \ll 1$) Eq. (15) reduces to [262,196,263,58]

$$Re(\omega_q) = -\frac{f_E R_0^3 \cos(2\theta)}{3\mu} q^2 - \frac{\gamma R_0^3}{3\mu} q^4 + Re(\overline{\omega}_q), \quad (16)$$

where the first term on the rhs has the same form, including the angle dependence, as the CV contribution Eq. (6), which is obtained by assuming that f_E is proportional to $\cos(\theta)$. In turn, the second term on the rhs of Eq. (16) precisely corresponds to surface-confined viscous flow [140], as employed by Umbach and coworkers [141] to account for the ripple wavelength dependence on temperature and ion energy, for experiments on silica targets. Recall here that there exist alternative forms [203,207,208] to incorporate stress as the mechanism which drives surface relaxation in IBS systems, as in the classic Asaro-Tiller-Grinfeld instability ubiquitous in heteroepitaxial growth [209]. However, the ensuing form of the linear dispersion relation as a function of $|q|$ differs with respect to the polynomial form (16). The recent direct measurements of $Re(\omega_q)$ by x-ray diffraction [59] for Si irradiation actually seem to agree rather with the latter.

Further detailed analysis of Eq. (15) in which one neglects the erosive contribution $\overline{\omega}_q$, leads to the conclusion [196,263,262,58] that it predicts a morphological transition at an energy independent angle $\theta_c^{\text{theo}} = 45°$, with the same features as in the experiment [37–39,58]. Namely, flat surfaces occur for $\theta < \theta_c^{\text{theo}}$ while ripple pattern formation takes place for $\theta > \theta_c^{\text{theo}}$. This result compares quite favorably e.g. with the experiments on Si targets shown in Fig. 3 in Section 3.1. Moreover, close to the transition angle, the ripple wavelength under pattern forming conditions behaves as $\ell = 2\pi[\gamma/(f_E \cos 2\theta)]^{1/2}$. Again, this behavior compares well with experiments on Si, as shown in Fig. 6, in which the solid line provides the theoretical prediction, and symbols are experimental data. Further support to the hydrodynamic description comes from the energy dependence of the ripple wavelength. Thus, considering the discussion above on f_E, one obtains [58] $\ell \sim E^{0.92} - E^{1.08}$, roughly a linear dependence, as obtained in the experiments reported in Fig. 9. As discussed above, this behavior contrasts with predictions based on the BH theory [2,3], and had motivated a number of earlier refinements of this model. Moreover, for Ar^+ irradiation at low to medium ion energies, a ripple wavelength that is roughly proportional to ion energy has been also reported for surfaces other than Si, such as SiO_2 [141], graphite [272], and amorphous carbon [78]. Thus, this type of energy dependence may in the end be the norm, rather than the exception as was widely believed until recently [2,3].

The viscous flow description we are discussing provides additional predictions on the morphological features during the linear regime. Such predictions can be employed in order to perform a self-consistent study of this regime. Thus, given the ensuing exponential rate of growth of height perturbations, see Fig. 5, one can define a typical time-scale associated with the growth rate of the fastest unstable Fourier mode of the surface, namely, the one associated with the ripple structure [58], $\tau \sim E^{7/3-2m}/[J\cos^2(2\theta)]$. This is the shortest time scale associated with linear evolution, thus it is a safe estimate on the duration of the linear regime for any pair of experimental values (θ, E). Hence, knowing its value for a reference experimental condition $(\theta_{\text{ref}}, E_{\text{ref}})$, it can be extrapolated for a different choice by rescaling through the previous formula. Thus, one can guarantee that experiments for, say, different values of the angle of incidence and/or ion energy, are within the same linear regime, provided they are performed for the value of irradiation time prescribed by τ for the chosen (θ, E) pair. Fig. 6 corresponds to the choice [58], $\theta_{\text{ref}} = 55°$ and $E_{\text{ref}} = 700$ eV. Consequently, from τ we can extract the experimental times for different angles or energies, which we define as an intrinsic timescale, namely, the time at which all the experiments are capturing the same linear regime. An example of this use is provided in Fig. 6. The data shown as bullets correspond to measurements of the roughness at times that relate to one another through τ. Indeed, now all values of the roughness [panel (a)] are quite similar, an indication that the system is at a comparable stage of development of the linear regime for the corresponding experimental conditions. Measurements plotted in panel (b) and in Fig. 9 have been performed through a similar procedure.

Within a continuum approach, the viscous flow approach provides a natural link between an external forcing exerted through events that occur at the picosecond time scale, and non-trivial surface dynamics unfolding in macroscopic time scales. Moreover, the assumption on irradiation-induced damage (stress), as the main physical mechanism driving the surface dynamics leads to an improved theoretical description in agreement with a number of experimental reports [58]. Such a residual stress results as the interplay between atom-displacement and partial relaxation through defect migration and sputtering. Another benefit from these results is the systematic exploration of the linear regime for different experimental conditions for which it has a different duration. At this, one needs to identify the proper parameter dependence of the relevant time scale. Overall, these results modify the interpretation of the morphological instability in IBS nanopatterning of mono-elemental semiconducting targets. Rather than being purely "erosive" and originating a curvature-dependent sputtering yield, the instability sets in due to the different exposure to the ion beam of the different regions in the amorphous layer. These local differences imply a larger driving for regions that are more directly exposed to the beam, while dynamics are relatively hampered in regions that receive a reduced flux. For incidence angles above the threshold value, incompressibility of the layer makes the fluid "bulge" out, leading to pattern formation.

Additional continuum models of IBS have been reported recently in which stress and/or viscous flow play important roles. For instance, in [265] a linear stability analysis is provided for a model in which the ions are proposed to impart a biaxial compressive stress to the amorphous layer. In turn, this phase relaxes as a linear Maxwellian viscoelastic film. Interestingly, this mechanism of stress generation turns out to be unconditionally stabilizing. This questions previous hypothesis on elastic stress, akin to the Asaro-Tiller-Grinfeld mechanism in heteroepitaxy, as the driving pattern formation in IBS, see Section 5.2.1. Moreover,

Norris finds [265] that the main effects of stress can be captured even if elasticity is neglected. In a different work [264], the same author also considers a viscous flow framework, but now as a means to describe anisotropic plastic flow of the amorphous layer, as induced by the ion beam. In this model, a strong analogy is made with the properties of irradiation-induced stress in the MeV energy range [273,274]. In this energy range electronic stopping dominates over nuclear stopping, which is prevalent in the range of energies we are presently discussing [50]. Still, some of the properties described above, like the transition from flat to patterned surfaces at $\theta_c^{\text{theo}} = 45^\circ$ and the angle-dependence of the ripple wavelength, have been also obtained by this approach [264]. In this case, similar to a case in [263], a constant stress tensor, rather than a body force as in e.g. [262,263,58], is assumed to act throughout the amorphous layer. Actually, the model in [264] can be mathematically mapped to the body-force model in [263] by adding a multiple of the identity matrix to the stress tensor. This modification can be reabsorbed into the hydrostatic pressure, so that both models lead to the same predictions in the limit of a vanishing body force.

Although consistent progress seems to be building up through these hydrodynamic descriptions, a number of their current limitations have to be mentioned. An important one is the lack of predictions about the ripple rotation at grazing incidence angles. Whether the origin of this rotation is in stress forces or induced by the erosion or redistribution, it has to be elucidated yet. Also, recent systematic experimental studies, mentioned in Section 3.1, unambiguously report the dependence of the value of θ_c with e.g. ion-target combination, both for Si [275] and for other targets, like Ge [61,65]. Thinking in terms of e.g. thermodynamic phase transitions, the value of θ_c is akin to the value of the critical temperature, at which the characteristic wavelength likewise diverges. From this point of view it is natural to expect θ_c *not* to be an universal value. In any case, this fact remains to be fully reconciled with hydrodynamic descriptions. Incidentally, in the context of these two observations, we may note again Ref. [193]. In this work a mixed approach is taken, in which SDTrimSp simulations were compared with a continuum model. The latter incorporates an explicit surface-confined viscous flow mechanism together with erosive mechanisms. Improvements are proposed over the original CV effect, such as an explicit θ-dependence of the thickness of the amorphous layer. Interestingly, this work concludes that the BH mechanism is more relevant than as suggested by other crater-function approaches, and indeed dominant at glancing angles where rotated ripples can ensue. Although consistency of some of the constitutive laws in [193] remains to be systematically assessed, the results in this reference point to the capabilities for comprehensive modeling that similar type of multiscale approaches may have.

As a general conclusion on the theoretical descriptions of IBS for silicon targets, we believe that the focus of further efforts should probably remain with the dynamics of the amorphous layer, probably for both, mono-elemental and compound targets. Naturally, additional features need to be understood, such as the anisotropy of the IBS set-up and its relevance for transitions among different patterns. As suggested by the description just presented, a full understanding of the stress field beneath the surface does seem an important avenue for further significant experimental and theoretical improvements. These may in particular enhance our understanding of e.g. conspicuous morphologies such as hole patterns which, having been described in detail in a number of recent experiments as described above, seem to deserve a more detailed theoretical consideration. Furthermore, note that the most recent continuum models restrict their attention to relatively short times within which linear stability analysis holds. Beyond these, to date longer irradiation times still remain a challenge to the theoretical description, hosting a number of processes of a nonlinear nature, such as shadowing effects, faceting, wavelength coarsening, etc. Beyond their general interest as instances of far-from-equilibrium phenomena at the nanoscale, these properties also feature interest from an applied point of view, as they are key to the long-time evolution of the system. In particular, their understanding might provide the key to the production of more complex pattern morphologies, which lie beyond the relatively simple types of spatial ordering associated with linear instabilities.

6. Applications

The interest in the search for applications of IBS-nanostructured silicon surfaces has arisen in recent years. Most of the works reported so far concern the use of the nanopatterns as templates for further structuring. Thus, rippled targets have been employed as substrates to grow nanostructured thin Ni [276], Co [277], and multilayer [278] films. In particular, the relevance of silicon IBS nanopatterns as templates for growing nanostructured magnetic thin films was already pointed out by Teichert in 2003 [279]. Since then, the influence of IBS rippled morphologies in the magnetic properties of a deposited thin film has been addressed. For instance, a 9 nm thick permalloy film was deposited by Molecular Beam Epitaxy on IBS rippled silicon surfaces [280]. In this case, a 5 nm thick Cr buffer was also used in order to achieve a perfect replication of the rippled morphology into the metallic film. In this work, the main goal was to study how the ripple wavelength affected the magnetic properties of the film, the main aim being to tailor them. This was straightforward to do employing IBS ripples as templates since their wavelength can be tuned by changing the ion energy. The authors found a significant induced magnetic anisotropy only below a ripple wavelength threshold (close to 60 nm) as it is shown in Fig. 40. In contrast, above this threshold the corrugated Permalloy film acted as a flat film. More recently, the same group has studied how the uniaxial magnetic anisotropy (UMA), induced in a ferromagnetic film by the underlying IBS rippled Si substrate, depends on the film thickness [281]. In fact, an abrupt transition was observed, since for a thin film regime there is a corrugated alignment of the magnetic moments and above a critical thickness there are dipolar interactions due to the sinusoidal surface modulations.

There is also another application employing IBS nanopatterned Si substrates as templates to grow (metal) nanoparticles on top. The aim is to achieve a certain order in the array of nanoparticles through the substrate morphology. In fact, it was observed that Ag nanoparticles grown by sputtering [282] or evaporation [283] were preferentially located at the valleys of the rippled silicon templates (which have 35 nm of periodicity), resulting into a highly aligned array of Ag structures, as shown in Fig. 41(a). Moreover, due to the

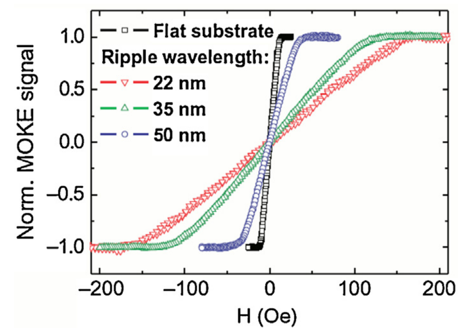

Fig. 40. Hard axis magnetization reversal investigated by magneto-optic Kerr effect (MOKE) for Permalloy films prepared on Si substrates with various ripple wavelengths as indicated. Reprinted from [280] under a Public Open Access License.

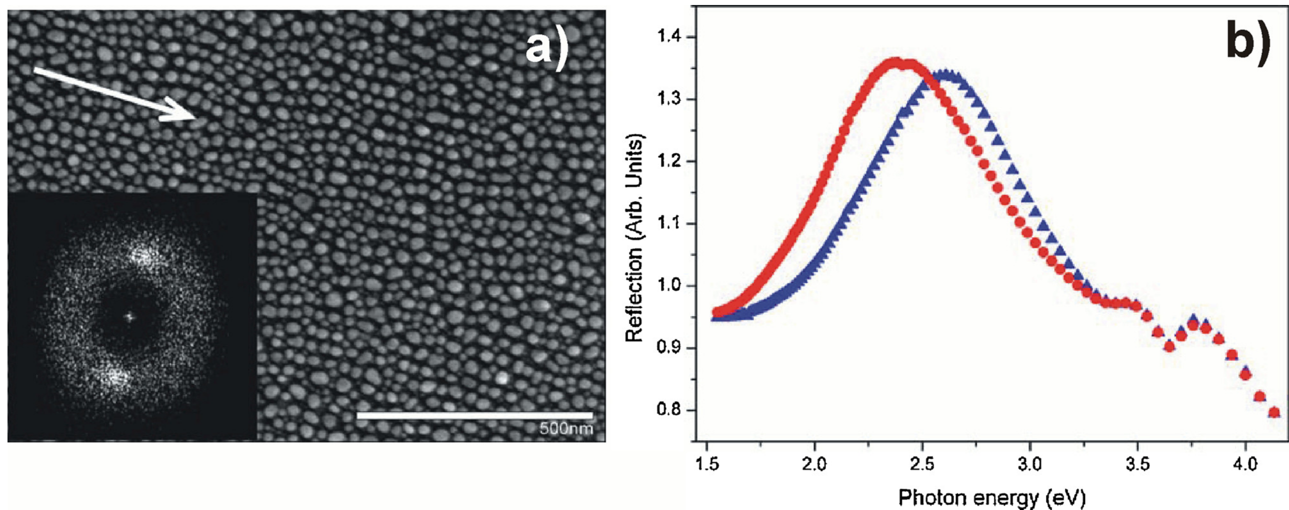

Fig. 41. (a) SEM image of silver nanoparticles on a rippled substrate with a periodicity of 35 nm. The arrow shows the direction of the ripples. The spatial Fourier transform (inset) shows distinctive peaks representing particle alignment. (b) Polarized reflection spectra of the sample shown in (a) for light polarized parallel (red circles) and perpendicular (blue triangles) to the direction of the ripples. A red shift of 0.21 eV is observed in the peak energy of the surface plasmon resonance for parallel polarization due to interparticle coupling of the resonances. Adapted with permission from [282]. Copyright 2007, Springer. (For interpretation of the references to colour in this figure legend, the reader is referred to the web version of this article.)

interparticle coupling of resonances, this array displayed a 0.21 eV shift in the surface plasmon resonance peak when light polarization is parallel or perpendicular to the direction of the ripples, see Fig. 41(b). The speed and simplicity of this method make it viable for cost-effective and large-scale production of mesoscale aligned nanostructures with adjustable periodicity.

It has also been recently shown that Ag nanoparticle arrays grown on rippled Si surfaces behave as surface-enhanced Raman scattering (SERS) active surfaces [284]. More specifically, it was found that inter-particle gap, ordering, and aspect ratio are key parameters to get maximum SERS intensity. Following a similar strategy, it is also possible to grow arrays of Ag or Au nanowires [284]. In this case, the former yield more intense SERS than the latter. It should be stressed that the flexibility of this approach can be exploited to make SERS-based biological sensors.

Another different functionality of Si nanopatterns produced by IBS has been found under the metal co-deposition approach described in Section 3.2. In this case [285], a Si surface was irradiated at normal incidence by 1.5 keV Ar^+ ions for 45 min at an ion current density of 1 mA/cm^2 with metal co-deposition resulting in an array of cone structures densely and randomly distributed over the surface as shown in Fig. 42. The cones have average height and base width close to 350 nm and 250 nm respectively. These surfaces appear black as seen by the naked eye. Moreover, an enhancement of more than 25% in absorption is observed in the light wavelength range from 350 to 2000 nm with respect to the polished Si [285]. Analogous results are obtained for thin film amorphous silicon solar cells irradiated with simultaneous co-deposition of Au [286]. In a further work, it was determined that the absorption of the nanostructured surfaces in fact increases with increasing aspect ratio and height of the nanostructures. A close to unity and all-solar-spectrum absorption by the nanostructured Si is finally achieved, with the absorbance for wavelengths in the 350–1100 nm range being higher than 96%, whereas for the 1100–2000 nm range it is higher than 92% [287].

The rippled silicon surfaces have been also recently used to study the adsorption of biomolecules on them. In particular, the adsorption of human plasma fibrinogen (HPF) was studied as a function of the ripple wavelength [288]. It was observed by AFM that the adsorption of HPF takes place in mostly globular conformation on crystalline and amorphous flat Si surfaces as well as on nano-structured Si with long ripple wavelengths. In contrast, for short ripple wavelengths the proteins seem to adsorb in a stretched formation and align across or along the ripples.

These are some examples of the interest of IBS nanopatterned Si surfaces for different applications. It should be noted that for many of them it is not relevant whether they are produced with or without metal co-deposition or if the nanostructures are crystalline or amorphous. As shown, the pattern anisotropy can be exploited as growth template but also interesting optical properties may appear

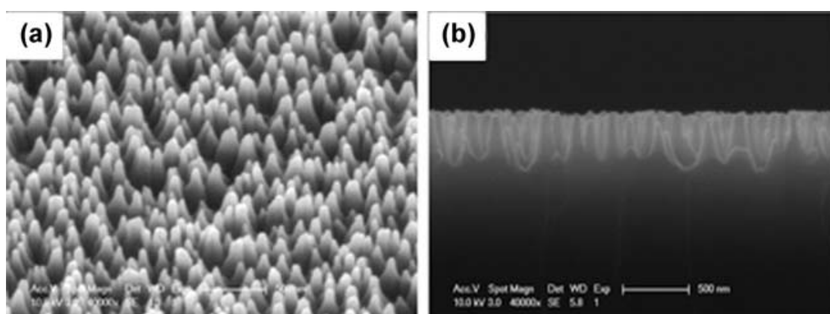

Fig. 42. Bird's-eye (a) and cross-sectional (b) view SEM images of the Si samples irradiated by 1.5 keV Ar^+ ions at a current density of 1 nA/cm^2 for 45 min with metal incorporation. Adapted with permission from [285]. Copyright 2011, AIP Publishing LLC.

from the nanopatterned silicon itself [289]. Regarding future applications in micro(opto)electronic devices, the formation of confined crystalline silicon nanoripples has also been realized on SiO_2 [290]. Furthermore, additional applications are being developed in other IBS surfaces, particularly silicon dioxide [291,292], which can be directly adapted to the case of silicon. Thus, the advance in the understanding of IBS nanopatterning of Si surfaces can indeed improve the control of this process not only in this material but also in many others, which surely will contribute to develop new and interesting applications for this kind of patterns at the nanoscale. Finally, it should be noted that although this review is focused on nanopatterning of silicon surfaces, recent efforts have been devoted to exploring new applications of IBS nanopatterns by extending the process to other highly functional semiconductors such as TiO_2 [293,294], ZnO [295] or CdTe [296].

7. Concluding remarks

The previous sections portrait a situation in which, although full theoretical understanding and experimental control of the IBS technique on Si surfaces have not yet been reached, consistent progress is nonetheless rapidly and consistently developing. Naturally, a crucial role in this process has been the realization of the important effect which contamination plays as a driving physical mechanism when it occurs. Thus, at the present moment the stage of development of the topic seems reminiscent of that at the time of previous reviews [2,3]. In these, a systematic assessment of the dependence of the pattern features with experimental parameters (flux, energy, temperature, etc.) was considered, albeit at times noting contradictions between results from different groups working under apparently similar conditions. Right now the main source of this type of variability seems to have been removed, so that more consistent progress can be expected in the elucidation of this self-organizing phenomenon, that revisits the issues that were already put forward in [2,3] as the next important steps to be taken in the field, on a more firm basis.

Promising results are already appearing simultaneously with this writing, and more are expected in a near future. Thus, a number of recent experimental studies have been mentioned above, in which some dependencies of the ripple wavelength with experimental parameters have been clearly assessed. However, there are some important issues that await to be explored and confirmed yet, such as the universality of system properties in terms of energy and ion/target combination. Also, important practical setups, such as irradiation of rotating targets, seem worth reconsidering in the light of recent developments. These might aid to consistently recover the high degree of control on, and the wide range of, experimental pattern shapes produced, which were achieved [108] prior to the realization of the role of contamination. A natural extension of this class of studies could be the patterning of the bulk of compound systems, which actually exploits the coupling between surface shape and composition that seems to take place [253,254].

Conceptually, the cases of compound systems and of those in which contamination is substantial, seem to be more complex than that of a clean monoelemental target, in such a way that the former should "reduce" to the latter in an appropriate limiting process. Hence, a non-trivial competition can be expected between the mechanisms of material redistribution and ion-induced stress, recently unveiled as relevant to the first, and preferential sputtering and compositional segregation, as seen in the second scenario. The result of work in this connection may clarify the reasons behind e.g. the universality of continuum models derived for clean systems for the evolution of targets irradiated with concurrent contaminant deposition. In general, it should provide a more comprehensive physical picture with an increased predictive power, that would enhance the present capabilities to nanostructure a wide range of materials beyond silicon itself.

Further interplays seem worth studying between different approaches or effects, which may contribute to an improved understanding in the field. One of them is the relation among different simulation techniques, each one of them having a characteristic range for optimal validity. In increasing order of length scales, these include MD, binary collision, and continuum approaches, as described above. A systematic or natural form to transition among them would be highly desirable, that could account for the way in which the large scale properties of one of them become effectively short scale ingredients for the next one in a hierarchy of increasing scales [297]. In any case, use of a combination of methods [298] seems ever more appropriate. Any progress along these lines will certainly impact not only the topic of the present review, which is particularly challenging in this respect [299], but also Materials Science at large. Another non-trivial interplay is that between spatial order in the patterns produced and spatial disorder, as induced by the pervasive conditions that enhance kinetic roughening. Recent indications exist [300] that the prevalence of one of these effects over the other (order vs disorder), and the form in which it takes place, may actually place constraints on the type of interfacial equation that is appropriate, and thus guide in the development of an accurate continuum description of the process.

Naturally, one expects that a direct benefit from a deeper understanding of the mechanisms behind IBS of silicon is the development of new applications to devices or processes of interest, from information technology to energy production and storage, to environmental issues. We have discussed a number of recent attempts in connection e.g. to magnetism or solar cells. Actually related proposals have already led to patents which are being commercially exploited [301]. One can speculate whether connections to more novel areas of research in which silicon, or targets which behave similarly under IBS, are finding usage—like circuits for nanofluidic channels and "transistors" [302], ultrathin membranes [303], or biocompatible imaging devices [304]—may benefit from the present and upcoming advances in the topic of the present review. In this way full harnessing of this fascinating bottom-up route to self-organized surface nanostructuring would be achieved and exploited, hopefully honoring Taniguchi's seminal forecast [1] at last.

Acknowledgements

We thank C. Ballesteros, V.I.T.A. de Rooij-Lohmann, M. Engler, S. Facsko, S.K. Garg, B. Galiana, D. Ghose, N.B. Ha, R. Hübner, M. Joe, D. Kanjilal, A. Keller, J.-H. Kim, J.-S. Kim, I.V. Kozhevnikov, T. Kumar, K.-R. Lee, K. Lorenz, T.H. Metzger, T. Michely, W. Möller, S. Mollick, A. Mücklich, M. Nicoli, F.J. Palomares, L. Peverini, O. Plantevin, M. Plapp, T. Som, C. Teichert, H. Urbassek, M. Varela, M. Vinnichenko, E. Vivo, and E. Ziegler for enriching collaborations during the course of our research. This work has been partially supported by the Spanish Ministries of Science and Innovation (grants Nos. FIS2009-12964-C05-01, FIS2009-12964-C05-03, FIS2009-12964-C05-04, and BES-2010-036179) and of Economy and Competitiveness (grants Nos. FIS2012-38866-C05-01 and FIS2012-38866-C05-05, FIS2012-32349 and FIS2013-47949-C2-2). A.R.C. also acknowledges funding from SFRH/BPD/74095/2010 (Portugal) and from Juan de la Cierva program (Spain) under contract No. JCI-2012-14509.

References

[1] N. Taniguchi, Proc. Intl. Conf. Prod. Eng., Tokyo, Part II, (1974), pp. 18–23.
[2] W.L. Chan, E. Chason, J. Appl. Phys. 101 (2007) 121301.

[3] J. Muñoz-García, L. Vázquez, R. Cuerno, J.A. Sánchez-García, M. Castro, R. Gago, Toward Functional Nanomaterials, Springer, New York, 2009, pp. 323–398.
[4] T. Som, D. Kanjilal, Nanofabrication by Ion-beam Sputtering: Fundamentals and Applications, CRC Press, Boca Raton, 2012.
[5] P. Bettotti, M. Cazzanelli, L. Dal Negro, B. Danese, Z. Gaburro, C. Oton, G.V. Prakash, L. Pavesi, J. Phys. Condens. Matter 14 (2002) 8253.
[6] L. Pavesi, L. Dal Negro, C. Mazzoleni, G. Franzo, F. Priolo, Nature 408 (2000) 440.
[7] Y. Yin, B. Gates, Y. Xia, Adv. Mater. 12 (2000) 1426.
[8] G. Grom, D. Lockwood, J. McCaffrey, H. Labbe, P. Fauchet, B. White, J. Diener, D. Kovalev, F. Koch, L. Tsybeskov, Nature 407 (2000) 358.
[9] N. Koshida, N. Matsumoto, Mater. Sci. Eng.: R Rep. 40 (2003) 169.
[10] R. Rurali, Rev. Mod. Phys. 82 (2010) 427.
[11] F.A. Zwanenburg, A.S. Dzurak, A. Morello, M.Y. Simmons, L.C.L. Hollenberg, G. Klimeck, S. Rogge, S.N. Coppersmith, M.A. Eriksson, Rev. Mod. Phys. 85 (2013) 961.
[12] H. Gnaser, Low Energy Ion Irradiation of Solid Surfaces, Springer-Verlag, Berlin, 1999.
[13] R. Gago, L. Vázquez, R. Cuerno, M. Varela, C. Ballesteros, J.M. Albella, Appl. Phys. Lett. 78 (2001) 3316.
[14] R. Cuerno, L. Vázquez, R. Gago, M. Castro, J. Phys. Condens. Matter 21 (2009) 220301.
[15] R. Cunningham, P. Haymann, C. Lecomte, W. Moore, J. Trillat, J. Appl. Phys. 31 (1960) 839.
[16] M. Navez, C. Sella, D. Chaperot, C. R. Acad. Sci. 254 (1962) 240.
[17] G. Carter, V. Vishnyakov, Y. Martynenko, M. Nobes, J. Appl. Phys. 78 (1995) 3559.
[18] K. Wittmaack, J. Vac. Sci. Technol. A 8 (1990) 2246.
[19] R.M. Bradley, J.M.E. Harper, J. Vac. Sci. Technol. A 6 (1988) 2390.
[20] P. Sigmund, J. Mater. Sci. 8 (1973) 1545.
[21] S. Facsko, T. Dekorsy, C. Koerdt, C. Trappe, H. Kurz, A. Vogt, H.L. Hartnagel, Science 285 (1999) 1551.
[22] G. Carter, M. Nobes, C. Cave, N. Al-Qadi, Vacuum 45 (1994) 71.
[23] U. Valbusa, C. Boragno, F. Buatier de Mongeot, J. Phys. Condens. Matter 14 (2002) 8153.
[24] R. Cuerno, A.-L. Barabási, Phys. Rev. Lett. 74 (1995) 4746.
[25] M. Makeev, A.-L. Barabási, Appl. Phys. Lett. 71 (1997) 2800.
[26] M. Makeev, R. Cuerno, A. Barabási, Nucl. Instrum. Meth. B 197 (2002) 185.
[27] B. Kahng, H. Jeong, A.-L. Barabási, Appl. Phys. Lett. 78 (2001) 805.
[28] M. Castro, R. Cuerno, L. Vázquez, R. Gago, Phys. Rev. Lett. 94 (2005) 016102.
[29] G. Ozaydin, A.S. Özcan, Y. Wang, F. Ludwig, H. Zhou, R.L. Headrick, D.P. Siddons, Appl. Phys. Lett. 87 (2005) 163104.
[30] C. Teichert, C. Hofer, G. Hlawacek, Adv. Eng. Mater. 8 (2006) 1057.
[31] G. Ozaydin, A.S. Özcan, Y. Wang, K.F. Ludwig Jr., H. Zhou, R.L. Headrick, Nucl. Instrum. Meth. B 264 (2007) 47.
[32] K. Zhang, M. Brötzmann, H. Hofsäss, New J. Phys. 13 (2011) 013033.
[33] S. Macko, F. Frost, M. Engler, D. Hirsch, T. Höche, J. Grenzer, T. Michely, New J. Phys. 13 (2011) 073017.
[34] J.A. Sánchez-García, L. Vázquez, R. Gago, A. Redondo-Cubero, J.M. Albella, Z. Czigány, Nanotechnology 19 (2008) 355306.
[35] A. Redondo-Cubero, R. Gago, F. Palomares, A. Mücklich, M. Vinnichenko, L. Vázquez, Phys. Rev. B 86 (2012) 085436.
[36] J. Zhou, S. Facsko, M. Lu, W. Moller, J. Appl. Phys. 109 (2011) 104315.
[37] C. Madi, B. Davidovitch, H. George, S. Norris, M. Brenner, M. Aziz, Phys. Rev. Lett. 101 (2008) 246102.
[38] C. Madi, B. Davidovitch, H. George, S. Norris, M. Brenner, M. Aziz, Phys. Rev. Lett. 107 (2011) 049902.
[39] C.S. Madi, H.B. George, M. Aziz, J. Phys. Condens. Matter 21 (2009) 224010.
[40] V. Shenoy, W. Chan, E. Chason, Phys. Rev. Lett. 98 (2007) 256101.
[41] C.S. Madi, M.J. Aziz, Appl. Surf. Sci. 258 (2012) 4112.
[42] F. Ludwig, C. Eddy, O. Malis, R. Headrick, Appl. Phys. Lett. 81 (2002) 2770.
[43] G. Ozaydin-Ince, K. Ludwig Jr., J. Phys. Condens. Matter 21 (2009) 224008.
[44] G. Carter, M.J. Nobes, F. Paton, J.S. Williams, J.L. Whitton, Radiat. Eff. Defect Solids 33 (1977) 65.
[45] G. Lewis, M. Nobes, G. Carter, J. Whitton, Nucl. Instrum. Meth 170 (1980) 363.
[46] G. Carter, V. Vishnyakov, Phys. Rev. B 54 (1996) 17647.
[47] Z.X. Jiang, P.F.A. Alkemade, Appl. Phys. Lett. 75 (1998) 315.
[48] G. Carter, J. Phys. D: Appl. Phys. 34 (2001) R1.
[49] S. Bhattacharjee, P. Karmakar, V. Naik, A. Sinha, A. Chakrabarti, Appl. Phys. Lett. 103 (2013) 181601.
[50] M.A. Nastasi, J.W. Mayer, J.K. Hirvonen, Ion–Solid Interactions: Fundamentals and Applications, Cambridge University Press, New York, 1996.
[51] O. El-Atwani, J. Allain, A. Cimaroli, S. Ortoleva, J. Appl. Phys. 110 (2011) 074301.
[52] O. El-Atwani, A. Suslova, A. DeMasi, S. Gonderman, J. Fowler, M. El-Atwani, K. Ludwig, J. Paul Allain, Appl. Phys. Lett. 101 (2012) 263104.
[53] O. El-Atwani, S. Gonderman, A. DeMasi, A. Suslova, J. Fowler, M. El-Atwani, K. Ludwig, J. Paul Allain, J. Appl. Phys. 113 (2013) 124305.
[54] D. Chowdhury, D. Ghose, B. Satpati, Mater. Sci. Eng. B 179 (2014) 1.
[55] K. Zhang, H. Hofsäss, F. Rotter, M. Uhrmacher, C. Ronning, J. Krauser, Surf. Coat. Technol. 203 (2009) 2395.
[56] A. Keller, S. Facsko, Materials 3 (2010) 4811.
[57] T. Basu, J.R. Mohanty, T. Som, Appl. Surf. Sci. 258 (2012) 9944.
[58] M. Castro, R. Gago, L. Vázquez, J. Muñoz-García, R. Cuerno, Phys. Rev. B 86 (2012) 214107.
[59] C. Madi, E. Anzenberg, K. Ludwig Jr., M. Aziz, Phys. Rev. Lett. 106 (2011) 66101.
[60] E. Anzenberg, C.S. Madi, M.J. Aziz, K.F. Ludwig Jr., Phys. Rev. B 84 (2011) 214108.
[61] E. Anzenberg, J.C. Perkinson, C.S. Madi, M.J. Aziz, K.F. Ludwig Jr., Phys. Rev. B 86 (2012) 245412.
[62] D. Carbone, A. Biermanns, B. Ziberi, F. Frost, O. Plantevin, U. Pietsch, T.H. Metzger, J. Phys. Condens. Matter 21 (2009) 224007.
[63] M. Cross, H. Greenside, Pattern Formation and Dynamics in Nonequilibrium Systems, Cambridge University Press, Cambridge, England, 2009.
[64] S. Macko, F. Frost, B. Ziberi, D.F. Förster, T. Michely, Nanotechnology 21 (2010) 085301.
[65] M. Teichmann, J. Lorbeer, B. Ziberi, F. Frost, B. Rauschenbach, New J. Phys. 15 (2013) 103029.
[66] T. Basu, T. Som, Appl. Surf. Sci. (2014).
[67] A. Keller, S. Roßbach, S. Facsko, W. Möller, Nanotechnology 19 (2008) 135303.
[68] A. Keller, R. Cuerno, S. Facsko, W. Möller, Phys. Rev. B 79 (2009) 115437.
[69] T. Basu, D.P. Datta, T. Som, Nanoscale Res. Lett. 8 (2013) 289.
[70] M. Engler, S. Macko, F. Frost, T. Michely, Phys. Rev. B 89 (2014) 245412.
[71] W. Hauffe, Phys. Stat. Sol. A 35 (1976) K93.
[72] T. Aste, U. Valbusa, New J. Phys. 7 (2005) 122.
[73] S. Habenicht, K.P. Lieb, J. Koch, A.D. Wieck, Phys. Rev. B 65 (2002) 115327.
[74] H. Hofsäss, K. Zhang, H. Gehrke, C. Brüsewitz, Phys. Rev. B 88 (2013) 075426.
[75] J. Erlebacher, M.J. Aziz, E. Chason, M.B. Sinclair, J.A. Floro, Phys. Rev. Lett. 82 (1999) 2330.
[76] S. Habenicht, K. Lieb, W. Bolse, U. Geyer, F. Roccaforte, C. Ronning, Nucl. Instrum. Meth. B 161 (2000) 958.
[77] K. Takahiro, K. Ozaki, K. Kawatsura, S. Nagata, S. Yamamoto, K. Narumi, H. Naramoto, Appl. Surf. Sci. 256 (2009) 972.
[78] O. Bobes, K. Zhang, H. Hofsäss, Phys. Rev. B 86 (2012) 235414.
[79] A.-D. Brown, J. Erlebacher, W.-L. Chan, E. Chason, Phys. Rev. Lett. 95 (2005) 056101.
[80] A.-D. Brown, J. Erlebacher, Phys. Rev. B 72 (2005) 075350.
[81] L. Csepregi, E. Kennedy, J. Mayer, T. Sigmon, J. Appl. Phys. 49 (1978) 3906.
[82] A. Keller, M. Nicoli, S. Facsko, R. Cuerno, Phys. Rev. E 84 (2011) 015202.
[83] A. Keller, M. Nicoli, S. Facsko, R. Cuerno, Phys. Rev. E 85 (2012) 029905(E).
[84] D.P. Datta, T.K. Chini, Phys. Rev. B 76 (2007) 075323.
[85] S.K. Garg, V. Venugopal, T. Basu, O. Sinha, S. Rath, D. Kanjilal, T. Som, Appl. Surf. Sci. 258 (2012) 4135.
[86] V. Vishnyakov, G. Carter, Nucl. Instrum. Meth. B 106 (1995) 174.
[87] G. Carter, V. Vishnyakov, M. Nobes, Nucl. Instrum. Meth. B 115 (1996) 440.
[88] G. Carter, J. Appl. Phys. 85 (1999) 455.
[89] D.P. Datta, T.K. Chini, Phys. Rev. B 69 (2004) 235313.
[90] T. Chini, D. Datta, S. Bhattacharyya, J. Phys. Condens. Matter 21 (2009) 224004.
[91] T. Kumar, A. Kumar, D.C. Agarwal, N.P. Lalla, D. Kanjilal, Nanoscale Res. Lett. 8 (2013) 336.
[92] A. Biermanns, U. Pietsch, J. Grenzer, A. Hanisch, S. Facsko, G. Carbone, T.H. Metzger, J. Appl. Phys. 104 (2008) 044312.
[93] A. Biermanns, A. Hanisch, J. Grenzer, T.H. Metzger, U. Pietsch, Phys. Stat. Sol. A 208 (2008) 2608.
[94] T. Chini, M. Sanyal, S. Bhattacharyya, Phys. Rev. B 66 (2002) 153404.
[95] F. Frost, A. Schindler, F. Bigl, Phys. Rev. Lett. 85 (2000) 4116.
[96] S. Le Roy, E. Barthel, N. Brun, A. Lelarge, E. Søndergard, J. Appl. Phys. 106 (2009) 094308.
[97] A. Cuenat, M.J. Aziz, in: Materials Research Society Symposium Proceedings, vol. 696, Cambridge University Press, Berlin, p. 31.
[98] W.-b. Fan, W.-q. Li, L.-j. Qi, H.-t. Sun, J. Luo, Y.-y. Zhao, M. Lu, Nanotechnology 16 (2005) 1526.
[99] B. Ziberi, F. Frost, B. Rauschenbach, T. Höche, Appl. Phys. Lett. 87 (2005) 033113.
[100] B. Ziberi, F. Frost, M. Tartz, H. Neumann, B. Rauschenbach, Appl. Phys. Lett. 92 (2008) 063102.
[101] B. Ziberi, F. Frost, M. Tartz, H. Neumann, B. Rauschenbach, Thin Solid Films 459 (2004) 106.
[102] K. Zhang, O. Bobes, H. Hofsäss, Nanotechnology 25 (2014) 085301.
[103] J. Muñoz-García, R. Gago, L. Vázquez, J.A. Sánchez-García, R. Cuerno, Phys. Rev. Lett. 104 (2010) 026101.
[104] T. Bobek, S. Facsko, H. Kurz, T. Dekorsy, M. Xu, C. Teichert, Phys. Rev. B 68 (2003) 085324.
[105] J. Muñoz-García, R. Gago, R. Cuerno, J. Sánchez-García, A. Redondo-Cubero, M. Castro, L. Vázquez, J. Phys. Condens. Matter 24 (2012) 375302.
[106] S. Fascko, T. Bobek, H. Kurz, T. Dekorsy, S. Kyrsta, R. Cremer, Appl. Phys. Lett. 80 (2002) 130.
[107] R. Gago, L. Vázquez, O. Plantevin, T.H. Metzger, J. Muñoz-García, R. Cuerno, M. Castro, Appl. Phys. Lett. 89 (2006) 233101.
[108] B. Ziberi, M. Cornejo, F. Frost, B. Rauschenbach, J. Phys. Condens. Matter 21 (2009) 224003.
[109] F. Frost, Appl. Phys. A 74 (2002) 131.
[110] Y.-P. Zhao, G.-C. Wang, T.-M. Lu, Characterization of Amorphous and Crystalline Rough Surfaces: Principles and Applications, Academic Press, San Diego, 2001.
[111] J.A. Sánchez-García, R. Gago, R. Caillard, A. Redondo-Cubero, J.A. Martin-Gago, F.J. Palomares, M. Fernández, L. Vázquez, J. Phys. Condens. Matter 21 (2009) 224009.
[112] B. Ziberi, F. Frost, T. Höche, B. Rauschenbach, Phys. Rev. B 72 (2005) 235310.
[113] M. Cornejo, B. Ziberi, C. Meinecke, D. Hirsch, J.W. Gerlach, T. Höche, F. Frost, B. Rauschenbach, Appl. Phys. A 102 (2011) 593.
[114] M. Cornejo, B. Ziberi, C. Meinecke, F. Frost, Appl. Surf. Sci. 257 (2011) 8659.
[115] B. Khanbabaee, B. Arezki, A. Biermanns, M. Cornejo, D. Hirsch, D. Lützenkirchen-Hecht, F. Frost, U. Pietsch, Thin Solid Films 527 (2013) 349.
[116] H. Hofsäss, K. Zhang, Appl. Phys. A 92 (2008) 517.
[117] S. Macko, J. Grenzer, F. Frost, M. Engler, D. Hirsch, M. Fritzsche, A. Mücklich, T. Michely, New J. Phys. 14 (2012) 073003.

[118] R. Gago, L. Vázquez, O. Plantevin, J.A. Sánchez-García, M. Varela, M.C. Ballesteros, J.M. Albella, T.H. Metzger, Phys. Rev. B 73 (2006) 155414.
[119] R. Behrisch, W. Eckstein, Sputtering by Particle Bombardment: Experiments and Computer Calculations from Threshold to MeV Energies, vol. 110, Springer Verlag, Berlin, 2007.
[120] V. Vishnyakov, G. Carter, D. Goddard, M. Nobes, Vacuum 46 (1995) 637.
[121] G. Ozaydin, K.F. Ludwig, H. Zhou, R.L. Headrick, J. Vac. Sci. Technol B 26 (2008) 551.
[122] H. Hofsäss, K. Zhang, A. Pape, O. Bobes, M. Brötzmann, Appl. Phys. A 111 (2013) 653.
[123] M. Engler, F. Frost, S. Müller, S. Macko, M. Will, R. Feder, D. Spermann, R. Hübner, S. Facsko, T. Michely, Nanotechnology 25 (2014) 115303.
[124] B. Khanbabaee, A. Biermanns, S. Facsko, J. Grenzer, U. Pietsch, J. Appl. Crystallogr. 46 (2013) 505.
[125] J. Zhou, M. Lu, Phys. Rev. B 82 (2010) 125404.
[126] P. Sigmund, Phys. Rev. 184 (1969) 383.
[127] M. Koster, H.M. Urbassek, Nucl. Instrum. Meth. B 180 (2001) 299.
[128] M.C. Moore, N. Kalyanasundaram, J.B. Freund, H.T. Johnson, Nucl. Instrum. Meth. B 225 (2004) 241.
[129] N. Kalyanasundaram, J. Freund, H. Johnson, J. Eng. Mater. Technol. 127 (2005) 457.
[130] N. Kalyanasundaram, M.C. Moore, J.B. Freund, H.T. Johnson, Acta Mater. 54 (2006) 483.
[131] N. Kalyanasundaram, M. Ghazisaeidi, J. Freund, H. Johnson, Appl. Phys. Lett. 92 (2008) 131909.
[132] N. Kalyanasundaram, J. Freund, H. Johnson, J. Phys. Condens. Matter 21 (2009) 224018.
[133] S.A. Norris, M.P. Brenner, M.J. Aziz, J. Phys. Condens. Matter 21 (2009) 224017.
[134] S.A. Norris, J. Samela, L. Bukonte, M. Backman, F. Djurabekova, K. Nordlund, C.S. Madi, M.P. Brenner, M.J. Aziz, Nat. Commun. 2 (2011) 276.
[135] M.L. Nietiadi, H.M. Urbassek, Appl. Phys. Lett. 103 (2013) 113108.
[136] J.C. Perkinson, E. Anzenberg, M.J. Aziz, J.K.F. Ludwig, Phys. Rev. B 89 (2014) 115433.
[137] M.P. Harrison, R.M. Bradley, Phys. Rev. B 89 (2014) 245401.
[138] M. Tang, L. Colombo, J. Zhu, T.D. De La Rubia, Phys. Rev. B 55 (1997) 14279.
[139] W.W. Mullins, J. Appl. Phys. 28 (1957) 333.
[140] S.G. Mayr, Y. Ashkenazy, K. Albe, R.S. Averback, Phys. Rev. Lett. 90 (2003) 055505.
[141] S.E. Orchard, Appl. Sci. Res. 11A (1962) 451.
[142] C.C. Umbach, R.L. Headrick, K.-C. Chan, Phys. Rev. Lett. 87 (2001) 246104.
[143] S.K. Theiss, M. Caturla, M. Johnson, J. Zhu, T. Lenosky, B. Sadigh, T. Diaz de la Rubia, Thin Solid Films 365 (2000) 219.
[144] W. Eckstein, S. Hackel, D. Heinemann, B. Fricke, Z. Phys. D 24 (1992) 171.
[145] B. Sadigh, T.J. Lenosky, S.K. Theiss, M.-J. Caturla, T.D. de la Rubia, M.A. Foad, Phys. Rev. Lett. 83 (1999) 4341.
[146] E. Holmström, A. Kuronen, K. Nordlund, Phys. Rev. B 78 (2008) 045202.
[147] D. Frenkel, B. Smit, Understanding Molecular Simulation: From Algorithms to Applications, Academic Press, San Diego, 2001.
[148] R. Smith, Atomic and Ion Collisions in Solids and at Surfaces: Theory, Simulation and Applications, Cambridge University Press, New York, 2005.
[149] J.F. Ziegler, J.P. Biersack, SRIM-2008, Stopping Power and Range of Ions in Matter, Nuclear Energy Agency-OECD/NEA, 2008.
[150] L. Bukonte, F. Djurabekova, J. Samela, K. Nordlund, S. Norris, M. Aziz, Nucl. Instrum. Meth. B 297 (2013) 23.
[151] K. Nordlund, Comput. Mater. Sci. 3 (1995) 448.
[152] K. Nordlund, M. Ghaly, R. Averback, M.-J. Caturla, Phys. Rev. B 57 (1998) 7556.
[153] K. Nordlund, J. Keinonen, M. Ghaly, R. Averback, Nucl. Instrum. Meth. B 148 (1999) 74.
[154] K. Nordlund, R. Averback, J. Nucl. Mater. 276 (2000) 194.
[155] B. Thijsse, T. Klaver, E. Haddeman, Appl. Surf. Sci. 231-232 (2004) 29.
[156] I. Santos, L.A. Marqués, L. Pelaz, P. López, M. Aboy, J. Barbolla, Mater. Sci. Eng. B 124 (2005) 372.
[157] H. Chan, K. Nordlund, J. Peltola, H.-J. Gossmann, N. Ma, M. Srinivasan, F. Benistant, L. Chan, Nucl. Instrum. Meth. B 228 (2005) 240.
[158] H. Hensel, H.M. Urbassek, Radiat. Eff. Defect Solids 142 (1997) 497.
[159] R. Goldberg, J. Williams, R. Elliman, Nucl. Instrum. Meth. B 106 (1995) 242.
[160] A. Mazzone, Ultramicroscopy 85 (2000) 15.
[161] Y. Rosandi, H.M. Urbassek, Phys. Rev. B 85 (2012) 155430.
[162] D. Stock, B. Weber, K. Gärtner, Phys. Rev. B 61 (2000) 8150.
[163] I. Santos, L.A. Marqués, L. Pelaz, Phys. Rev. B 74 (2006) 174115.
[164] L.A. Marqués, L. Pelaz, P. López, I. Santos, M. Aboy, Phys. Rev. B 76 (2007) 153201.
[165] L. Pelaz, L.A. Marqués, J. Barbolla, J. Appl. Phys. 96 (2004) 5947.
[166] B. Liedke, K.-H. Heinig, W. Möller, Nucl. Instrum. Meth. B 316 (2013) 56.
[167] J. Tarus, K. Nordlund, A. Kuronen, J. Keinonen, Phys. Rev. B 58 (1998) 9907.
[168] N.A. Kubota, D.J. Economou, S. Plimpton, J. Appl. Phys. 83 (1998) 4055.
[169] J. Finder, D. Richards, J. Adams, Model. Simul. Mater. Sci. Eng. 7 (1999) 495.
[170] M.L. Nietiadi, Y. Rosandi, M. Kopnarski, H.M. Urbassek, Nucl. Instrum. Meth. B 289 (2012) 97.
[171] J. Nord, K. Nordlund, J. Keinonen, Phys. Rev. B 65 (2002) 1.
[172] K. Beardmore, N. Grønbech Jensen, Phys. Rev. B 60 (1999) 610.
[173] K. Gärtner, B. Weber, Nucl. Instrum. Meth. B 180 (2001) 274.
[174] J. Peltola, K. Nordlund, J. Keinonen, Nucl. Instrum. Meth. B 195 (2002) 269.
[175] E. Haddeman, B. Thijsse, Nucl. Instrum. Meth. B 202 (2003) 161.
[176] D. Humbird, D.B. Graves, A. Stevens, W. Kessels, J. Vac. Sci. Technol. A 25 (2007) 1529.
[177] D. Humbird, D.B. Graves, Pure Appl. Chem. 74 (2002) 419.
[178] J.-C. Pothier, F. Schiettekatte, L. Lewis, Phys. Rev. B 83 (2011) 1.
[179] V. Borodin, Nucl. Instrum. Meth. B 282 (2012) 33.
[180] H. Haberland, Z. Insepov, M. Moseler, Phys. Rev. B 51 (1995) 11061.
[181] P. Süle, K.-H. Heinig, J. Chem. Phys 131 (2009) 204704.
[182] M. Koster, H. Urbassek, Phys. Rev. B 62 (2000) 219.
[183] M.J. Buehler, Atomistic and continuum studies of deformation and failure in brittle solids and thin film systems (dissertation), Universität Stuttgart, 2004.
[184] M. Koster, H.M. Urbassek, Surf. Sci. 496 (2002) 196.
[185] Y. Yin, D. McKenzie, M. Bilek, Surf. Coat. Technol. 198 (2005) 156.
[186] L. Pastewka, R. Salzer, A. Graff, F. Altmann, M. Moseler, Nucl. Instrum. Meth. B 267 (2009) 3072.
[187] M. Aziz, Matematisk-fysike Meddelelser 52 (2006) 187.
[188] J. Samela, K. Nordlund, V.N. Popok, E.E. Campbell, Phys. Rev. B 77 (2008) 075309.
[189] J. Samela, S. Norris, K. Nordlund, M. Aziz, Nucl. Instrum. Meth. B 269 (2011) 1568.
[190] Z. Yang, M. Lively, J.P. Allain, Nucl. Instrum. Meth. B 307 (2013) 189.
[191] M.Z. Hossain, K. Das, J.B. Freund, H.T. Johnson, Appl. Phys. Lett. 99 (2011) 151913.
[192] S.A. Norris, J. Samela, M. Vestberg, K. Nordlund, M.J. Aziz, Nucl. Instrum. Meth. B 318 (2014) 245.
[193] H. Hofsäss, Appl. Phys. A 114 (2014) 401.
[194] W. Eckstein, R. Dohmen, A. Mutzke, R. Schneider, IPP Report 12/3 (2007).
[195] R. Cuerno, M. Castro, J. Muñoz-García, R. Gago, L. Vázquez, Eur. Phys. J. Spec. Top. 146 (2007) 427.
[196] R. Cuerno, M. Castro, J. Muñoz-García, R. Gago, L. Vázquez, Nucl. Instrum. Meth. B 269 (2011) 894.
[197] W. Eckstein, C. Garcia-Rosales, J. Roth, W. Ottenberger, IPP Report 9/82 (1993).
[198] P. Sigmund, in: R. Behrisch (Ed.), Sputtering by Particle Bombardment I, Springer, Berlin, 1981.
[199] Y. Yamamura, Y. Itikawa, N. Itoh, IPPJ Report AM-26 (1983).
[200] G. Bales, R. Bruinsma, E. Eklund, R. Karunasiri, J. Rudnick, A. Zangwill, Science 249 (1990) 264.
[201] R. Ditchfield, E.G. Seebauer, Phys. Rev. Lett. 82 (1999) 1185.
[202] P.F. Alkemade, Phys. Rev. Lett. 96 (2006) 107602.
[203] B. Davidovitch, M.J. Aziz, M.P. Brenner, Phys. Rev. B 76 (2007) 205420.
[204] M. Moseler, P. Gumbsch, C. Casiraghi, A.C. Ferrari, J. Robertson, Science 309 (2005) 1545.
[205] S. Vauth, S. Mayr, Phys. Rev. B 75 (2007) 224107.
[206] H. Hofsäss, O. Bobes, K. Zhang, AIP Conf. Proc. 1525 (2013) 386.
[207] N. Medhekar, W. Chan, V. Shenoy, E. Chason, J. Phys. Condens. Matter 21 (2009) 224021.
[208] E. Chason, V. Shenoy, Nucl. Instrum. Meth. B 272 (2012) 178.
[209] J. Stangl, V. Holỳ, G. Bauer, Rev. Mod. Phys. 76 (2004) 725.
[210] J. Krug, Adv. Phys. 46 (1997) 139.
[211] R.M. Bradley, Phys. Rev. B 84 (2011) 075413.
[212] S. More, R. Kree, Appl. Surf. Sci. 258 (2012) 4179.
[213] A.-L. Barabási, H.E. Stanley, Fractal Concepts in Surface Growth, Cambridge University Press, New York, 1995.
[214] S. Habenicht, W. Bolse, K.P. Lieb, K. Reimann, U. Geyer, Phys. Rev. B 60 (1999) R2200.
[215] H.H. Chen, O.A. Urquidez, S. Ichim, L.H. Rodriguez, M.P. Brenner, J. Aziz, Science 310 (2005) 294.
[216] M. Holmes-Cerfon, M.J. Aziz, M.P. Brenner, Phys. Rev. B 85 (2012) 165441.
[217] M. Holmes-Cerfon, W. Zhou, A.L. Bertozzi, M.P. Brenner, M.J. Aziz, Appl. Phys. Lett. 101 (2012) 143109.
[218] S. Facsko, T. Bobek, A. Stahl, H. Kurz, T. Dekorsy, Phys. Rev. B 69 (2004) 153412.
[219] N. Anspach, S.J. Linz, J. Stat. Mech. Theory Exp. 2012 (2012) P06012.
[220] R.M. Bradley, Phys. Rev. B 83 (2011) 75404.
[221] C. Diddens, S. Linz, Europhys. Lett. 104 (2013) 17010.
[222] C. Diddens, S.J. Linz, Eur. Phys. J. B 86 (2013) 1.
[223] T.C. Kim, C.-M. Ghim, H.J. Kim, D.H. Kim, D.Y. Noh, N.D. Kim, J.W. Chung, J.S. Yang, Y.J. Chang, T.W. Noh, B. Kahng, J.-S. Kim, Phys. Rev. Lett. 92 (2004) 246104.
[224] M. Castro, R. Cuerno, Phys. Rev. Lett. 94 (2005) 139601.
[225] T.C. Kim, C.-M. Ghim, H.J. Kim, D.H. Kim, D.Y. Noh, N.D. Kim, J.W. Chung, J.S. Yang, Y.J. Chang, T.W. Noh, B. Kahng, J.-S. Kim, Phys. Rev. Lett. 94 (2005) 139602.
[226] M. Feix, A.K. Hartmann, R. Kree, J. Muñoz-García, R. Cuerno, Phys. Rev. B 71 (2005) 125407.
[227] T. Aste, U. Valbusa, Physica A 332 (2004) 548.
[228] Z. Csahók, C. Misbah, F. Rioual, A. Valance, Eur. Phys. J. E 3 (2000) 71.
[229] B. Spencer, P. Voorhees, J. Tersoff, Phys. Rev. B 64 (2001) 235318.
[230] J. Muñoz-García, R. Cuerno, M. Castro, J. Phys. Condens. Matter 21 (2009) 224020.
[231] J. Muñoz-García, M. Castro, R. Cuerno, Phys. Rev. Lett. 96 (2006) 086101.
[232] J. Muñoz-García, R. Cuerno, M. Castro, Phys. Rev. B 78 (2008) 205408.
[233] D. Kramczynski, B. Reuscher, H. Gnaser, Phys. Rev. B 89 (2014) 205422.
[234] J. Muñoz-García, R. Cuerno, M. Castro, Phys. Rev. E 74 (2006) R050103.
[235] M. Castro, J. Muñoz-García, R. Cuerno, M. García-Hernández, L. Vázquez, New J. Phys. 9 (2007) 102.
[236] M. Raible, S.G. Mayr, S.J. Linz, M. Moske, P. Hänggi, K. Samwer, Europhys. Lett. 50 (2000) 61.
[237] M. Raible, S.J. Linz, P. Hänggi, Phys. Rev. E 62 (2000) 1691.
[238] T. Tiedje, K.A. Mitchell, B. Lau, A. Ballestad, E. Nodwell, J. Geophys. Res. Earth Surf. 111 (2006) F02015.
[239] O. Bikondoa, D. Carbone, V. Chamard, T.H. Metzger, J. Phys. Condens. Matter 24 (2012) 445006.
[240] O. Bikondoa, D. Carbone, V. Chamard, T.H. Metzger, Scientific Reports 3 (2013).
[241] J. Kim, N. Ha, J. Kim, M. Joe, K. Lee, R. Cuerno, Nanotechnology 22 (2011) 285301.
[242] J.-H. Kim, J.-S. Kim, J. Muñoz-García, R. Cuerno, Phys. Rev. B 87 (2013) 085438.

[243] R.M. Bradley, P.D. Shipman, Phys. Rev. Lett. 105 (2010) 145501.
[244] P.D. Shipman, R.M. Bradley, Phys. Rev. B 84 (2011) 085420.
[245] R.M. Bradley, P.D. Shipman, Appl. Surf. Sci. 258 (2012) 4161.
[246] S.A. Norris, J. Samela, M. Vestberg, K. Nordlund, M.J. Aziz, Nucl. Instrum. Meth. B 318 (2014) 245.
[247] R.M. Bradley, J. Appl. Phys. 111 (2012) 114305.
[248] S.A. Norris, J. Appl. Phys. 114 (2013) 204303.
[249] F.C. Motta, P.D. Shipman, R.M. Bradley, J. Phys. D: Appl. Phys. 45 (2012) 122001.
[250] A. Keller, S. Facsko, Phys. Rev. B 82 (2010) 155444.
[251] S. Le Roy, E. Søndergård, I. Nerbø, M. Kildemo, M. Plapp, Phys. Rev. B 81 (2010) 161401.
[252] R.M. Bradley, K.W. Mauser, J. Appl. Phys. 114 (2013) 033506.
[253] G. Abrasonis, K. Morawetz, Phys. Rev. B 86 (2012) 085452.
[254] R.M. Bradley, J. Appl. Phys. 114 (2013) 224306.
[255] R. Kree, T. Yasseri, A. Hartmann, Nucl. Instrum. Meth. B 267 (2009) 1403.
[256] E.O. Yewande, Modelling and simulation of surface morphology driven by ion bombardment (Ph.D. Thesis), Universität Göttingen, 2006.
[257] A.K. Hartmann, R. Kree, T. Yasseri, J. Phys. Condens. Matter 21 (2009) 224015.
[258] R.M. Bradley, Phys. Rev. B 83 (2011) 195410.
[259] R.M. Bradley, Phys. Rev. B 85 (2012) 115419.
[260] R.M. Bradley, Phys. Rev. B 87 (2013) 205408.
[261] S.A. Mollick, D. Ghose, P.D. Shipman, R.M. Bradley, Appl. Phys. Lett. 104 (2014) 043103.
[262] M. Castro, R. Cuerno, arXiv preprint arXiv:1007.2144 (2010).
[263] M. Castro, R. Cuerno, Appl. Surf. Sci. 258 (2012) 4171.
[264] S.A. Norris, Phys. Rev. B 86 (2012) 235405.
[265] S.A. Norris, Phys. Rev. B 85 (2012) 155325.
[266] E. Chason, T.M. Mayer, B.K. Kellerman, D.T. McIlroy, A.J. Howard, Phys. Rev. Lett. 72 (1994) 3040.
[267] T.M. Mayer, E. Chason, A.J. Howard, J. Appl. Phys. 76 (1994) 1633.
[268] A. Rudy, V. Smirnov, Nucl. Instrum. Meth. B 159 (1999) 52.
[269] B. Abendroth, H. Jäger, W. Möller, M. Bilek, Appl. Phys. Lett. 90 (2007) 181910.
[270] H. Windischmann, J. Appl. Phys. 62 (1987) 1800.
[271] C.A. Davis, Thin Solid Films 226 (1993) 30.
[272] S. Habenicht, Phys. Rev. B 63 (2001) 125419.
[273] H. Trinkaus, A. Ryazanov, Phys. Rev. Lett. 74 (1995) 5072.
[274] H. Trinkaus, Nucl. Instrum. Meth. B 146 (1998) 204.
[275] K. Zhang, F. Rotter, M. Uhrmacher, C. Ronning, H. Hofsäss, J. Krauser, Surf. Coat. Technol. 201 (2007) 8299.
[276] A. Keller, L. Peverini, J. Grenzer, G.J. Kovacs, A. Mücklich, S. Facsko, Phys. Rev. B 84 (2011) 035423.
[277] D. Kumar, A. Gupta, Appl. Phys. Lett. 98 (2011) 123111.
[278] M. Körner, K. Lenz, M. Liedke, T. Strache, A. Mücklich, A. Keller, S. Facsko, J. Fassbender, Phys. Rev. B 80 (2009) 214401.
[279] C. Teichert, Appl. Phys. A 76 (2003) 653.
[280] J. Fassbender, T. Strache, M. Liedke, D. Markó, S. Wintz, K. Lenz, A. Keller, S. Facsko, I. Mönch, J. McCord, New J. Phys. 11 (2009) 125002.
[281] M. Liedke, M. Körner, K. Lenz, M. Fritzsche, M. Ranjan, A. Keller, E. Čižmár, S. Zvyagin, S. Facsko, K. Potzger, et al. Phys. Rev. B 87 (2013) 024424.
[282] T.W. Oates, A. Keller, S. Facsko, A. Mücklich, Plasmonics 2 (2007) 47.
[283] M. Ranjan, S. Facsko, M. Fritzsche, S. Mukherjee, Microelectron. Eng. 102 (2013) 44.
[284] M. Ranjan, S. Facsko, Nanotechnology 23 (2012) 485307.
[285] J. Zhou, M. Hildebrandt, M. Lu, J. Appl. Phys. 109 (2011) 053513.
[286] C. Martella, D. Chiappe, P. Delli Veneri, L.V. Mercaldo, I. Usatii, F. Buatier de Mongeot, Nanotechnology 24 (2013) 225201.
[287] Y. Qiu, H.-C. Hao, J. Zhou, M. Lu, Opt. Express 20 (2012) 22087.
[288] J. Sommerfeld, J. Richter, R. Niepelt, S. Kosan, T.F. Keller, K.D. Jandt, C. Ronning, Biointerphases 7 (2012) 1.
[289] L. Persechini, M. Ranjan, F. Grossmann, S. Facsko, J. McGilp, Phys. Stat. Sol. B 249 (2012) 1173.
[290] X. Ou, R. Kögler, X. Wei, A. Mücklich, X. Wang, W. Skorupa, S. Facsko, AIP Adv. 1 (2011) 042174.
[291] E. Mele, F. Di Benedetto, R. Cingolani, D. Pisignano, A. Toma, F.B. de Mongeot, R. Buzio, C. Boragno, G. Firpo, V. Mussi, et al. Nanotechnology 16 (2005) 2714.
[292] F. Granone, V. Mussi, A. Toma, S. Orlanducci, M. Terranova, C. Boragno, F. Buatier de Mongeot, U. Valbusa, Nucl. Instrum. Meth. B 230 (2005) 545.
[293] T. Luttrell, M. Batzill, Phys. Rev. B 82 (2010) 035408.
[294] M. Kolmer, A. Zebari, M. Goryl, F.B. de Mongeot, F. Zasada, W. Piskorz, P. Pietrzyk, Z. Sojka, F. Krok, M. Szymonski, Phys. Rev. B 88 (2013) 195427.
[295] H. Qian, W. Zhou, J. Phys. D: Appl. Phys. 42 (2009) 105304.
[296] R. Gago, L. Vázquez, F. Palomares, F. Agulló-Rueda, M. Vinnichenko, V. Carcelén, J. Olvera, J. Plaza, E. Diéguez, J. Phys. D: Appl. Phys. 46 (2013) 455302.
[297] G. Lu, E. Kaxiras, Handbook of Theoretical and Computational Nanotechnology, vol. X, American Scientific Publishers, Los Angeles, 2005, pp. 1–33.
[298] X.-M. Bai, A.F. Voter, R.G. Hoagland, M. Nastasi, B.P. Uberuaga, Science 327 (2010) 1631.
[299] T.D. de la Rubia, H.M. Zbib, T.A. Khraishi, B.D. Wirth, M. Victoria, M.J. Caturla, Nature 406 (2000) 871.
[300] E. Vivo, M. Nicoli, M. Engler, T. Michely, L. Vázquez, R. Cuerno, Phys. Rev. B 86 (2012) 245427.
[301] V. Smirnov, D. Kibalov, Methods of formation of a silicon nanostructure, a silicon quantum wire array and devices based thereon, US Patent 6,274,007 (2001).
[302] R. Karnik, K. Castelino, R. Fan, P. Yang, A. Majumdar, Nano Lett. 5 (2005) 1638.
[303] C.C. Striemer, T.R. Gaborski, J.L. McGrath, P.M. Fauchet, Nature 445 (2007) 749.
[304] F. Erogbogbo, K.-T. Yong, I. Roy, G. Xu, P.N. Prasad, M.T. Swihart, ACS Nano 2 (2008) 873.